

# NOTE TO USERS

This reproduction is the best copy available.

**UMI**<sup>®</sup>



CLOUD DETECTION AND TRACE GAS RETRIEVAL FROM THE NEXT  
GENERATION  
SATELLITE REMOTE SENSING INSTRUMENTS

A  
THESIS

Presented to the Faculty  
of the University of Alaska Fairbanks  
in Partial Fulfillment of the Requirements  
for the Degree of  
DOCTOR OF PHILOSOPHY

By

North Fredrick Larsen, B.S., M.S.

Fairbanks, Alaska

May 2005

UMI Number: 3167011

### INFORMATION TO USERS

The quality of this reproduction is dependent upon the quality of the copy submitted. Broken or indistinct print, colored or poor quality illustrations and photographs, print bleed-through, substandard margins, and improper alignment can adversely affect reproduction.

In the unlikely event that the author did not send a complete manuscript and there are missing pages, these will be noted. Also, if unauthorized copyright material had to be removed, a note will indicate the deletion.

**UMI**<sup>®</sup>

---

UMI Microform 3167011

Copyright 2005 by ProQuest Information and Learning Company.

All rights reserved. This microform edition is protected against unauthorized copying under Title 17, United States Code.

ProQuest Information and Learning Company  
300 North Zeeb Road  
P.O. Box 1346  
Ann Arbor, MI 48106-1346

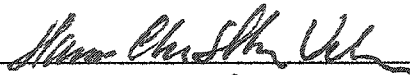


CLOUD DETECTION AND TRACE GAS RETRIEVAL FROM THE NEXT  
GENERATION  
SATELLITE REMOTE SENSING INSTRUMENTS

By

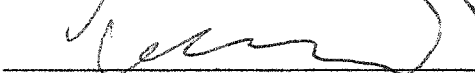
North Fredrick Larsen

RECOMMENDED:

  
\_\_\_\_\_

  
\_\_\_\_\_

  
\_\_\_\_\_

  
\_\_\_\_\_

Advisory Committee Chair

  
\_\_\_\_\_

Department Head

APPROVED:

  
\_\_\_\_\_  
Dean, College of Natural Science and Mathematics

  
\_\_\_\_\_  
Dean of the Graduate School

  
\_\_\_\_\_  
Date

## Abstract

The objective of this thesis is to develop a cloud detection algorithm suitable for the National Polar Orbiting Environmental Satellite System (NPOESS) Visible Infrared Imaging Radiometer Suite (VIIRS) and methods for atmospheric trace gas retrieval for future satellite remote sensing instruments. The development of this VIIRS cloud mask required a flowdown process of different sensor models in which a variety of sensor effects were simulated and evaluated. This included cloud simulations and cloud test development to investigate possible sensor effects, and a comprehensive flowdown analysis of the algorithm was conducted. In addition, a technique for total column water vapor retrieval using shadows was developed with the goal of enhancing water vapor retrievals under hazy atmospheric conditions. This is a new technique that relies on radiance differences between clear and shadowed surfaces, combined with ratios between water vapor absorbing and window regions. A novel method for retrieving methane amounts over water bodies, including lakes, rivers, and oceans, under conditions of sun glint has also been developed. The theoretical basis for the water vapor as well as the methane retrieval techniques is derived and simulated using a radiative transfer model.

## Table of Contents

Signature Page .....	i
Title Page .....	ii
Abstract .....	iii
Table of Contents.....	iv
List of Figures .....	vii
List of Tables .....	xii
List of Appendices .....	xiv
Acknowledgments.....	xv
<b>Chapter 1 - Introduction .....</b>	<b>16</b>
1.0 Introduction.....	16
1.1 The NPOESS Program.....	19
1.1.1 NPOESS Program Description .....	20
1.1.2 Sensors of the NPOESS Program .....	22
1.1.3 NPOESS Data Products .....	23
1.1.4 NPOESS Timeline .....	25
1.2 The VIIRS Sensor System .....	26
1.3 The VIIRS Sensor Bandset .....	30
1.3.1 The VNIR VIIRS Sensor Bandset .....	30
1.3.2 The SWIR VIIRS Sensor Bandset .....	33
1.3.3 The MWIR VIIRS Sensor Bandset.....	35
1.3.4 The LWIR VIIRS Sensor Bandset.....	37
1.4 The MODIS Airborne Simulator Sensor .....	39
1.5 Algorithms Developed for Future Sensors .....	41
<b>Chapter 2 – The VIIRS Cloud Mask.....</b>	<b>42</b>
2.0 Introduction.....	42

2.1 Overview .....	42
2.1.1 Cloud Mask Definition .....	43
2.1.2 Objective of the Cloud Mask .....	45
2.1.3 Historical Perspective on Cloud Detection .....	45
2.1.4 Cloud Mask Algorithm .....	46
2.1.4.1 Inputs to the Cloud Mask .....	46
2.1.4.2 Algorithm Description and Processing .....	53
2.1.4.3 Cloud Mask Output .....	64
2.2 Description and Physics of Cloud Masking .....	66
2.2.1 Pixel Level Cloud Detection Tests .....	66
2.2.1.1 Thermal BT Tests .....	69
2.2.1.2 Visible to MWIR Reflectance Tests .....	70
2.2.1.3 Imagery Band Tests .....	71
2.2.1.4 Tests for Future Investigation .....	72
2.2.1.5 Additional Pixel Level Tests .....	73
2.3 Cloud Mask over Varying Surface Types .....	75
2.4 Error Budget and Flowdown Results .....	79
2.4.1 Sensor Noise Flowdown .....	80
2.4.2 Cloud Cover Flowdown Analysis .....	80
2.5 Cloud Mask Validation .....	81
2.5.1 VCM Retrieval Examples on MAS Data .....	81
2.5.2 Predicted Performance of the Cloud Mask .....	84
2.6 Summary .....	87
<b>Chapter 3 – Effect of Band-to-Band Mis-registration on Cloud Detection .....</b>	<b>88</b>
3.0 Band-to-Band Mis-registration Flowdown Study .....	88
3.1 Analysis .....	90
3.2 Assumptions .....	91
3.3 Effect of BBM on Cloud Mask and Cloud Cover .....	92

3.4 Conclusions.....	104
<b>Chapter 4 - Use of Shadows to Retrieve Water Vapor in Hazy Atmospheres ..</b>	<b>106</b>
4.0 Introduction.....	106
4.1 Overview and Background .....	108
4.2 Description of the Shadow Algorithm .....	117
4.2.1 Basic Equations.....	117
4.2.2 Derivation of the Shadow Algorithm.....	119
4.2.3 Simulations and Comparisons.....	123
4.3 Practical Considerations.....	127
4.4 Conclusions.....	129
<b>Chapter 5 - Methane Detection from Space: Use of Sun Glint .....</b>	<b>130</b>
5.0 Introduction.....	130
5.1 Overview and Background .....	131
5.1.1 Methane Sources .....	131
5.1.2 Ground-based Methane Remote Sensing Techniques .....	132
5.1.3 Satellite Remote Sensing Potential .....	134
5.1.4 Sun Glint Features.....	135
5.2 Description of the Algorithm.....	139
5.3 Radiative Transfer Simulations.....	144
5.4 Practical Considerations.....	150
5.5 Conclusions.....	151
<b>Chapter 6 – Summary and Discussion .....</b>	<b>152</b>
<b>Appendices .....</b>	<b>155</b>
<b>References .....</b>	<b>203</b>

## List of Figures

Figure 1.1 Evolution of the NPOESS satellite system .....	21
Figure 1.2 NPOESS system timeline .....	25
Figure 1.3 Comparison of the VIIRS imagery bandset with heritage sensors .....	27
Figure 1.4 Summary of VIIRS design concepts and heritage .....	28
Figure 1.5 Summary of VIIRS imaging bands design .....	29
Figure 1.6 The VIIRS VNIR spectral bands .....	31
Figure 1.7 The VIIRS SWIR spectral bands .....	34
Figure 1.8 The VIIRS MWIR spectral bands .....	36
Figure 1.9 The VIIRS LWIR spectral bands .....	38
Figure 2.1 An illustration of band nesting.....	52
Figure 2.2 Conceptual overview of the VCM EDR .....	54
Figure 2.3 First section of flowchart of the VCM .....	56
Figure 2.4 Second section of the flowchart of the VCM.....	58

Figure 2.5 Third section of the flowchart of the VCM .....	61
Figure 2.6 Graphical depiction of confidence thresholds.....	62
Figure 2.7 The final section of the flowchart of the VCM.....	63
Figure 2.8 Conceptual overview of the pixel region classification by the VCM.....	64
Figure 2.9 Conceptual flow of the VCM over land regions.....	76
Figure 2.10 Conceptual flow of the VCM over water regions.....	77
Figure 2.11 Conceptual flow of the VCM over polar regions.....	78
Figure 2.12 VCM over sea ice .....	83
Figure 3.1 MAS scene used in BBM study .....	89
Figure 3.2(a) Total misclassification due to BBM .....	93
Figure 3.2(b) The cloudy-when-clear misclassification due to BBM .....	94
Figure 3.2(c) The clear-when-cloudy misclassification due to BBM .....	95
Figure 3.3(a) Cloud cover accuracy for 25 km HCS .....	99
Figure 3.3(b) Cloud cover precision for 25 km HCS .....	99
Figure 3.3(c) Cloud cover accuracy for 13 km HCS .....	100

Figure 3.3(d) Cloud cover precision for 13 km HCS .....	100
Figure 3.3(e) Cloud cover accuracy for 6.5 km HCS .....	101
Figure 3.3(f) Cloud cover precision for 6.5 km HCS.....	101
Figure 3.3(g) Cloud cover accuracy for 2.5 km HCS ... ..	102
Figure 3.3(h) Cloud cover precision for 2.5 km HCS .....	102
Figure 4.1 Atmospheric transmission across the NIR spectral region .....	109
Figure 4.2 Gao method of reflectance ratio vs. precipitable water ... ..	114
Figure 4.3 Conceptual illustration of the shadow method ... ..	120
Figure 4.4 Shadow method of reflectance ratio vs. precipitable water .....	124
Figure 4.5 Gao method reflectance ratio haze and clear sky difference .....	125
Figure 4.6 Shadow method reflectance ratio haze and clear sky difference.....	126
Figure 5.1 Solar and viewing angles definition ... ..	137
Figure 5.2 SWIR atmospheric transmission 2100 - 2350 nm .....	140
Figure 5.3 Reflectance ratios versus total column methane for a short path length...	147



Figure 5.4 Reflectance ratios versus total column methane for a long path length...	148
Figure 5.5 Reflectance ratios versus surface methane for a short path length.....	149
Figure B-1 VIIRS Cloud Mask context level data flow diagram.....	158
Figure B-2 VIIRS Cloud Mask component level data flow diagram.....	159
Figure C-1 VIIRS Cloud Phase Algorithm... ..	161
Figure E-1(a-b) Optical thickness and truth case .....	182
Figure E-2(a-f) Simulated reflectance and BT of the VIIRS channels .....	183
Figure E-3(a-h) Noise models applied to daytime Cloud Mask.....	184
Figure E-4(a-h) Noise models applied to nighttime Cloud Mask... ..	185
Figure E-5 VIIRS Cloud Cover accuracy and precision at 25 km .....	187
Figure E-6 VIIRS Cloud Cover accuracy and precision at 2 km... ..	188
Figure F-1 Synthetic imagery generation diagram.....	190
Figure F-2 The process for imagery generation .....	191
Figure F-3(a) Reflectance for water cloud scene at 0.65 and 0.86 $\mu\text{m}$ ... ..	193
Figure F-3(b) Reflectance for water cloud scene at 1.24 and 1.38 $\mu\text{m}$ ... ..	193

Figure F-3(c) Reflectance for water cloud scene at 1.61 and 2.14 $\mu\text{m}$ ... ..	193
Figure F-3(d) BT for water cloud scene at 3.75 and 8.5 $\mu\text{m}$ .....	194
Figure F-3(e) VIIRS BT for water cloud scene at 10.8 and 12.0 $\mu\text{m}$ .....	194
Figure F-4 VCM results for a simulated water cloud scene .....	195
Figure F-5(a) Reflectance for cirrus cloud scene at 0.65 and 0.86 $\mu\text{m}$ ... ..	196
Figure F-5(b) Reflectance for cirrus cloud scene at 1.24 and 1.38 $\mu\text{m}$ .....	196
Figure F-5(c) Reflectance for cirrus cloud scene at 1.61 and 2.14 $\mu\text{m}$ ... ..	197
Figure F-5(d) BT for cirrus cloud scene at 3.75 and 8.5 $\mu\text{m}$ .....	197
Figure F-5(e) BT for cirrus cloud scene at 10.8 and 12.0 $\mu\text{m}$ ... ..	198
Figure F-6 VCM results for a simulated cirrus cloud ... ..	198

### List of Tables

Table 1.1 NPOESS Environmental Data Records and Imagery Products .....	24
Table 1.2 Description of the MAS instrumentation.....	40
Table 2.1 VIIRS Cloud Cover/Layers/Mask EDR.....	44
Table 2.2 Parameters for the VCM product.....	47
Table 2.3 The VIIRS channels used by the VCM.....	48
Table 2.4 Ancillary VIIRS data for the VCM.....	48
Table 2.5 The 48 bit Intermediate Product (IP) output of the VCM.....	65
Table 2.6 VCM tests performed with MAS thresholds .....	68
Table 2.7(a) Daytime probability of correct typing of the VCM.....	85
Table 2.7(b) Nighttime probability of correct typing of the VCM.....	86
Table 3.1 Effect of BBM upon cloud mask misclassification .....	97
Table 3.2(a) Effect of BBM upon cloud cover accuracy .....	103
Table 3.2(b) Effect of BBM upon cloud cover precision .....	103
Table A-1 Ancillary non-VIIRS data useful for the VCM.....	155

Table D-1(a) Cloud mask daytime ocean error budget.....	166
Table D-1(b) Cloud mask nighttime ocean error budget.....	167
Table D-1(c) Cloud mask daytime land error budget.....	168
Table D-1(d) Cloud mask nighttime land error budget.....	169
Table D-2 Error allocation to inputs to the cloud mask module.....	174
Table E-1 Scenario list of simulated data for sensor noise flowdown.....	180
Table F-1 Scenario list of simulated scene data used for the VCM.....	192
Table G-1 Table of acronyms.....	199

## List of Appendices

Appendix A) Ancillary Data of Future Use to VIIRS .....	155
Appendix B) Cloud Mask Software Architecture.....	157
Appendix C) The VIIRS Cloud Phase Product.....	160
Appendix D) Error Budget and Flowdown Results.....	164
Appendix E) Sensor Noise Flowdown and Cloud Cover Flowdown Analysis .....	179
Appendix F) Cloud Mask Validation and Simulation .....	189
Appendix G) Glossary of Acronyms .....	199

## Acknowledgements

I would like to thank my professor Dr. Knut Stamnes, my thesis advisor at the University of Alaska, Fairbanks. His continuous advice and encouragement made the completion of this thesis possible. I am grateful for this opportunity to work with him. My sincere appreciation also goes to other members of my graduate advisory committee: professors Dr. Brenton Watkins, Dr. Hans Nielsen, and Dr. John Olson. Their concerns and helpful suggestions improved my research work and the quality of my thesis.

I would also like to thank research scientist Dr. Si-Chee Tsay of NASA Goddard Space Flight Center (GSFC) for his mentoring, encouragement, and his facilitating the opportunity to do research at NASA GSFC. I would like to additionally thank the NASA GSFC research scientists Dr. Michael King and Dr. Yoram Kaufman, research scientist Dr. Bo-Cai Gao of the Naval Research Labs (NRL), and the UCLA professors Dr. Kuo-Nan Liou and Dr. Steven Ou for their guidance and stimulating and inspiring conversations.

I would finally like to thank my sister Yvonne for her love and friendship. I would like to thank my parents, Fred and Kate, whose love of education and academia led me to pursue this degree, rather than follow the family trade and become a commercial fisherman.

## **Chapter 1**

### **Introduction**

#### **1.0 Introduction**

Clouds are known to strongly moderate the energy balance of the Earth-atmosphere system through their interaction with solar and terrestrial radiation. Clouds reflect part of the solar energy back to space, and in doing so have a cooling effect upon the Earth-atmosphere system. Clouds also have a role in the greenhouse effect, by absorbing part of the longwave radiation emitted by the Earth's surface and thus warming the Earth's surface and the lower atmosphere. In Addition, the surface albedo and cloud properties are of great interest in studies of the global radiation budget and climate change.

The Earth's lower atmosphere is composed of gas molecules, cloud droplets, and aerosols. These components interact with solar and terrestrial radiation through processes involving scattering, absorption, and reflection. The radiation from the Sun is partially absorbed by aerosols, molecules, and clouds as well as the underlying surface. A significant portion of the solar radiation is scattered back to space by the atmosphere (aerosols, molecules and clouds) and the Earth's surface. The surface absorbs part of the incident solar radiation reaching it, and reflects the rest. The radiation reflected by the surface interacts with molecules, clouds, and aerosols in the atmosphere on its transit back to space, with a fraction reaching space and the rest being reflected back to the surface once more or absorbed by the atmosphere. The Earth's surface additionally emits thermal radiation which is partly absorbed by molecules, mainly water vapor, carbon dioxide, and ozone, absorbed by aerosols or cloud droplets, and weakly scattered by aerosol particles before it also reaches the top of the atmosphere. Clouds, aerosols, and molecules in the atmosphere also absorb and emit thermal radiation.

Satellite sensors detect a combination of radiation emitted and reflected from the Earth's surface and transmitted through the atmosphere. Additionally, sensors detect radiation emitted by the atmosphere or scattered into the field of view of satellite sensors by particles or molecules in the atmosphere. This radiation has spectral absorption signatures that allow for sensors to be developed to facilitate the retrieval of specific atmospheric and surface properties. The retrieval of these properties requires understanding of the physical processes of absorption, emission, and scattering by the atmosphere-surface system. Measured radiation can be used in conjunction with radiative transfer calculations to retrieve surface and atmospheric properties.

Due to the sparse spatial coverage of ground-based sensors to do such studies, programs such as the National Polar-orbiting Operational Environmental Satellite System (NPOESS) have been developed to investigate global climate and produce environmental products for research and monitoring purposes. This chapter contains a discussion of the NPOESS program, the NPOESS sensor/algorithm system, the Visible Infrared Imaging Radiometer Suite (VIIRS) sensor, the VIIRS multi-spectral and imaging bandset, and the MODIS Airborne Simulator (MAS) sensor. The MAS sensor has been used for the VIIRS cloud detection algorithm development.

Cloud detection algorithms are an initial step in satellite remote sensing processing. Such algorithms discriminate cloudy from clear pixels and enable additional processing to be done upon cloudy as well as cloud-free regions. To this end, a cloud detection algorithm has been developed for the VIIRS sensor. Chapter 2 describes this VIIRS Cloud detection algorithm, explaining the physics, the processing, the resulting product, the error sources, and the flowdown of this cloud detection algorithm using MAS imagery and simulated cloud scenes.

Chapter 3 is a study of the effects of Band-to-Band Mis-Registration (BBM) on the multi-spectral VIIRS cloud detection algorithm. The BBM occurs in imagery when pixels from multiple bands are not completely co-registered to the same location on the



Earth. The BBM is either a result of sensor imaging optical array defects, focal plane misalignment, and/or errors in the geolocation processing. Because the VIIRS Cloud Mask algorithm employs multiple bands that may be mis-registered, it could possibly be affected by BBM. The sensitivity of the of cloud detection to BBM is presented in this chapter.

Once cloud detection is done for a satellite-borne remote sensing system, then additional algorithms may be developed and applied to the clear sky imagery. Such algorithms are developed in Chapters 4 and 5.

In Chapter 4, an algorithm is developed that employs cloud shadows to improve upon water vapor retrievals under hazy atmospheric conditions. Historically, techniques to retrieve total column water vapor have been developed that rely upon observation of water vapor attenuation of near infrared solar radiation reflected by the Earth's surface. Ratios of measured radiances at wavelengths inside and outside of water vapor absorbing channels are used for retrieval purposes. These ratios partially remove the dependence of surface reflectance on wavelength, and are used to retrieve the total column water vapor amount. Hazy atmospheric conditions, however, introduce errors into this widely used technique. In this chapter a new method is presented, it is based upon radiance differences between clear and nearby shadowed surfaces, combined with ratios between water vapor absorbing and window regions. This new method improves water vapor retrievals under hazy atmospheric conditions. Radiative transfer simulations are used to demonstrate the advantage offered by this technique.

In Chapter 5, an algorithm is developed to use remote sensing to detect methane seepage over water bodies. Methane seepage is indicative of petroleum or natural gas reserves. Techniques aimed at detecting methane seepage with surface-based instrumentation have progressed significantly in recent years. These instruments rely upon measurement of light attenuation due to methane absorption of Short Wave Infrared (SWIR) radiation. Detection of methane seepage over water bodies with

electro-optical remote sensing has been limited due to the low surface reflectance of water. Also, due to sensor saturation, imagery over sun glint is commonly discarded in satellite remote sensing because the glint conditions produce high surface reflectance. However, recent measurements in the SWIR of sun glint regions have revealed that the surface reflectance is spectrally flat while enhanced without causing saturation. This higher surface reflectance in sun glint regions allow for retrieval of total column methane amount using ratios of measured radiances at wavelengths inside and outside of methane absorbing SWIR channels. The methane retrieval method presented here, based on short wave infrared ratios in sun glint regions, allows for detection of methane seepage over the Earth's oceans and lakes, and the detection of possible petroleum or natural gas reserves. Radiative transfer simulations are used to demonstrate the capabilities offered by this technique.

Finally, a summary of the thesis is provided in Chapter 6.

### **1.1 The NPOESS Program**

In 1994, the decision was made to merge America's military and civil operational meteorological satellite systems into a single satellite system. This new satellite system is the National Polar-orbiting Operational Environmental Satellite System (NPOESS). NPOESS merges Department of Defense (DoD), National Oceanic and Atmosphere Administration (NOAA), and Department of Commerce (DOC) meteorological satellite systems into a single national asset.

The mission of the NPOESS system is to provide a national, operational, polar-orbiting, environmental remote-sensing capability to the United States and her allies. In addition, by merging the three national agencies (NOAA, DoD, and DOC) civilian satellite programs together a projected savings of 1.8 billion United States dollars is projected (*Cunningham, 2001*). Also, NPOESS is expected to incorporate new

technologies from the National Aeronautics and Space Administration (NASA) and also to encourage international cooperation.

Observing the Earth from space, polar-orbiting satellites collect and disseminate data on Earth's weather and atmosphere, oceans, land, and space environment. The polar orbiters are able to monitor the entire Earth to provide data for long-range weather and climate forecasts. The NPOESS system consists of a suite of sensors on each platform.

The Departments of Commerce and Defense as well as NASA created the NPOESS Integrated Program Office (IPO) to develop, acquire, manage, and operate the next generation of polar-orbiting operational environmental satellites. As part of this effort, the United States has partnered with the European Organization for the Exploitation of Meteorological Satellites (EUMETSAT) to provide long-term continuity of observations from polar orbit that will continue and improve the operational meteorological and environmental forecasting and global climate monitoring services of the participating organizations.

The NPOESS program extends to the year 2018, building on new technologies to create a new system supporting long-term data continuity for environmental monitoring and global change assessment.

### **1.1.1 NPOESS Program Description**

NPOESS has undertaken a far-reaching program of sensor development and satellite transition to provide complete coverage of meteorological conditions for civil, military, and scientific purposes while cutting operational costs dramatically.

To accomplish its mission, NPOESS satellites in two orbital planes will replace the two-satellite Defense Meteorological Satellite Program (DMSP) and Polar Orbiting Environmental Satellite (POES) constellations, respectively, along with EUMETSAT providing data in the mid-morning orbital plane. NPOESS and EUMETSAT will share

data from their polar-orbiting satellites. The evolution of the satellite configuration is depicted in Figure 1.1 (Cunningham, 2001).

As is depicted in Figure 1.1, the NPOESS satellites will be a polar-orbiting satellite system. There are several benefits to such a system. A polar-orbiting satellite is able to provide full global coverage, while its geostationary counterparts, such as the Geostationary Operational Environmental Satellite (GOES) satellites, are limited to approximately 60 degrees of latitude at a fixed point over the Earth. Polar-orbiting satellites are able to circle the globe approximately once every 101 minutes. This global coverage allows polar systems to provide critical environmental information for initializing Global Forecast Models (GFM) and improving their output. The data from polar-orbiting satellites also provide higher spatial resolution than data from geostationary satellites.

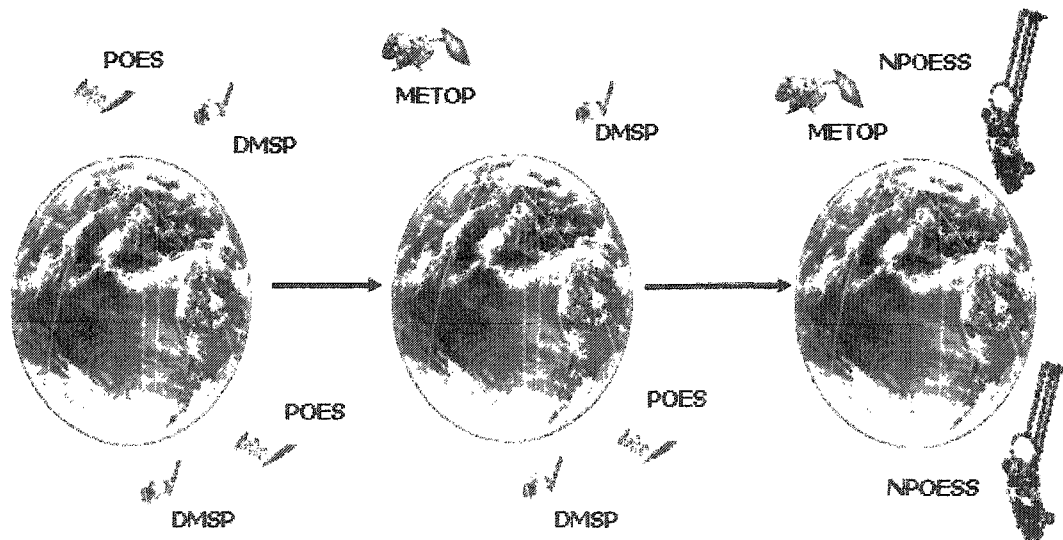


**Figure 1.1:** Evolution of the NPOESS satellite system.

### 1.1.2 Sensors of the NPOESS program

The array of sensors onboard NPOESS will collect and disseminate data about Earth's oceans, atmosphere, land, climate, and space environment. The sensors for the program are both under development and heritage instruments, drawing upon proven technology. These sensors serve to produce Environmental Data Requirement (EDR) products. These data products, and the sensors which measure/determine them are summarized in Table 1.1.

The Visible/Infrared Imager/Radiometer Suite (VIIRS) sensor collects visible and infrared radiometric data of the Earth's atmosphere, ocean, and land surfaces. This sensor is currently under development and is the sensor for which I developed the Cloud Mask methodology explained in Chapter 2. Data types produced from this sensor include atmospheric, clouds, Earth radiation budget, land/water and sea surface temperature, ocean color, and low light imagery.

The Conical Microwave Imager/Sounder (CMIS) instrument is also under development. For the CMIS sensor there are 22 products produced that are relevant to clouds, sea winds, hurricanes, rainfall. Also the CMIS instrument will collect global microwave radiometry and sounding data to produce microwave imagery and other meteorological and oceanographic data.

The Crosstrack Infrared Sounder (CRIS) instrument is under development for the NPOESS program. This sounder will measure the thermal radiation emitted by the Earth's atmosphere to determine the vertical distribution of temperature, moisture, and pressure in the atmosphere.

The Global Positioning System Occultation Sensor (GPSOS) will measure the refraction of radiowave signals from the GPS and Russia's Global Navigation Satellite

System (GLONASS) to characterize the state of the Earth's ionosphere. The instrument is also used for spacecraft navigation.

The Ozone Mapping and Profiler Suite (OMPS) will collect data to permit the calculation of the vertical and horizontal distribution of ozone in the Earth's atmosphere. Also measurements of the ultraviolet radiation will allow the characterization of aerosols over bright snow and ice surfaces.

The Space Environment Sensor Suite (SESS) instrument is dedicated to space physics measurements. SESS will measure neutral and charged particles, magnetic fields, and optical signatures of aurora.

### **1.1.3 NPOESS Data Products**

The data collected by the suite of instruments summarized in Section 1.1.2 above will be processed into Raw Data Records (RDRs), Sensor Data Records (SDRs), Data Products (DPs) and Environmental Data Requirements (EDRs) for use by a number of operational communities. The EDRs are the primary product of the NPOESS sensors. The types of NPOESS EDRs are shown in Table 1.1, in that the first six boxes in the far left column have been assigned top priority by the NPOESS program. In this table the EDRs with asterisks are those that are products of the VIIRS sensor, and other Non-VIIRS generated EDRs produced for NPOESS have no asterisks. The VIIRS Cloud Mask is a component of the Cloud Cover/Layers EDR product listed below. The development of this product is discussed in Chapters 2.

**Table 1.1: NPOESS Environmental Data Records and Imagery Products.**

<b>Atmospheric Vertical Moisture Profile</b>	<b>Downward Longwave Radiance (Surface)</b>	<b>Ozone – Total Column/Profile</b>
<b>Atmospheric Vertical Temp Profile</b>	<b>Electric Fields</b>	<b>Precipitable Water</b>
<b>Imagery *</b>	<b>Electron Density Profile</b>	<b>Precipitation Type/Rate</b>
<b>Sea Surface Temperature *</b>	<b>Energetic Ions</b>	<b>Pressure (Surface Profile)</b>
<b>Sea Surface Winds</b>	<b>Fresh Water Ice *</b>	<b>Sea Ice/Age and Edge Motion *</b>
<b>Soil Moisture *</b>	<b>Geomagnetic Field</b>	<b>Sea Surface Height/Topography</b>
<b>Aerosol Optical Thickness *</b>	<b>Ice Surface Temperature *</b>	<b>Snow Cover/Depth *</b>
<b>Aerosol Particle Size *</b>	<b>In-situ Plasma Fluctuations</b>	<b>Solar Irradiance</b>
<b>Albedo (Surface) *</b>	<b>In-situ Plasma Temperature</b>	<b>Supra-Thermal – Auroral Particles</b>
<b>Auroral Boundary</b>	<b>Insolation</b>	<b>Surface Type *</b>
<b>Auroral Imagery</b>	<b>Ionospheric Scintillation</b>	<b>Surface Wind Stress</b>
<b>Cloud Base Height *</b>	<b>Medium Energy Charged Particles</b>	<b>Suspended Matter *</b>
<b>Cloud Cover/Layers *</b>	<b>Land Surface Temperature *</b>	<b>Total Auroral Energy Deposition</b>
<b>Cloud Effective Particle Size *</b>	<b>Littoral Sediment Transport *</b>	<b>Total Longwave Radiance (TOA)</b>
<b>Cloud Ice Water Path</b>	<b>Mass Loading/Turbidity *</b>	<b>Total Water Content</b>
<b>Cloud Liquid Water</b>	<b>Net Heat Flux *</b>	<b>Vegetation Index/Surface Type *</b>
<b>Cloud Optical Depth *</b>	<b>Net Short Wave Radiance (TOA)</b>	<b>Imagery Product – Cloud Type *</b>
<b>Cloud Top Height *</b>	<b>Neutral Density Profile</b>	<b>Imagery Product – Cloud Cover *</b>
<b>Cloud Top Pressure *</b>	<b>Neutral Winds</b>	<b>Imagery Product – Ice Concentration *</b>
<b>Cloud Top Temperature *</b>	<b>Ocean Color/Chlorophyll *</b>	<b>Imagery Product – Ice Edge location *</b>
<b>Currents (Ocean) *</b>	<b>Ocean Wave Characteristics</b>	<b>Imagery Product– Near Constant Contrast</b>

### 1.1.4 NPOESS Timeline

The NPOESS Timeline is depicted in Figure 1.2 (Cunningham, 2001). In this figure the earliest NPOESS satellite to be launched is in 2008, with the DMSP shown as being phased out, and replaced by the NPOESS system. Also, the NOAA POES system will be replaced by the NPOESS system in 2009. Depicted also are the NASA Earth Observing System (EOS) Terra and Aqua satellites phasing into the NPOESS system. The European Meteorological Operational (METOP) system is shown initially being deployed as part of the NPOESS system of satellites.

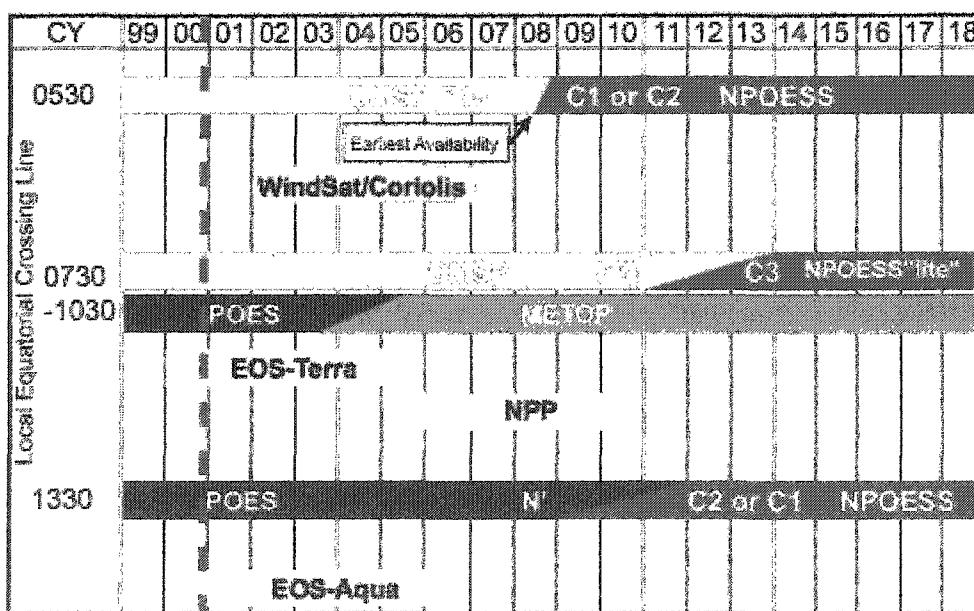


Figure 1.2: NPOESS system timeline.



## 1.2 The VIIRS Sensor System

The VIIRS instrument is briefly described here to clarify the context of the descriptions of the VIIRS Cloud Mask product presented in Chapter 2. The VIIRS can be pictured as a convergence of three existing sensors, two of which have historically seen extensive operational use. These three sensors are the DoD Operational Linescan System (OLS), the NOAA Advanced Very High Resolution Radiometer (AVHRR), and the NASA Moderate Resolution Imaging Spectroradiometer (MODIS) Sensor.

The OLS is the operational visible/infrared scanner for the Department of Defense (DoD). Its unique strengths are controlled increasing in spatial resolution through rotation of the ground instantaneous field of view (GIFOV) and the existence of a Low-Level Light Sensor (LLLS) capable of detecting visible radiation at night. OLS has primarily served as a data source for manual analysis of imagery. The AVHRR is the operational visible/infrared sensor flown on the National Oceanic and Atmospheric Administration (NOAA) Television Infrared Observation Satellite (TIROS-N) series of satellites. Its unique strengths are low operational and production cost and the presence of five spectral channels that can be used in a wide number of combinations to produce operational and research products. Figure 1.3 compares the VIIRS bandset to that of the heritage AVHRR and OLS sensors.

## *Imagery EDR Benefits from True Multispectral Capability*

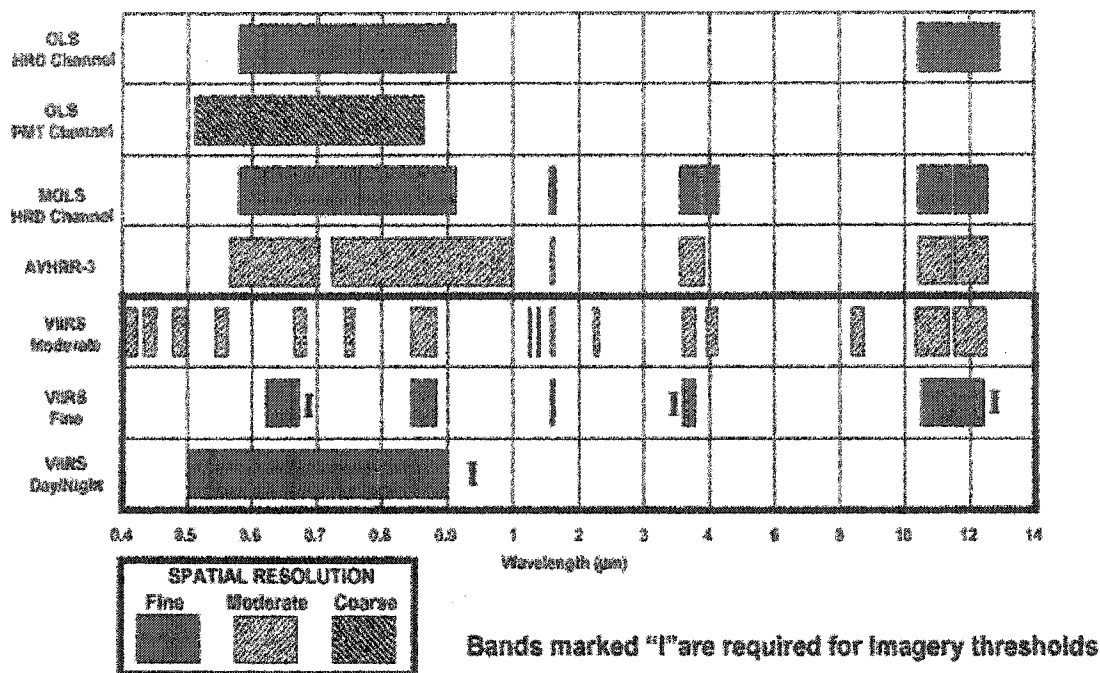


**Figure 1.3:** Comparison of the VIIRS imagery bandset with heritage sensors.

In December 1999, the National Aeronautics and Space Administration (NASA) launched the Earth Observing System (EOS) morning satellite, *Terra*, which includes the Moderate Resolution Imaging Spectroradiometer (MODIS). This sensor possesses an unprecedented array of thirty-two spectral bands at resolutions ranging from 250 m to 1 km at nadir, allowing for unparalleled accuracy in a wide range of satellite-based environmental measurements.

The VIIRS sensor will reside on a platform of the National Polar-orbiting Operational Environmental Satellite System (NPOESS) series of satellites. It is intended to be the product of a convergence between DoD, NOAA and NASA in the form of a single visible/infrared sensor capable of satisfying the needs of all three communities, as well as the research community beyond. As such, VIIRS will require three key

attributes: high spatial resolution, minimal production and operational cost, and a large number of spectral bands to satisfy the requirements for generating accurate operational and scientific products.

Illustrated in Figure 1.4 is the design concept for the VIIRS instrument, to be designed and built by Raytheon Santa Barbara Remote Sensing (SBRS). At its heart is a rotating telescope scanning mechanism that minimizes the effects of solar impingement and scattered light. Calibration is performed onboard using a solar diffuser for short wavelengths and a V-groove blackbody source and deep space view for thermal wavelengths. A solar diffuser stability monitor is also included to track the performance of the solar diffuser. The nominal altitude for NPOESS will be 833 km. The VIIRS scan will extend to 56 degrees on either side of nadir.

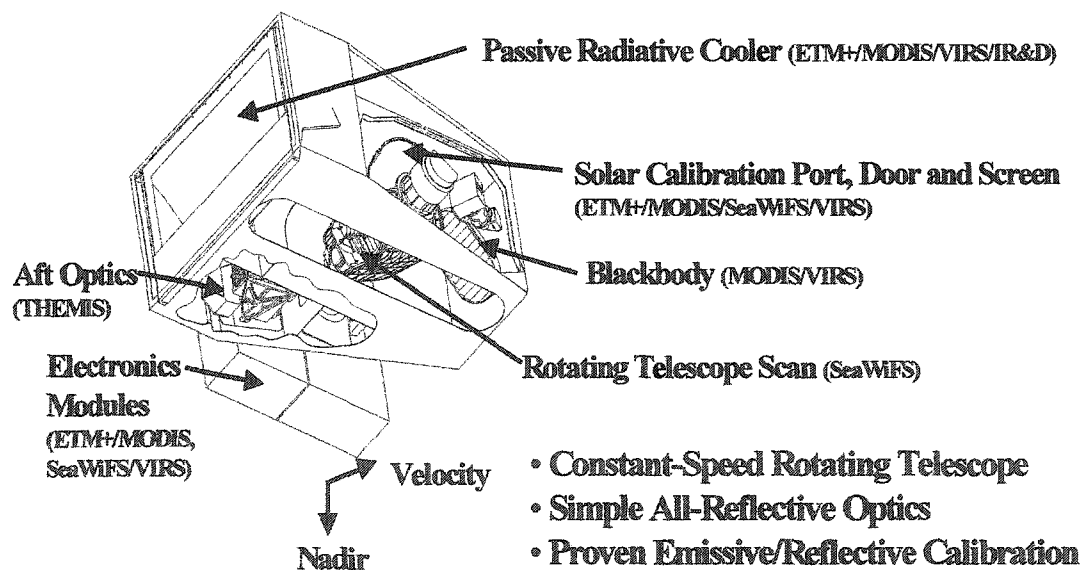


**Figure 1.4:** Summary of VIIRS design concepts and heritage.

The VIIRS Sensor Requirements Document (SRD) places explicit requirements on spatial resolution for the Imagery EDR. Specifically, the horizontal spatial resolution (HSR) of bands used to meet threshold Imagery EDR requirements must be no greater than 400 m at nadir and 800 m at the edge of the scan. This led to the development of a

unique scanning approach which optimizes both spatial resolution and signal-to-noise ratio (SNR) across the scan. The nested lower resolution radiometric bands follow the same paradigm at exactly twice the size. The VIIRS detectors are rectangular, with the smaller dimension projecting along the scan. At nadir, three detector footprints are aggregated to form a single VIIRS “pixel”, illustrated in Figure 1.5. Moving along the scan away from nadir, the detector footprints become larger both along track and along scan, due to geometric effects and the curvature of the Earth. The effects are much larger along scan. At around 32 degrees in scan angle, the aggregation scheme is changed from 3x1 to 2x1. A similar switch from 2x1 to 1x1 aggregation occurs at 48 degrees. The VIIRS scan consequently exhibits a pixel growth factor of only two both along track and along scan, compared with a growth factor of six along scan which would be realized without the use of the aggregation scheme.

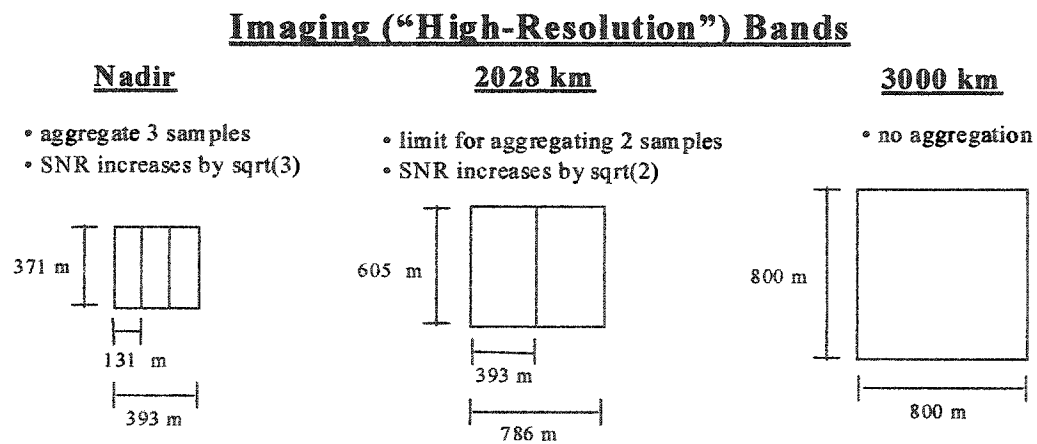


**Figure 1.5:** Summary of VIIRS imaging bands design.

### 1.3 The VIIRS Sensor Bandset

The VIIRS sensor has a total of 22 bands which may be broken down to subsets of 6 high resolution imagery bands, and 18 radiometric bands. Imagery bands are higher resolution (371 m) than the radiometric bands (742 m), and have primary uses in sea ice and cloud typing applications and use for imagery analysts to discern surface features. While radiometric bands are used in the suite of VIIRS algorithms to retrieve VIIRS EDRs.

Similarly the VIIRS bandset may be broken down into the spectral regions the bands span. The bandset may be subdivided into the Visible-Near-Infrared (VNIR), Short Wave Infra-Red (SWIR), Mid-Wave-Infra-Red (MWIR), and Long Wave Infra-Red (LWIR) spectral regions. Each of these regions, and the VIIRS bands which span them will be discussed briefly.

#### 1.3.1 The VNIR VIIRS Sensor Bandset

The positioning of the VIIRS spectral bands in the VNIR spectral region are summarized in Figure 1.6. Radiation in this spectral region is solar in origin, and therefore there exists a great dependence upon the solar zenith angle. The spectral region between 400 and 600 nm are the limitation of human vision, so even across the VNIR region, which spans 300 to 1000 nm, there are spectral features and reflectances undetectable to the naked eye require sensors to discern them.

Figure 1.6 is a depiction of the reflectances of snow, vegetation, water, and non-vegetated soil across the VNIR spectral region. Across much of the VNIR region most materials have a low reflectance, high absorption, except for in the longer wavelength regions. The most pronounced effect for a variety of materials is the decrease with longer wavelength of snow surface reflectance, the linear increase of reflectance with

wavelength of non-vegetated soil, the dramatic increase in the reflectance of vegetated regions between 600 nm and 800 nm, and the uniform low reflectance of water surfaces across the VNIR.

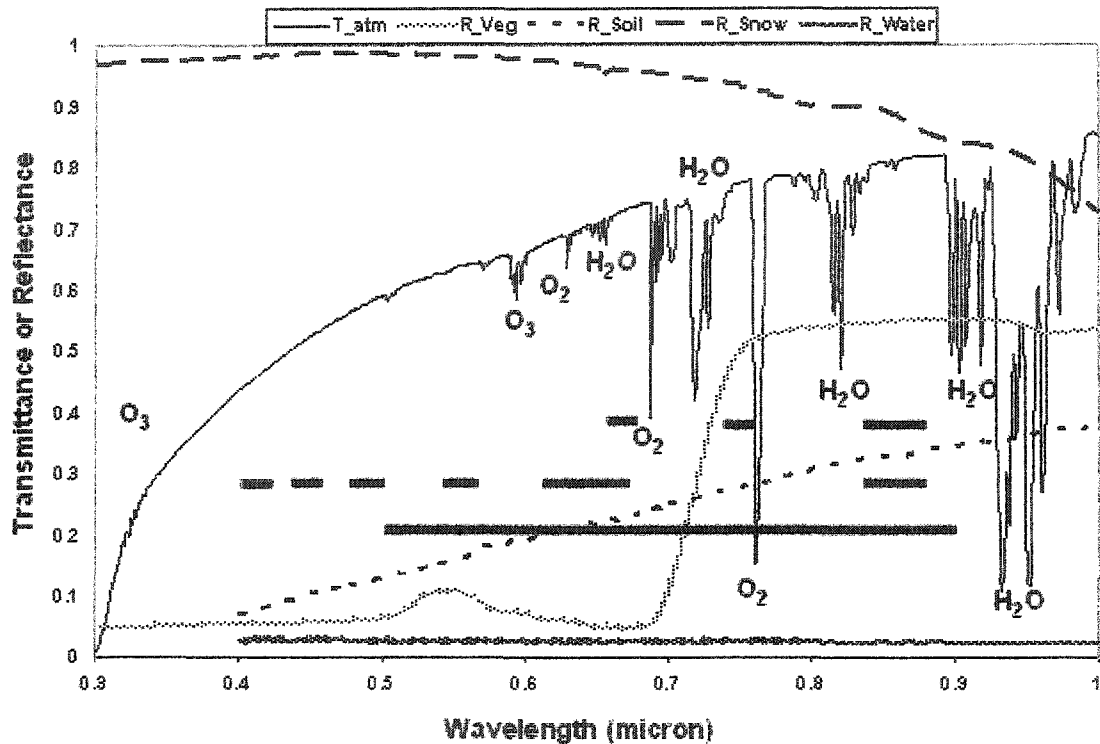


**Figure 1.6:** The VIIRS VNIR spectral bands. Bands are depicted by solid straight lines. Also illustrated are the surface reflectance of water, vegetated surfaces, snow, and non-vegetated soil. Atmospheric absorption features, and the molecules responsible are noted in this figure by labeling of the species responsible, and by the resultant drops in the atmospheric transmission (solid curve).

There are various important atmospheric effects across the VNIR region. Aerosols have a increase in their scattering effect as one goes from higher to lower wavelengths across this region. Clouds also scatter uniformly across this region, with similar reflectance properties to the snow reflectance curve in Figure 1.6. Additionally,

molecular scattering, which is commonly referred to as Rayleigh scattering also has an increase in magnitude as one goes to the smaller wavelengths.

Atmospheric absorption, the solid curve depicted in Figure 1.6, illustrates the absorbing properties of various atmospheric molecules across this spectral region. Where the solid line drops in magnitude there is an absorption feature of a specific atmospheric molecule encountered. Some atmospheric absorption features worth mentioning across the VNIR region. The first feature is at the lower wavelength region of the VNIR, the primary ozone absorption features are at the edge of the Ultraviolet (UV-B and UV-A) spectral regions of ozone, which leads to the drop in atmospheric transmission less than 400 nm in Figure 1.6. There are also additional weaker ozone absorption features near 580 nm in the Chapius bands. There are additional features across the VNIR region, with the oxygen absorption features at 760 nm, and the various water vapor features about 700, 820, and 945 nm being most prominent. Absorption regions exist due to discrete vibration bands in which solar radiation is absorbed by molecules across this spectral region. Energy absorbed by molecules and the surfaces in the solar region of the spectrum leads to warming and produces the surface and atmospheric temperature characteristics.

The VIIRS sensor bandset across the VNIR have various uses, dependent upon the atmospheric properties and surface reflectances in the spectral regions within their bandwidth. The three bands at wavelengths less than 500 nm have two predominant uses, one is in ocean color retrievals, and additional algorithms use this region for atmospheric aerosol retrievals. Phytoplankton and blue-green algae are detectable in this region using these bands, in addition to turbidity in the water. Of note is that ocean-color retrieval algorithms have also benefited from using bands near 550, 680, and 750 nm, whereas aerosol retrieval algorithms have primarily used the shorter wavelength bands. Vegetation amount is commonly inferred from the Normalized Differential Vegetation Index (NDVI) based on the low reflectance 650 nm band and the higher reflectance 850 nm band to discern vegetated areas. The bands near 650 and 850 nm

have additional uses in retrieving the optical depth of clouds. Across this spectral region there are additional bands which are used in cloud detection, the discussion of these bands will be done in Chapter 2. Sensors such as MODIS, use the 945 nm spectral region to retrieve atmospheric water vapor amounts. VIIRS however does not have requirements to produce this product, and thus lacks bands in this spectral region. The use of this spectral region for water vapor retrieval will be discussed in Chapter 4.

### 1.3.2 The SWIR VIIRS Sensor Bandset

The positioning of the VIIRS spectral bands in the SWIR spectral region are summarized in Figure 1.7. Radiation in this spectral region (1000 – 3000 nm) is primarily solar in origin. One exception to this rule is for very hot regions, i.e. forest fires, which can be hot enough to emit radiation, according to Planks Law at the longer wavelengths in this spectral region. The entire SWIR spectral region are beyond the upper wavelength limits of human vision, making the spectral features and reflectances invisible to the human eye and undetectable without sensors to identify them.

Figure 1.7 is a depiction of the reflectances of snow, vegetation, water, and non-vegetated soil across the SWIR spectral region. Across much of the SWIR region most materials have a decrease in reflectance with increasing wavelength, resulting in higher absorption, except for primarily non-vegetated surface types. The most pronounced atmospheric absorption effects across this spectral region are the numerous water vapor absorption regions, these are called ‘dirty windows’. Atmospheric water vapor absorption features are notable in Figure 1.7 near 1180, 1375, 1900, and 2600 nm. In these ‘dirty windows’ minimal solar radiation reaches the surface and is reflected back to satellite borne sensors. Thus, measured radiation in these spectral regions is used primarily for atmospheric, rather than for surface property retrieval. In contrast to these dirty window spectral regions are the ‘window’ regions in which atmospheric absorption



is minimal. These regions allow one to measure surface properties with minimal atmospheric attenuation.

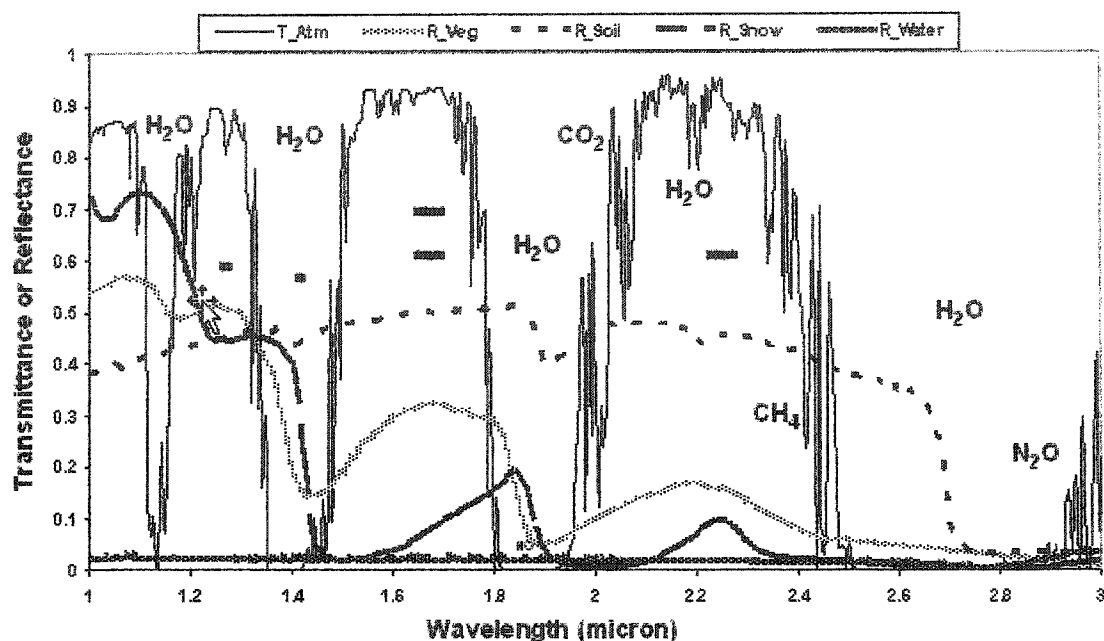


**Figure 1.7:** The VIIRS SWIR spectral bands. Bands are depicted by solid straight lines. Also illustrated are the surface reflectance of water, vegetated surfaces, snow, and non-vegetated soil. Atmospheric absorption features, and the molecules responsible are noted in this figure by labeling of the species responsible, and by the resultant drops in the atmospheric transmission (solid curve).

The SWIR spectral region has been primarily exploited for cloud effective particle size retrieval, cloud detection, and cloud phase/type. Additionally, this region has been used to discern surface snow cover using a Snow Differential Index (SDI), analogous to the NDVI in the visible spectral region, using the lower reflectance of snow near 1600 nm and the higher reflectance in the VNIR to discriminate surface snow cover.

There are additional important atmospheric effects across the SWIR region, aside from the dirty windows and window regions previously mentioned. Clouds have similar reflectance properties similar to those depicted for snow, with a general lower

reflectance that depends upon the clouds particle size. In the SWIR window regions clouds are easily discernable from snow. This will be discussed in more detail in Chapter 2. Methane has weak atmospheric absorption features located near 1600 and stronger features near 2200 nm. These features will be discussed and used in Chapter 5. Aerosols have a increase in their scattering effect as one goes from higher to lower wavelengths across this region, but their scattering is much less than in the VNIR spectral region.

The VIIRS sensor bandset across the SWIR have various uses, dependent upon the atmospheric properties and surface reflectances in the spectral regions within their bandwidth. The band located near 1200 nm has uses in discerning ice age and type, and additional applications in retrieving cloud particle size. The band near 1375 nm has a primary use in detecting thin cirrus clouds, which reflect radiation back to space before it encounters the atmospheric water vapor beneath the high cirrus clouds. The bands located in the 1600 and 2200 nm window regions are primarily used for cloud detection over snow and ice surfaces, and have uses in cloud typing of imagery.

### **1.3.3 The MWIR VIIRS Sensor Bandset**

The Mid-Wave-Infra-Red spectral region is between 3000 and 5000 nm, depicted in Figure 1.8. This spectral region is also referred to as the ‘crossover region’ because the solar radiation decreases while the thermal infrared radiation increases with wavelength here. With both thermal and solar radiation components in this spectral region there are both thermal and solar uses of the radiation field. During the daytime the solar radiation component in this spectral region disappears, while the thermal radiation component is always present.

Surface reflectance of a majority of surface types across this spectral region is uniformly low, illustrated in Figure 1.8. However, the exception is the reflectance of non-vegetated soils regions. Another property in addition to reflectance that may be

used in the thermal regions of the spectrum is the emissivity. The emissivity is the degree to which a surface adheres to being a black body, for which emissivity is unity and the surface emits following Planck's law (a perfect black body). The sum of emissivity and reflectivity of a surface equals one for a non-transmissive surface. This allows the use of both of these properties in studying atmospheric and surface interactions and effects.

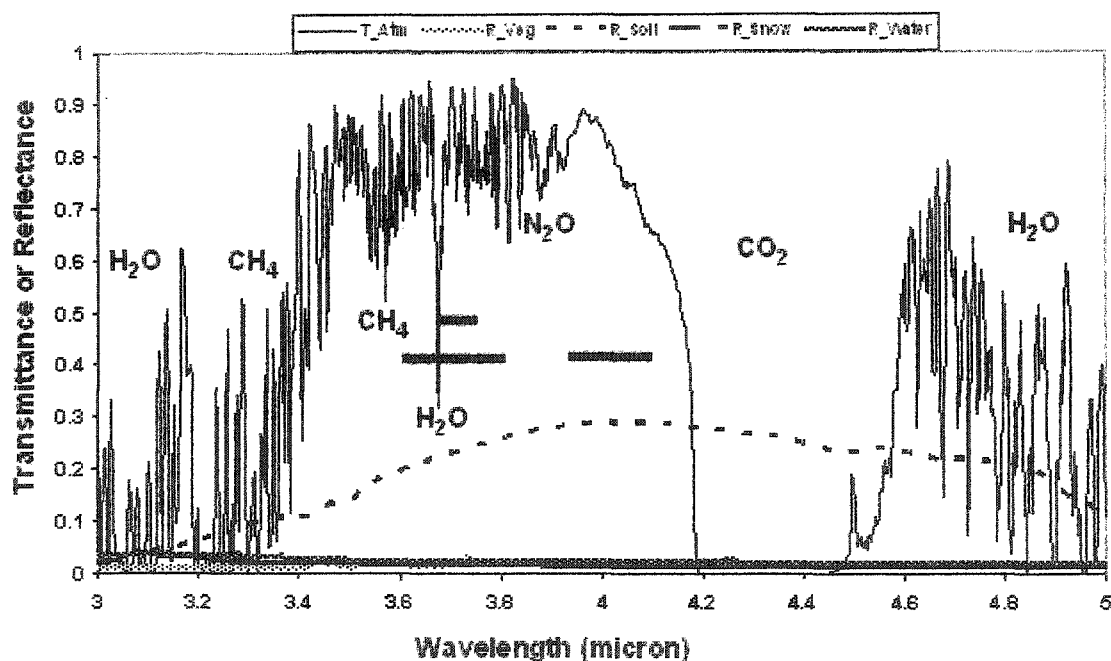


**Figure 1.8:** The VIIRS MWIR spectral bands. Bands are depicted by solid straight lines. Also illustrated are the surface reflectance of water, vegetated surfaces, snow, and non-vegetated soil. Atmospheric absorption features, and the molecules responsible are noted in this figure by labeling of the species responsible, and by the resultant drops in the atmospheric transmission (solid curve).

The absorption features across the MWIR are caused by both vibrational and rotational absorption bands. The most notable features across the region are dirty windows from water vapor (near 3100 and 4800 nm), from methane (3300 nm) and the strong carbon dioxide dirty window absorption region near 4300 nm. These features

both absorb solar radiation, and additionally absorb the thermal radiation emitted by the Earth's surface and atmosphere.

The VIIRS MWIR bandset are used for surface temperature retrieval, for snow/ice detection, for ocean current retrieval, for forest fire detection, for cloud type determination, and for cloud detection. The cloud detection bands usage is based primarily upon spectral differences in solar radiation, and is discussed more in Chapter 2.

#### **1.3.4 The LWIR VIIRS Sensor Bandset**

The Long-Wave-Infra-Red spectral region is between 5000 and 15000 nm, depicted in Figure 1.9. This spectral region consists of entirely emissive thermal radiation and unlike the other spectral regions considered there is no solar radiation. The amount of emitted thermal radiation is depends upon Plank's law, with variations a result of atmospheric absorption and spectral emissivity differences. During day and night the thermal radiation across the LWIR is always present.

Surface emissivity is considered across this spectral region as opposed to reflectance in the other spectral regions discussed. The emissivity of a majority of surface types across this spectral region is uniformly high as illustrated in Figure 1.9. However, the exception is the spectrally lower emissivity of non-vegetated soils regions. Additionally clouds have a spectrally varying emissivity across the LWIR region.

The absorption features across the LWIR are caused by rotational molecular absorption features. These features are illustrated in Figure 1.9. The most notable features across the region are dirty windows from water vapor (from 5000 – 8000 nm), from the carbon dioxide dirty window absorption region (wavelengths longer than 13000 nm) and from a sharp ozone absorption feature (9600 nm). These features absorb the thermal radiation emitted by the Earth's surface and atmosphere. The window

regions near 8600, and 10000-12000 nm allow thermal radiation to escape from the Earth's surface and atmosphere to space.

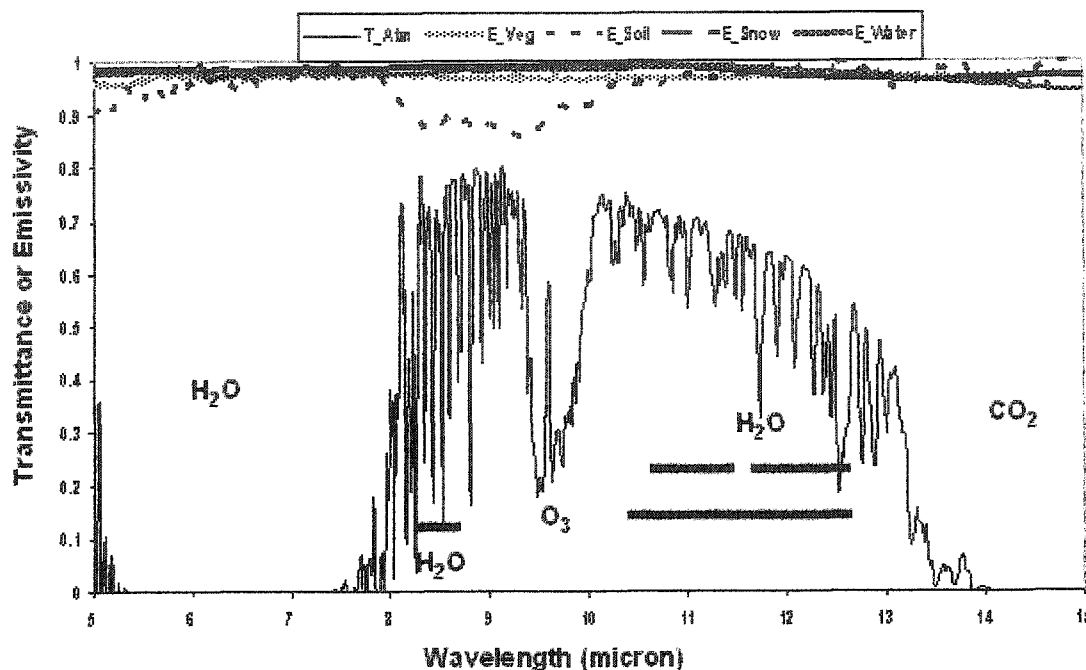


**Figure 1.9:** The VIIRS LWIR spectral bands. Bands are depicted by solid straight lines. Also illustrated are the surface emissivity of water, vegetated surfaces, snow, and non-vegetated soil. Atmospheric absorption features, and the molecules responsible are noted in this figure by labeling of the species responsible, and by the resultant drops in the atmospheric transmission (solid curve).

The VIIRS LWIR bandset is used for surface temperature retrieval, for snow/ice detection, for ocean current retrieval, for forest fire detection, for cloud type determination, and for cloud detection. The cloud detection bands usage is based primarily upon spectral differences in cloud emissivity, and is discussed more in Chapter 2.

#### 1.4 The MODIS Airborne Simulator Sensor

The MODIS Airborne Sensor (MAS) has been used extensively in the development of the VIIRS Cloud Mask EDR, discussed in Chapter 2. Data acquired by the MAS have in the past been used to define, develop, and test algorithms for the MODIS sensor, a key sensor of NASA's Earth Observing System (EOS). The VIIRS system has bands which are highly MODIS-like, therefore the MAS data has been used in developing the VIIRS algorithms as well, serving as VIIRS surrogate data in the absence of full simulation capabilities.

The MODIS Airborne Simulator (*King et al., 1992; King et al., 1996*) is a modified Daedalus Wildfire scanning spectrometer which flies on a NASA Experimental Research (ER-2) high altitude research aircraft and provides spectral information similar to that which is now provided by the MODIS instrument on the EOS platform.

Since 1992 the MAS has been flown in a series of experiments that have lasted on average 2-8 weeks, with anywhere from 5-15 flights conducted during each experiment. These experiments have been flown all over the world collecting an abundance of data over many varying surfaces and varying atmospheric conditions.

The MAS spectrometer acquires high spatial resolution imagery in the spectral range between 0.4 and 14.3 microns. A total of 50 spectral bands are available in this range. A 50-channel digitizer records all 50 spectral bands at 16 bit. The MAS spectrometer is mated to a scanner sub-assembly which collects image data with an Instantaneous Field of View (IFOV) of 2.5 mrad, giving a ground resolution of 50 m from 20 km altitude, and a cross track scan width of 85.92 degrees. A summary of the MAS instrument is presented in Table 1.2, and examples of MAS imagery is presented in both Chapters 2 and 3.

**Table 1.2: Description of the MAS Instrumentation.**

Platform:	NASA ER-2 aircraft
Ground Speed:	400 kts (206 m/s)
Altitude:	20 km (nominal)
Pixel Spatial Resolution:	50 m (at 20 km altitude)
Pixels per Scan Line:	716 (roll corrected)
Scan Rate:	6.25 scans/s
Swath width:	37.25 km or 22.9 mi (at 20 km altitude)
Total Field of View:	85.92°
Instantaneous Field of View:	2.5 milliradians
Roll Correction:	Plus or minus 3.5 degrees (approx)
Data Channels:	50 (16-bit resolution)
Spectral Bands:	Port 1: 09 bands from 0.529 - 0.969 $\mu\text{m}$ Port 2: 16 bands from 1.595 - 2.405 $\mu\text{m}$ Port 3: 15 bands from 2.925 - 5.325 $\mu\text{m}$ Port 4: 09 bands from 8.342 -14.521 $\mu\text{m}$
Data Rate:	246 Megabytes/hr
Visible Calibration:	Integrating sphere on the ground
Infrared Calibration:	Two black bodies on board

## 1.5 Algorithms Developed for Future Sensors

For the VIIRS sensor the author has developed the cloud detection algorithm, which will be discussed in detail in Chapter 2. The cloud detection algorithm has been developed and validated, along with flowdown of the error budget and effects of band-to-band mis-registration upon cloud detection for the VIIRS sensors algorithmic suite.

A cloud detection algorithm is needed to identify the cloudy and clear pixel regions in imagery. Once clear regions are discriminated from cloud regions then additional processing can be performed upon each of them to generate VIIRS products. For the regions identified as cloud-covered additional cloud processing algorithms are available to determine cloud phase, cloud effective particle size, cloud optical depth, cloud top height, and cloud base height, and to generate VIIRS Cloud EDR products. For regions identified as being clear atmospheric and surface processing algorithms are available. The atmospheric processing algorithms generate aerosol optical property and aerosol type products. The surface processing algorithms determine surface type, albedo, vegetation detection, snow/ice surface detection, surface temperature, ocean current retrieval, lead detection, sea ice detection, ocean color detection, and snow/ice imagery product development.

Two new techniques of retrieving atmospheric information, to be applied on future satellite remote sensing platforms, have been developed as part of this thesis. The first of these new techniques improve upon current MODIS water vapor retrieval algorithms under hazy atmospheric conditions by making use of cloud shadowed regions. This work is presented in Chapter 4. The second method employs regions of sun glint to retrieve total atmospheric and surface methane amounts. This work is presented in Chapter 5.



## Chapter 2

### The VIIRS Cloud Mask

#### 2.0 Introduction

This chapter consists of excerpts from the VIIRS Cloud Mask (VCM) Algorithm Theoretical Basis Document (ATBD) (*Larsen, 2000a*), a document which explains the theoretical background required to derive the Environmental Data Requirement (EDR) of the VCM. This EDR is a binary cloudy/not cloudy flag, which is a required segment of the Cloud Cover/Layers EDR (*NPOESS IPO, 2000*). In addition, this chapter provides an overview of the required input data, a description of how cloud detection is performed for VIIRS, examples of cloud detection, and a description of the error budget for the described algorithm. The cloud mask described in this chapter is part of the Cloud Cover/Layers EDR developed for the National Polar Orbiting Environmental Satellite System (NPOESS)/VIIRS software package of EDRs. Parameters relevant to the EDR VCM are displayed in Table 2.2.

#### 2.1 Overview

This chapter covers the theoretical basis for the generation of the VIIRS EDR VCM Algorithm. Sections 2.1.1 and 2.1.2 give an overview of the cloud mask objectives. Section 2.1.4 describes the VCM, its input data, the theoretical background, and some practical considerations. Section 2.4 provides an overview of the error budget and simulation results, and Section 2.5 shows validation examples for the VCM.

### 2.1.1 Cloud Mask Definition

In the VIIRS Sensor Requirements Document (*NPOESS IPO*, 2000) the Cloud Cover/Layers EDR is outlined and explained as follows.

Cloud cover/layers EDR consists of two data products:

- (a) fractional cloud cover, defined as the fraction of a given area on the Earth's surface for which a locally normal line segment extending between two given altitudes intersects a cloud, and
- (b) a binary (cloudy/not cloudy) map at the pixel level indicating which pixels are deemed to contain clouds. This is a specification which the cloud detection algorithm fills in.

As a threshold, fractional cloud cover is required for up to four layers of the atmosphere between the surface and an altitude of 20 km. As an objective, cloud cover is required for contiguous, 0.1 km thick layers at 0.1 km increments in altitude, from the surface of the Earth to an altitude of 30 km.

Table 2.1 below depicts the Cloud Cover/Layers EDR requirements. The cloud mask is the probability of correct typing (binary map) section of Table 2.1. With no threshold or objective probability of correct typing values specified by the VIIRS SRD (*NPOESS IPO*, 2000) the government asked for the developers to assign specifications for the probability of correct typing. These values are provided in Section 2.5.

**Table 2.1: VIIRS Cloud Cover/Layers/ Mask EDR.**

Para. No.	Field	Thresholds	Objectives
	a. Horizontal Cell Size		
V40.4.2-11	1. Fractional cloud cover	25 km	2 km
V40.4.2-12	2. Binary Map	pixel size	(TBD)
V40.4.2-2	b. Horizontal Reporting Interval	To Be Determined (TBD)	(TBD)
	c. Vertical Cell Size	N/A	N/A
V40.4.2-3	d. Vertical Reporting Interval (fractional cloud cover)	Up to 4 layers	0.1 km
V40.4.2-4	e. Horizontal Coverage	Global	Global
V40.4.2-5	f. Vertical Coverage	0 - 20 km	0 - 30 km
V40.4.2-6	g. Measurement Range	0 - 1.0	0 - 1.0
V40.4.2-14	1. Fractional cloud cover	0 - 1.0	0 - 1.0
V40.4.2-15	2. Binary map	Cloudy/not cloudy	Cloudy/not cloudy
V40.4.2-7	h. Measurement Accuracy (fractional cloud cover)	0.1	0.05
V40.4.2-8	i. Measurement Precision (fractional cloud cover)	0.15	0.025
V40.4.2-13	n. Probability of Correct Typing (binary map)	> (TBD) at 95 % To Be Resolved (TBR) confidence level	> (TBD) at 95 % (TBR) confidence level
V40.4.2-9	j. Mapping Uncertainty	4 km	1 km
	k. Maximum Local Average Revisit Time	6 hrs	4 hrs
	l. Maximum Local Refresh	(TBD)	(TBD)
V40.4.2-10	m. Minimum Swath Width (All other EDR thresholds met)	3000 km (TBR)	(TBD)

### 2.1.2 Objective of the Cloud Mask

The objective of the VCM is to determine if a given Field of View (FOV) has a cloud present. The VCM is defined as the pixel level flag which indicates when a line segment extending between the sensor and a given area of the Earth's surface is intersected by a cloud. The cloud mask EDR is a binary cloudy/not cloudy flag operating at the pixel level using VIIRS radiance data. Aggregation of the cloud mask to a larger HCS is performed to retrieve the Cloud Cover/Layers EDR. The VCM operates at a radiometric pixel resolution (742 m), and at the imagery pixel resolution (371 m), at nadir along the scantrack. It should be noted that not only is the VCM an EDR, but it is crucial as a first step in evaluating any scene before further processing is begun to retrieve the many other VIIRS EDRs. Also generated by the VCM, in addition to the binary cloudy/not cloudy EDR, are many processing flags and test result indicators, which are used by other EDRs in the VIIRS processing architecture.

### 2.1.3 Historical Perspective on Cloud Detection

Cloud masking, or screening, involves the discrimination between clear and cloudy pixels within an image. Excellent reviews of the many cloud detection methods can be found in the literature (*Ackerman et al.*, 1997; *Hutchison and Hardy*, 1995; *Saunders and Kriebel*, 1988; *Stowe et al.*, 1995; *Goodman and Henderson-Sellers*, 1988; and *Rossow*, 1989). The methods used in detecting clouds are generally based upon radiance and Brightness Temperature (BT) thresholding and statistical techniques which make use of the spectral and textural features in the imagery. The radiance and BT thresholding techniques performed by the VCM work on a pixel-by-pixel basis. Single or multi-channel thresholds are used to discriminate clear from cloudy pixels. Thresholding tests performed by the VCM have a heritage from the NOAA Clouds from

AVHRR tests (CLAVR) and the NASA MODIS program. Statistical techniques use groups of adjacent pixels to recognize cloud apparent behavior.

#### 2.1.4 Cloud Mask Algorithm

The VCM is essentially derived from the MODIS Cloud Mask (MCM) multi-channel cloud masking techniques (*Ackerman et al.*, 1997), which in turn have their heritage in other algorithms. These include the Support of Environmental Requirements for Cloud Analysis and Archive (SERCAA) algorithm (*Gustafson et al.*, 1994), and the Clouds from AVHRR-Phase I (CLAVR-1) algorithm (*Stowe et al.*, 1998). The heritage technology that the VCM is based on uses the most recent advancements in cloud detection techniques. This research has been conducted by the MODIS cloud research team at the University of Wisconsin, headed by Dr. Steve Ackerman, and the CLAVR-2 algorithm team at NOAA, lead by Dr. Larry Stowe of the NPOESS Integrated Project Office (IPO). A third cloud mask has been developed specifically for cloud detection in the cryosphere. This cloud mask was developed for the Global Imager (GLI) instrument on the Advanced Earth Observing Satellite (ADEOS-2) satellite (*Stammes*, 1999; *Stammes*, 2003). When new cloud detection techniques are developed and proven to be effective, the modularized coding of the VCM will allow for these techniques to be added.

##### 2.1.4.1 Inputs to the Cloud Mask

The inputs to the VCM algorithm are listed in Table 2.2. Additional ancillary data inputs are shown in Table 2.4. The spectral radiance is required for cloud thresholding tests. Within the VCM the radiances, reflectances (for solar bands at wavelengths less than 5  $\mu\text{m}$ ), and Brightness Temperature (BT) (for bands at wavelengths longer than 2  $\mu\text{m}$ ) for each band are needed for cloud tests. Normalized incident Top of Atmosphere

(TOA) irradiance and sun/sensor geometries (terrain-referenced geometric parameters) are required for determination of TOA reflectances, and identification of regions susceptible to sun glint effects. The retrieval quality indicators are relevant to the quality of the sensor data in Table 2.2 being used by the VCM for cloud detection. They indicate that the respective input data are suspect.

**Table 2.2:** Parameters for the VCM product.

<b>Name</b>	<b>Units</b>	<b>Definition/Comments</b>
Spectral radiance (L)	W/(m <sup>2</sup> sr μm)	Radiant energy per time-area-solid angle wavelength interval
Brightness Temperature (BT)	K	Brightness temperature for a given channel of the sensor, derived from spectral radiance.
Equivalent reflectance (ρ <sub>equiv</sub> )	None	$\pi \times L$ divided by normal incidence TOA irradiance
Normal incident TOA Irradiance	W/(m <sup>2</sup> μm)	Normalized incident TOA irradiance in specific channel
Terrain-referenced geometric parameters	Deg	Solar- and observer geometry, solar and sensor zenith and azimuthal angles.
Retrieval quality indicators	vary	Determine the quality assessment of the VCM

Not all bands of the VIIRS are used in the VCM for cloud detection. A list of the bands which are used by the VCM are given in Table 2.3. The radiometric parameters of these bands listed in Table 2.2 are required for operation of the VCM. The spectral response functions and additional information about the bandset below are described in chapter one. The band names listed in Table 2.3 are from the pre-PDR (Preliminary Design Review) of the VIIRS sensor. These band names are subject to change in the future VIIRS sensor development, however the band center and Bandwidth (BW) is considered to be fixed.

**Table 2.3:** The VIIRS channels used by the VCM.

<b>Band</b>	<b>Center <math>\lambda</math> (<math>\mu\text{m}</math>)</b>	<b>Bandwidth (<math>\mu\text{m}</math>)</b>
DNB	0.7000	0.4000
5i	0.6450	0.0500
OC2	0.6720	0.0200
6i	0.8650	0.0390
6r	0.8650	0.0390
7	1.3780	0.0150
8i	1.6100	0.0600
8r	1.6100	0.0600
10iw	3.7400	0.3800
10r	3.7000	0.1800
SST2	4.0500	0.1550
SST4	8.5500	0.3000
11	10.7625	1.0000
12iw	11.4500	1.9000
12r	12.0125	0.9500

**Table 2.4:** Ancillary VIIRS data for the VCM.

<b>Input Data</b>	<b>Source of Data</b>
Land/Water Tag	EROS Data Center
Ecosystem Map	Olson/Loveland
Topographical Map	USGS/EDC
Radiometric Quality Indicator	VIIRS
Most Recent Snow/Ice Map	VIIRS/CMIS/RADARSAT
Sun/Sensor Geometry	VIIRS
Geolocation Data	VIIRS

Table 2.4 lists the required ancillary data. The following section explains all of the input ancillary data in greater detail.

The VCM requires a land/water map, which is sometimes referred to as a land/water tag, to discriminate land from water. Land and water possess different surface reflective properties. These properties affect the thresholds applied in discriminating clear sky from cloud. The best quality land/water map available will be used. Presently the VCM uses the 1 km resolution world map provided from the Earth Research Environmental Systems (EROS) Data Center (EDC). A possible future solution is to use the data product generated by the MODIS instrument. After launch it is hoped that a VIIRS land/water surface product is available for use.

A global ecosystem map is required to discriminate different land types. Various land types possess different reflective properties. The reflective properties need to be known to properly develop and identify the correct thresholds to be applied in cloud tests. The Olson map of ecosystems (*Olson et al.*, 1994) at 10 minute resolution is used for global processing. Tom Loveland's ecosystem map (*Loveland et al.*, 1991) at 1 km resolution is applied, while over North America. The MODIS land cover classification is planned to be used in future development stages for this algorithm. Once NPOESS is operating, and global data are being acquired and updated regularly, the VIIRS Surface Type EDR (*Brown De Coulston*, 2000) can be applied, which at this level will be an Intermediate Product (IP).

Presently, a topographical map is not used by the VCM. However, in the future, a topographical map, or Digital Elevation Model (DEM) may be applied to assist in defining rugged versus plateau terrain. This is needed to determine the pixel elevation, define terrain type, identify topographically induced shadowing, modify surface reflectances, and to assist in cloud versus snow/ice cover discrimination. The plan is to use the United States Geological Survey GTOPO30 (USGS/EDC) DEM, with approximately 1 km resolution, in the future. The quality of the topographical data, and the methodology utilized, will be developed with a heritage of MODIS technology.

The radiometric quality of the input radiances are described by the Radiometric Data Quality Indicator (RDQI). The sensor provides the RDQI to the VCM. A



threshold of RDQI >1 must be obtained to start the VCM retrieval procedure. This RDQI differs from the quality indicators mentioned in Table 2.2 in that the other quality indicators pertain more to input data results than just the radiometric quality, of which the RDQI is an indicator.

For the VCM, snow/ice discrimination is required. This snow/ice map is needed to decide which cloud detection tests will be applied, and also to adjust thresholds applied over snow/ice surfaces. Spectrally, snow/ice and clouds have many similar features. A snow/ice map will decrease the misclassification of snow/ice as clouds. Presently the VCM uses a Normalized Differential Ice Index (NDII) snow/ice threshold detection technique (*Hall et al.*, 1996). The snow/ice mask is planned to be a combined result of the Conical Scanning Microwave Image/Sounder (CMIS) snow cover EDR, the CMIS fresh water ice EDR, the CMIS sea ice edge motion EDR, the VIIRS snow cover EDR, the VIIRS fresh water ice EDR, the thresholding techniques developed by MODIS, and the global climatological records of sea ice extent and location. The plan is to use the most recent snow/ice knowledge within the region being masked. This will be a stored global array which is updated within the VCM by conducting snow/ice tests. Knowledge of snow/ice is also needed beneath the clouds by other cloud EDRs following the VCM.

The sun viewing geometry (including solar and azimuthal angles), and the sensor viewing geometry are required for the VCM. These are used for setting some reflectance threshold tests. The data will be used to look for sun glint effects; set, apply, or adjust thresholds for cloud detection tests; assist in eliminating optically thick aerosol-laden paths (which can be misidentified as clouds); assist in the identification of cloud shadows; and to determine if a pixel is in the day or night regime. The night regime is defined as when the solar zenith angle exceeds 85 degrees.

The geolocated positions on the Earth's surface are needed as input to the VCM. The latitude and longitude coordinates of the surface being viewed allow the land/sea/ecosystem information to be retrieved from the land/water and ecosystem maps.

Surface temperature maps are presently not being used in the VCM, but are considered to be a future input which will increase the probability of correct typing of clouds. The surface temperature map, when available, may be used as ancillary input data to the VCM. A surface temperature map for both land and sea is needed to enhance cloud detection. With the lack of daytime solar radiance measurements, low surface temperatures can be misidentified as clouds in some thermal cloud detection tests. Also, thermal threshold tests, for cloud detection will need to be modified using surface temperature data. The surface temperature map is expected to come from a combination of the CMIS Sea Surface Temperature EDR, CMIS Land Surface Temperature EDR, CRIS Vertical Temperature Profile EDR, VIIRS Ice Surface Temperature EDR, VIIRS Land Surface Temperature EDR, VIIRS Sea Surface Temperature EDR, ground based *in situ* surface temperature measurements, and sea ice based *in situ* measurements from the International Arctic Buoy Program (IABP). These surface maps may be used for establishing thresholds over a region for cloud detection tests. The primary benefit achieved from using surface temperature maps would be for nighttime cloud tests.

As with surface temperature maps, as explained above, the clear sky radiance/reflectance composite maps are presently not being used in the VCM. Clear sky radiance maps will allow cloud detection thresholds to be set and evaluated, and improve cloud detection. These clear-sky composite maps are expected to be composed of clear sky VIIRS radiance measurements, clear sky OMPS radiance measurements, clear sky CRIS radiance measurements, and clear sky CMIS radiance measurements. Dramatic seasonal differences in vegetated surface reflectances may require monthly or seasonal clear sky radiance composite maps at a regional level. In many cases, just using the most recent clear sky radiance map will assist in cloud detection. These radiance composite maps are not required for the cloud mask, but if they are available they may be used.

The VIIRS Daytime Nighttime Band (DNB) Top of Atmosphere (TOA) is not presently used for VIIRS cloud detection. The DNB may be useful for cloud detection at

nighttime when lunar illumination is concurrent. The usefulness of the DNB for this application will be investigated for the final cloud mask product, along with the thresholds for the cloud detection tests associated with it. The DNB is also called the Low Level Light Sensor (LLS).

Imagery channels BT of and TOA reflectances are presently used to improve the detection of subpixel clouds within pixels which the imagery channels nest with other VIIRS channels. The VIIRS imagery resolution bands 'nest' in the radiometric bands as depicted in Figure 2.1.

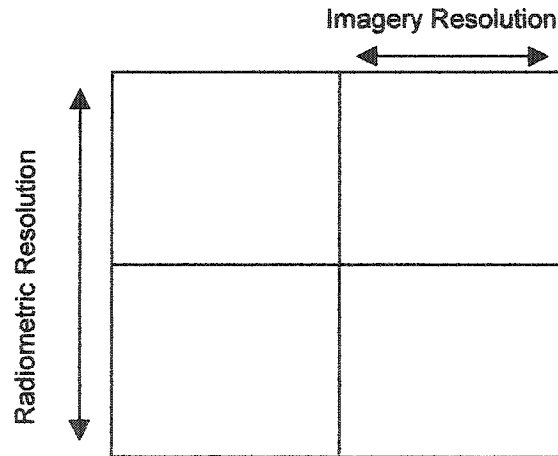


**Figure 2.1:** An illustration of band nesting. Depiction of the nesting of the imagery resolution bands within the VIIRS radiometric resolution bands.

This nesting allows the inclusion of an imagery resolution cloud mask along with the VCM output. The individual imagery resolution pixels, four of which are contained within a given radiometric pixel, undergo cloud detection tests, and the 2x2 imagery pixel region are subjected to spatial contrast tests which are of CLAVR heritage. For the 48 bit output Intermediate Product (IP) the 4 bits are ordered from the upper left imagery resolution quadrant. Looking at the bit numbers 3-6, we note that the first bit is this upper left quadrant, the second bit is the upper right quadrant, the third bit is the lower left quadrant, and the fourth bit is the lower right quadrant.

The use of additional ancillary (non-VIIRS) data sources to be considered for future use has also been investigated, and is detailed in Appendix A.

#### 2.1.4.2 Algorithm Description and Processing

The VCM is developed from a hybrid of the MODIS/CLAVR cloud masks (*Ackerman et al.*, 1997; *Stowe et al.*, 1998). As a hybrid algorithm, it combines the best features from both of these cloud detection algorithms. The overall processing structure of the VCM is directly related to the MODIS Cloud Mask algorithm processing structure, developed by Dr. Steve Ackerman's research team at the University of Wisconsin.

Generation of the VCM occurs routinely as part of the first level of EDR processing, residing in the Sensor Data Record (SDR) module (*Kuin*, 2000). The VCM pixel level results are then used at a pixel level by the other EDRs. The VCM results also undergo a conversion from a pixel level cloud mask to a Horizontal Cell Size (HCS) in the VIIRS Cloud Cover EDR. VCM output is used by the many other EDRs which depend on cloud masking. The VCM does cloud tests at both the radiometric resolution, using the radiometric bands, and at the higher Imagery resolution, using the Imagery bands. The pixel level detection is performed using a limited number of cloud thresholding tests, and spatial homogeneity tests applied to the 2x2 imagery bands. The Imagery tests use thresholding at the imagery resolution. Imagery resolution tests available in CLAVR-1 are used in the VCM. These multi-pixel contrast and thresholding tests are done using the imagery bands nested within radiometric bands. Use of the imagery resolution bands for cloud detection allows for the sub-pixel level clouds to be more easily detected.

A conceptual overview of the VCM algorithm is displayed in Figure 2.2. The data input to the VCM is illustrated in the ellipsoids above the 'black box' in which the VCM is contained. Output from the VCM is illustrated at the bottom of Figure 2.2. The

output data are reported at a pixel level. For the multi-pixel tests, the output data are reported at an aggregated pixel resolution. The VCM box in Figure 2.2 has been expanded in order to assist in explaining how the VCM algorithm processes the data.

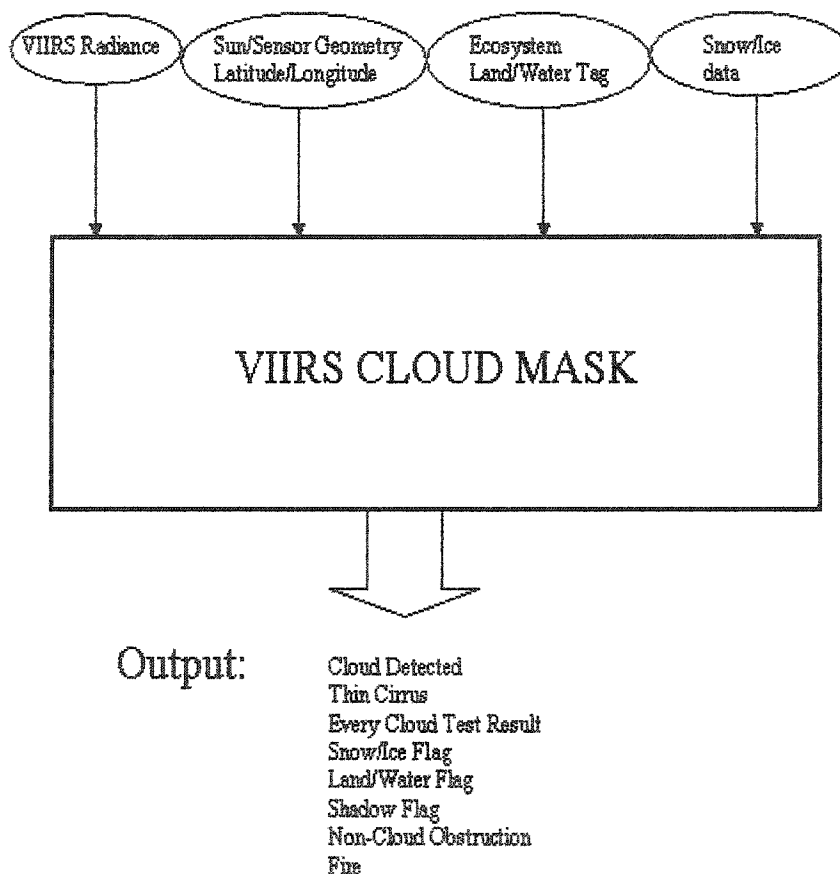


**Figure 2.2:** Conceptual overview of the VCM EDR.

Figures 2.3-2.5 and 2.7 depict the expansion of the VCM depicted in Figure 2.2, and show the general flow of the algorithm. The final box in the flowcharts from Figures 2.3-2.6 continue onto the next figure in sequence.

The first modules (Figure 2.3) of the VCM show the processing steps for the cloud mask. These are performed in a loop over a given scan line of the image being masked. First, the arrays for the algorithm are defined. This sets up the appropriately sized arrays for channel radiances, latitude, longitude, channel BTs, channel reflectances, sun/sensor geometry, ecosystem, and others. Once these arrays have been defined, they are then filled with data read in from ancillary data products, VIIRS radiance data, and sun/sensor data. In order to perform BT thresholding tests, the radiances for the VIIRS thermal channels are assumed to have been converted to Brightness Temperatures (BT) values before the VCM is applied in the SRD Module. These radiances are placed in the appropriate arrays. Due to limited data flow from the sensor to the algorithms, the additional sun/sensor relative azimuthal and reflectance angles are assumed to be calculated prior to the application of the VCM for the given FOV. The background beneath the pixel being masked is then determined and the land/ocean, sun glint, and ecosystem masks are applied. Logical arrays are defined along the entire scan line which define the pixel in terms of its background. This is necessary to define which thresholding tests are to be performed later in the algorithm, as well as to set the appropriate cloud detection threshold values. The BT and reflectance values are then unscaled. Note, however, that this unscaling step may not be necessary if no scaling was done to the radiance before the algorithm began processing. Scaling has often been performed in cloud mask program architectures in the past to decrease the overall data flow rate. The solar radiance channels are then converted to reflectances, and the thermal radiance channels are converted to BTs, if either have not been converted prior to the application of the cloud mask. These reflectances are used in the thresholding cloud detection tests, while the BTs are used in differencing tests which are employed to detect the presence of a cloud.

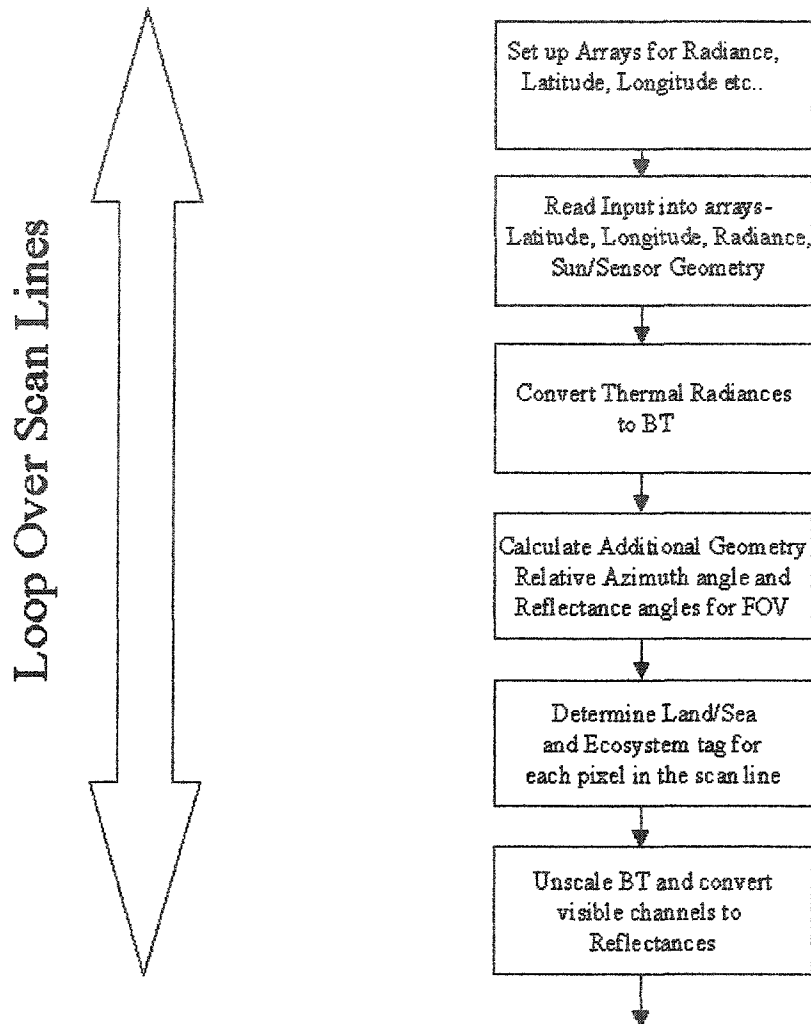


**Figure 2.3:** First section of flowchart of the VCM.

Once a given scan line of an image is prepared, the loop along the scan line is performed. Each scan line is processed within the loop over the scan lines. For an image, a simple way to envision this looping process (Figure 2.4) is the following. If,  $x$  denotes the horizontal position along a scan line and the vertical is  $y$ , there is a loop over  $x$  done within a loop over  $y$ . To facilitate the cloud tests, a context region is first set up. This is an  $N$  by  $N$  region, with  $N$  defined by the user. At present the context region has  $N$  set at the value  $N=1$ , this corresponds to the VIIRS radiometric pixel resolution. In the future, if cloud contrast tests are performed upon the bands for mask output at a

coarser resolution, the context region considered might be increased in size. An array is then filled with the radiometric band BT, reflectance, and radiance values for the pixels within the N by N region. This N by N region is set up in order to be slid along a given scan line. The central pixel will be subject to pixel level tests. Also, in future algorithms, the larger region surrounding the center pixel will have the capability to have contrast and statistical tests performed upon it. Contrast and threshold tests will also be performed upon the five 2x2 imagery and DNB/LLLS channels which nest within the VIIRS radiometric resolution pixels; tests under consideration are CLAVR in heritage. In the MCM (*Ackerman et al.*, 1997), it has proven necessary to perform an averaging of the thermal channels over the entire context region, in order to minimize the thermal noise. Presently, this is not being done for the BT threshold tests. In the future, this averaging may be performed if it demonstrates an improvement in cloud masking. The cloud mask array results are then cleared prior to cloud masking. The ancillary data logic flags are subsequently set for the pixel region being masked. This means that the region is defined as being within the following categories: land/water, in a possible sun glint geometry, day/night, or in a polar region. This is a crucial step. The definition of the region will control the dataflow of the algorithm, and determine which cloud masking tests are performed and which thresholds applied. In sun glint regions there will still be a cloud mask generated. This cloud mask, however, will only employ the thermal cloud detection tests which are unaffected by sun glint. The region is then tested for snow/ice using Normalized Differential Ice Index (NDII) tests developed by D. Hall (*Hall et al.*, 1995).



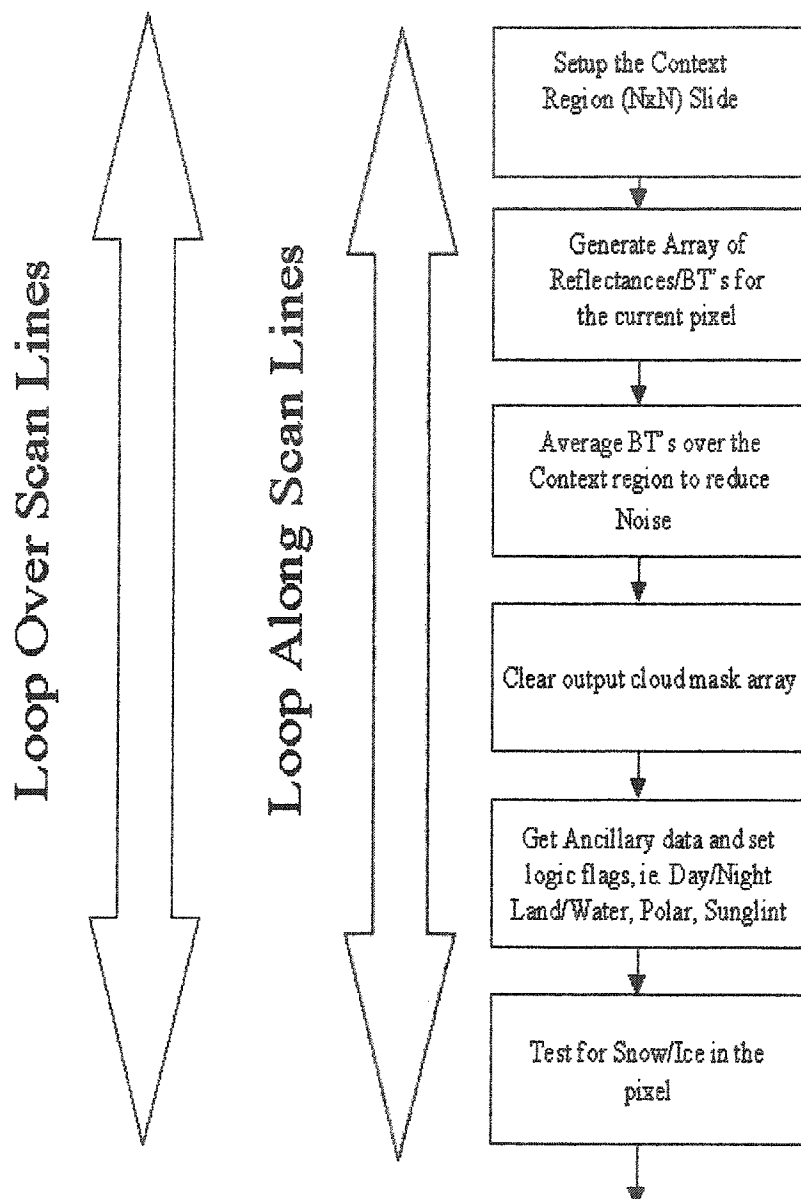


**Figure 2.4:** Second section of the flowchart of the VCM.

The crucial masking occurs in the first box depicted in Figure 2.5. This box is expanded in Figure 2.8 and explained in more detail later in this processing description. Along with the cloud detection (performed on a radiometric pixel level and at the imagery resolution), the specific cloud test which flagged the cloudy pixel will be reported. By reporting the cloud

test which was successful, the capabilities of specific cloud tests can be better assessed and the detection thresholds adjusted appropriately. The presence of high versus low level clouds, classification of cloud thermodynamic phase, and automated cloud typing are also performed. Another capability of this cloud mask is the use of a confidence code upon each pixel. This confidence technique is presently employed by the MODIS Cloud Mask (MCM) (*Ackerman et al., 1997*). The setting of an absolute threshold to distinguish between completely cloudy and clear is quite abrupt in some cases. A range of values between the definite confident clear and definite confident cloudy is established to identify the confidence level to be assigned to a pixel. From experience with the MCM, the author notes these regions are commonly the cloud edge regions. Assessment of confidence of the cloudy vs. clear will assist other EDR algorithms, which depend on the VCM to judge the quality of the cloud-flagged pixels. A similar series of confidence levels are also established for the cloud phase determination.

The confidence flag methodology applied to establish four levels of cloud confidence is similar to that used in the MCM (*Ackerman et al., 1997*). The reasoning behind using these confidence levels is that as one approaches the threshold limits, the certainty or confidence in the labeling of a pixel as being cloudy or not cloudy becomes uncertain. As such, an individual confidence flag is assigned to each single pixel test, and the value of this confidence is a function of how close the observation is to the thresholds. All of the individual confidence flags are combined to produce the final cloud mask radiometric resolution EDR flag. The four confidence levels are designed to provide information about how much confidence a user of the cloud mask can place in the result. Each test is given a value between 0 and 1, representing increasing confidence that the pixel has clear sky conditions. Figure 2.6 is a graphical representation of how a confidence level is assigned for a given spectral test. This technique is commonly called the S function approach, named after the shape of the curve in Figure 2.6 (*Ackerman et al., 1997*). The abscissa represents the observations and the ordinate the confidence of clear sky conditions. In this figure the observation with a value greater than  $\gamma$  is high confidence clear, while an observation with a value

less than  $\alpha$  is cloudy. Likewise a value between  $\alpha$  and  $\beta$  indicates probably cloudy confidence, whereas a value between  $\beta$  and  $\gamma$  indicates probably clear confidence. These high confidence clear and cloud thresholds,  $\gamma$  and  $\alpha$  respectively, are determined from observations and/or theoretical simulations. The MODIS cloud mask team has found that the S function may be applied to assign confidence, and the VCM team has adopted a similar approach. In the final cloud mask only four levels of confidence are provided, these confidence levels are based upon how close the observed value is to a set of thresholds. These individual confidence levels are combined to determine a final decision of cloudy or clear, with the probably cloudy and confident cloudy indicating the binary EDR cloudy result, and the probably clear and confident clear indicating the binary EDR not cloudy result. The way in which the bits are arranged in the VCM and also the modularized coding of the VCM will allow the use of a full MODIS cloud confidence determination if this approach is proven to be a beneficial methodology. The imagery resolution 2x2 nested in each radiometric pixel is analyzed as follows: if only one of the four pixels indicates a cloud then the results are probably cloudy; if two or more indicate cloud presence then the pixel is confident cloudy; and if none indicate cloud presence then it is confident clear.

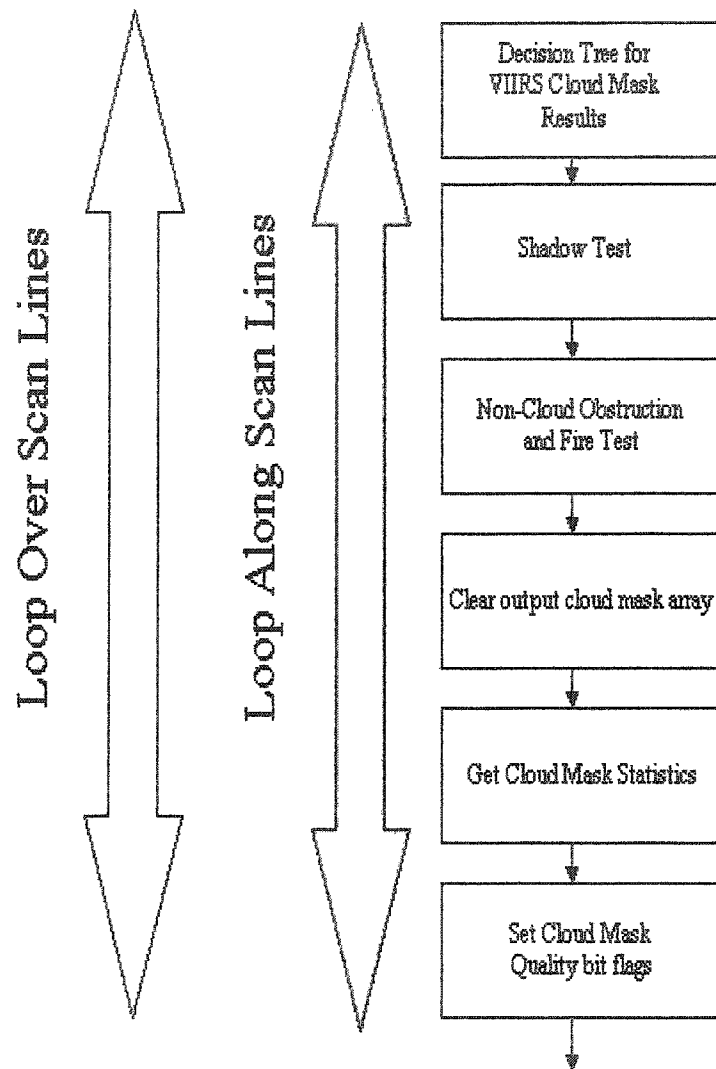
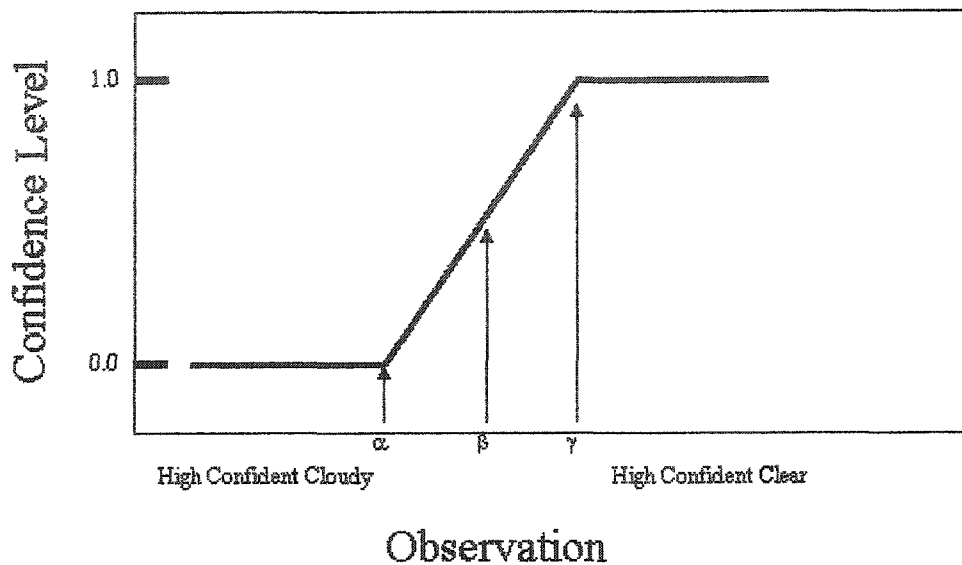


Figure 2.5: Third section of the flowchart of the VCM.



**Figure 2.6:** Graphical depiction of confidence thresholds.

Once a cloud mask result has been returned for the context region or individual pixel, several additional tests are then performed, including a shadow test. This test determines if there are shadows within the regions where clouds were not detected. Detection of cloud on cloud shadows and cloud shadow on snow/ice is an issue for further research. These detections are not presently being considered. The next test performed over the pixel region is a non-cloud obstruction test. The cloud mask statistics from the context region are then set into the proper arrays. The cloud mask flags are also set, along with quality flags for use by other EDRs in assessing the cloud mask performance. When this has been done, the loop along the scan line is complete. The loop over the scan lines is continued with the next scan line. This loop will be continued until all scan lines of the image have been masked.

The final step in the loop over scan lines is depicted in Figure 2.7. For each scan line the output of the cloud mask is written as a stream of 48 bits for each pixel within the region. The output also includes quality flags indicating the performance and

confidence of the cloud mask, and the imagery resolution cloud mask results. This Cloud Mask IP will be explained and is depicted in Table 2.5.

Data are then rebuffered for the next scan line, thus freeing up arrays with appropriate indexing. The loop over the scan lines is then resumed until all scan lines in the image have been masked. At this point, the statistics of the cloud mask image as a whole are produced. This step is performed for the inspection by the analyst. These image statistics may be used by the cloud cover EDR or imagery EDRs in the future. If not, that step can be removed from the final algorithm structure.

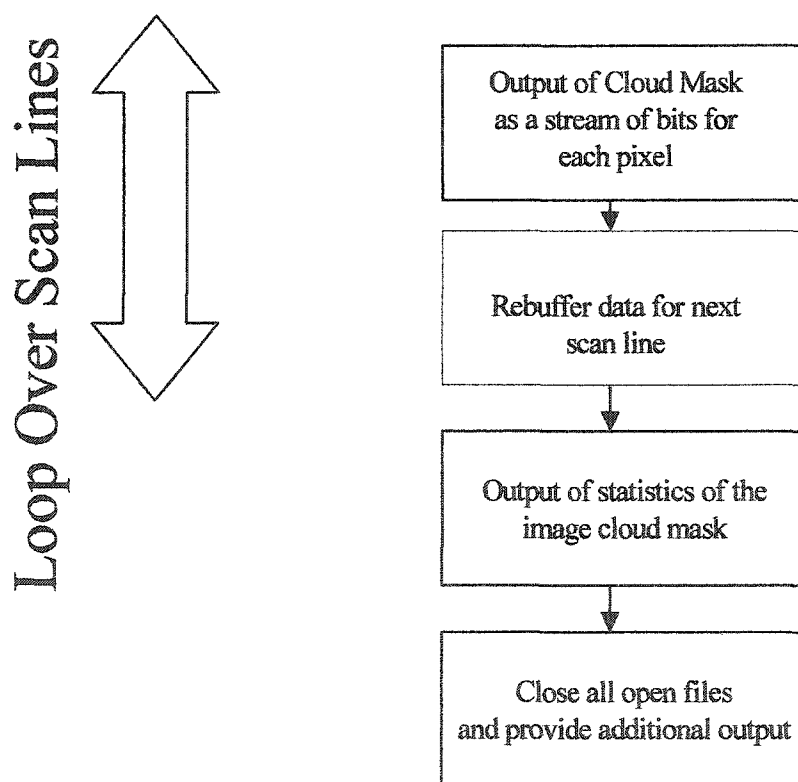


**Figure 2.7:** The final section of the flowchart of the VCM.

Figure 2.8 illustrates the flow of the VCM within the first module of Figure 2.5. For a given pixel, the knowledge of the underlying surface type determines which specific cloud tests are performed. The flow of the algorithm determines the cloud tests

and threshold settings for the pixel, based upon the underlying surface type. The underlying surfaces are designated as polar, land, ocean, desert, and coastal. The tests performed for these specific regions will be discussed in Section 2.3. As the algorithm develops, additional surface type modules may be added, based on whether more specific threshold differences are found to improve cloud detection.

## DECISION TREE FOR VIIRS CLOUD TESTS

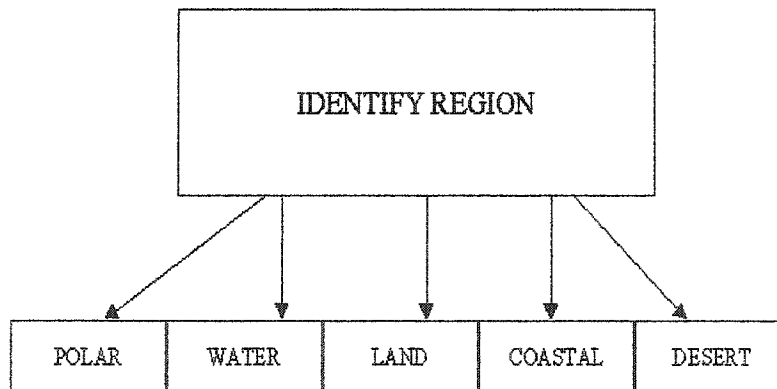


**Figure 2.8:** Conceptual overview of the pixel region classification by the VCM.

For a more detailed description of the Cloud Mask software architecture structure there is further development and explanation provided in Appendix B.

### 2.1.4.3 Cloud Mask Output

The Cloud mask output is summarized in Figure 2.6. Output from the VCM is 6 bytes (48 bits) for each radiometric resolution pixel, this is called an Intermediate Product (IP). This output is a binary result (1's and 0's) for each pixel.

**Table 2.5:** The 48 bit Intermediate Product (IP) output of the VCM.

Byte	Flag	Bit #	Note (bit results indicate)
1	Cloud Mask Quality Flag	1	1= mask okay/0=mask questionable
	Binary Cloud EDR result	2	1= cloudy/0=not cloudy
	Cloud Imagery Resolution Flag	3-6	1=cloudy/0=not cloudy (each bit is a pixel of the 2x2 imagery resolution pixels nested in the radiometric resolution pixel), 1111 = all cloudy, 0000=all not cloudy
	Cloud Confidence Flag	7-8	4 confidence levels of cloud EDR flag, 11= confident cloudy, 10=probably cloudy, 01= probably clear, 00=confident clear
2	Sun Glint Flag	9-10	11= geometry based sunglint, 10= wind speed based sunglint, 00= no glint (1 spare flag 01)
	Snow Surface	11	1=snow/ice, 0=no snow/ice
	Surface Type	12-14	111=land, 000=water, 010=coastal, 011=desert other 5 flags (101,110,100,001,010) reserved for additional surface types used in future
	Non-Cloud Obstruction	15	1=yes, 0=no
	Thin Cirrus Detected (Daytime)	16	1=yes, 0=no
3	Cloud Phase	17-18	11=water, 00=ice, 10=mixed, 01= unknown
	Pixel Within 2 of a cloudy pixel	19	1=yes, 0=no (radiometric pixel size considered)
	Shadow Flag	20	1=yes, 0=no
	High Cloud Flag	21	1=yes, 0=no
	Low Cloud Flag	22	1=yes, 0=no
	Fire Detected	23	1=yes, 0=no
	Day/Night	24	1=day, 0=night
4	Cloud Test Flags	25-32	4 cloud test results indicators 1=tested/0=not tested and 1=cloud detected/0=no cloud detected. Each cloud test done has a 2 bit flag which tells if a pixel was tested and if it passed or failed.
5		33-40	4 cloud test results indicators (see Byte 4)
6		41-44	2 cloud test results indicators (See Byte 4)
		46-48	spare bits (2 more cloud tests allowed in future)

The exact number of bytes for each pixel of output is presently 6, but may be increased as needed. This depends on the number of cloud tests performed in the final product, and the demands placed upon the cloud mask by other VIIRS EDRs.



The Cloud Cover EDR is an aggregation over a multiple pixel region of the cloud mask cloudy/not cloudy results. Summing these results over a given area and dividing by the total number of pixels within that area result in the fractional cloud cover. The Horizontal Cell Size (HCS) at which this will be done is still being considered. The cloud mask will deliver the cloudy/not cloudy decision at the radiometric and imagery pixel levels. The Cloud Cover/Layers EDR is covered in depth in the VIIRS Cloud Cover/Layers (*Apling et al., 2000*).

## **2.2 Description and Physics of Cloud Masking**

In the following section, the background of the processes previously outlined will be described. These processes apply only to regions which successfully passed the quality examinations.

The detection of clouds using simple visible reflectance and thermal BT thresholding tests has been demonstrated with considerable success. Due to their nature, clouds are generally characterized by a higher reflectance and lower temperature than the underlying surface. This statement is generally true for most surface types around the Earth, such as ocean and sea level vegetated land. However, some surfaces require adjustments to the thresholds needed to detect clouds, and the use of different cloud detection tests. The various cloud detection tests and techniques will be discussed in the section below.

### **2.2.1 Pixel Level Cloud Detection Tests**

The basis of the VCM is the pixel level cloud detection tests. These are performed over an entire image. The pixel level tests define if a pixel is clear or cloudy. This will be done at the radiometric resolution using the radiometric channels, and at the higher imagery resolution using the imagery bands. Table 2.6 displays the current

threshold values for the various cloud tests presently being performed within the VCM; note however the threshold values illustrated are for MAS channels, not VIIRS. As a result these threshold values are subject to change in the future, however the changes are not expected to be large. The number of tests and scenarios will also increase with the development of the VCM. In the following section the various cloud tests currently employed are discussed, along with those which will be researched/considered in the future. Many of the tests presented here are performed by the MCM and CLAVR. Thresholds for the tests will be developed in the future using MODIS data sets. These thresholds, depicted below in Table 2.6, were developed from representative MAS spectral data.

In the future, contrast tests will be developed using the 2x2 imagery pixels which nest within the radiometric pixels to define clear and cloudy regions. These high-resolution tests will use imagery resolution channels, which are nested within and at a finer physical resolution than the VIIRS bands. Many of the techniques presently used by CLAVR will be used in contrast tests applied to the imagery pixels for cloud detection.

Bi-spectral cloud detection tests are computationally inexpensive. However, it is important that pixels are only detected as cloud a single time; therefore, the most efficient cloud detection test is applied first to all pixels. Those pixels classified as cloud-contaminated are removed, flagged, and the second cloud test is applied only to those remaining cloud-free, and so forth. Adjustments for special effects, e.g., partially cloudy pixels and shadows, are made only after all cloud tests have been applied and pixels identified as cloud-contaminated have been flagged.

Table 2.6: VCM tests performed with MAS thresholds.

Test	Day Ocean	Night Ocean	Day Land	Night Land	Day Snow	Night Snow	Day Desert	Night Desert
BT11 IR Threshold	<270K	<270K						
R1.38 High Cirrus	>2.5%		>3.5 %		>3.5 %		>3.5%	
BT3.7– BT12 Thin Cirrus		0.6 K	-16K	>4 K		>4 K		Used
BT11– BT3.7 Low water clouds	<- 8 K	>0.6 K	<-16 K	>0.6 K	>9 K	>0.6 K		Used
R0.66 Visible reflectance			>27 %					
R0.87 Visible reflectance	>7%						>30 %	
R0.87/R0.6 6 Visible ratio	0.9– 1.1		0.9- 1.1					
BT3.7 – BT4.05	>6K		>10 K		>8K			
R1.6 Near-IR reflectance	>25%		>50 %		>35%		>60%	
BT8.6– BT11 & BT11–BT12 Tri-spectral test	Table or <0.2 K	Table or <0.2 K	Table or >3 K	Table				Table

### 2.2.1.1 Thermal BT Tests

The BT11 threshold test is a simple Infra-Red (IR) window threshold test. This test is performed over open water. The test should be cautiously used in other regions, due to the effects of cold snow/ice surfaces on this channel, and the emissivities of some land types. Over open ocean, when the BT of the 11  $\mu\text{m}$  channel is less than 270 K, the pixel is designated as cloudy. This test is only applied over open water at present.

A test that has proven successful for the detection of thin cirrus clouds under primarily night time conditions is the BT3.7-BT12 micron test. Applying this BT difference test is useful for separating thin cirrus and cloud free conditions (*Hutchison and Hardy, 1995*).

The BT11-BT3.7 differencing test became best known for the detection of stratus in nighttime imagery (*Saunders and Kriebel, 1988*); however, this BT difference test is also useful for detecting clouds during both day and night. The differences present in a cloudy scene are a result of the different emissivities between the 3.7 and 11  $\mu\text{m}$  channels, and the presence of a solar component in the 3.7  $\mu\text{m}$  channel. Thermal difference tests will be performed with caution in the polar regions, where cold surface temperatures may give false cloud detection.

Scatter plots of the BT8.6-BT11 and BT11-BT12 differences has been useful in detecting clouds as demonstrated by researchers at the University of Wisconsin. The spectral uniformity of surface emittance in these IR window regions can be used to detect clouds. For a complete explanation of the technique see *Ackerman et al. (1990)* and *Strabala et al. (1994)*.

The BT3.7-BT4.05 difference test is another method of removing the solar and thermal contribution of the 3.7  $\mu\text{m}$  channel. Due to the small wavelength differences between these two bands the thermal contributions are relatively close. The largest difference between these two bands is due to the larger solar component in the 3.7  $\mu\text{m}$

channel. The BT3.7-BT4.05 difference removes the BT component and thus isolates the difference due to the larger solar component in the 3.7  $\mu\text{m}$  channel. Due to the low reflectances of most surface types, and the relative high reflectance of clouds in the 3.7  $\mu\text{m}$  channel, this test has shown much promise in MAS and simulated VIIRS data. This test works only during daytime conditions, but over a majority of surface types.

### 2.2.1.2 Visible to MWIR Reflectance Tests

A single channel reflectance test for bright clouds over dark surfaces may be applied using the 0.65  $\mu\text{m}$  channel. This test may not be used over bright snow/ice covered surfaces, but has success over heavily vegetated areas and some success over open ocean regions.

A single channel reflectance test for bright clouds over dark surfaces may be applied using the 0.86  $\mu\text{m}$  channel. This test may not be successful over vegetated regions, but has demonstrated some success over snow/ice and desert regions. The primary use for this test is for cloud detection over water surfaces.

The  $R_{0.86}/R_{0.65}$  reflectance ratio test is based upon the fact that the reflectances for cloud covered regions in these bands should be very close to one another (*Saunders and Kriebel, 1988*). For cloudy pixels, this ratio is slightly less than one, but may be as small as 0.6 depending upon solar illumination and scattering geometry. But over clear vegetated land scenes this ratio is generally greater than one, and for clear water surfaces this ratio is much less than one, depending upon solar illumination and scattering geometry (*Hutchison and Hardy, 1995*).

A single channel 1.38  $\mu\text{m}$  reflectance test may be performed for high cirrus cloud detection (*Gao et al., 1993; Gao et al., 1998*). This single channel reflectance test greatly improves the detection of thin cirrus over land surfaces in daytime imagery, if sufficient lower-level water vapor is present (*Hutchison and Choe, 1996*) and can be used to decouple high cirrus clouds from lower level clouds for the analysis of cloud top

phase (*Hutchison et al.*, 1997). The high amount of water vapor absorption across this channel means radiation reflected from the surface and lower level cloud is absorbed by water vapor. The resulting reflectance/absorption signature is indicative of a thin cirrus cloud presence. This test may require modifications to the thresholds, if it is to be applied in polar regions with low water vapor levels.

The reflectance threshold test at 1.6  $\mu\text{m}$  uses the high absorption of snow/ice surfaces, and the highly variable reflectance of clouds within this band to differentiate between water clouds and these cloud-free surfaces. The dramatic variation in snow/ice versus cloud absorption was first detected by Russian scientists (*Valvokin*, 1978). Use of this reflectance test has demonstrated promising capabilities for cloud detection over snow and sea ice, and cloud vs. snow/ice discrimination.

### 2.2.1.3 Imagery Band Tests

The imagery bands on the VIIRS sensor are at a finer resolution than the other VIIRS radiometric bands, within which they nest. Presently these bands are centered at 0.65, 0.86, 1.6, 3.7, and 11.45  $\mu\text{m}$ , having a Horizontal Cell Size (HCS) of approximately 370 m. Cloud tests performed with these bands will rely on spectral contrasts as well as tests being conducted at the finest spatial resolution available, and will be reported at the imagery resolution. These tests are BT and reflectance tests of CLAVR heritage.

The imagery BT11 threshold test is the same as the radiometric test, except that it relies on the imagery resolution band centered at 11.45  $\mu\text{m}$ . Thus, the BT11-BT3.7 difference test is the same conceptually as the test used at the radiometric resolution with the radiometric bands, but it is performed at the imagery resolution with the imagery bands centered at 3.7 and 11.45  $\mu\text{m}$ .

The reflectance 0.66  $\mu\text{m}$  threshold test is the same as the test used for the radiometric resolution test, but relies on the imagery resolution band centered at 0.645

$\mu\text{m}$ . The reflectance threshold test at  $0.86 \mu\text{m}$  is the same as the test used for the radiometric resolution test, but uses the imagery resolution band centered at  $0.845 \mu\text{m}$ . The reflectance ratio test of the  $R_{0.86}/R_{0.65}$  is the same as the test used for the radiometric resolution test, but uses the imagery resolution bands centered at  $0.645$  and  $0.845 \mu\text{m}$ . Finally, the  $1.6 \mu\text{m}$  reflectance ratio test is the same as the test used for the radiometric resolution test, but uses the imagery resolution band centered at  $1.6 \mu\text{m}$ .

#### 2.2.1.4 Tests For Future Investigation

Use of the BT $_{8.6}$ -BT $_{3.7}$   $\mu\text{m}$  brightness temperature difference test should be considered for further investigation. This would be a radiometric resolution pixel threshold based test. It has shown promise in detection of clouds over snow and ice covered surfaces, and it is under investigation.

A BT $_{3.7}$  thermal and solar component separation test is proposed for future investigation. By decoupling the solar and thermal component of the  $3.7 \mu\text{m}$  channel, it has been demonstrated that the contrast between a snow-covered surface and thin cirrus is greatly enhanced using only the reflective characteristics, along with the Advanced Very High Resolution Radiometer (AVHRR)  $0.6 \mu\text{m}$  band (*Hutchison et al.*, 1997; *Hutchison and Locke*, 1997). Also, there is similar behavior of the imaginary component of the indices of refraction of ice and liquid water between this channel and the  $1.6 \mu\text{m}$  channel. For this reason, the solar components reflectivity may be used to perform similar reflectance tests as those which are planned with the  $1.6 \mu\text{m}$  channel as explained above.

Use of the VIIRS Day time Nighttime Band (DNB) as a reflectance threshold test would be useful for non-polar region cloud detection at night when lunar illumination is present. Use of this DNB may also be useful over urban regions where clouds should obscure city lights. An imagery resolution cloud detection threshold needs to be developed using the DNB reflectance. The methodology for this would be the same

applied over the other imagery resolution bands. Also contrast tests may be developed with this DNB using the 2x2 DNB pixels nested within any radiometric pixel.

The VIIRS Imagery resolution pixels may be used for contrast using the 2x2 DNB pixels nested within any radiometric pixel. These tests would be CLAVR in heritage and should assist greatly in sub-radiometric resolution pixel cloud detection. All the tests proposed above for imagery band cloud detection may be used in spatial inhomogeneity tests which are CLAVR in heritage (*Stowe et al.*, 1998).

#### 2.2.1.5 Additional Pixel Level Tests

A non-cloud obstruction test has proven useful by the MCM (*King et al.*, 1998). Detection of non-cloud aerosols are important for the cloud mask, for those sun/sensor geometries which create long path-lengths. For long path-lengths, aerosol-laden atmospheres may be misinterpreted as clouds by some tests. This is due to the enhanced reflectances in the visible bands created by the non-cloud obstructions. This test is present primarily for the Imagery Analyst (IA) to assess the presence of aerosols by use of an automated indicator. To detect aerosols in the path, simple pixel level tests are planned. A quality flag indicating the performance will be output from the cloud mask. Presently, the plan is to use tests involving the 11 and 12  $\mu\text{m}$  VIIRS channels to detect the presence of dust storms. Similar tests will identify heavy aerosol using the 2.1 and the 0.65  $\mu\text{m}$  bands. In addition, a simple fire detection test will be employed using the 3.7 and 11  $\mu\text{m}$  channels.

Detection of cloud shadows is a problem which has not been addressed adequately in the literature. Some approaches perform a theoretical computation of shadows from viewing geometry, solar azimuth and zenith angles, cloud edge distribution, and cloud top altitudes. But these approaches require far too much computation time to run operationally. The current VCM cloud shadow detection approach is the MODIS shadow detection approach (*King et al.*, 1998). This method of



shadow detection only works over vegetated regions. Cloud-on-cloud shadows are not detected by this algorithm. Topographical shadowing is another form of shadowing which exists. Topographical shadowing will not be detected by the VCM. In the future, when Digital Elevation Models (DEMs) evolve to include parameters to investigate such effects, topographical shadowing detection may be considered for VIIRS.

A multiple cloud flag is indicated when a test result which is indicative of a high and a low cloud is triggered. The reason for these flags is that they may be used by the cloud cover/layers EDR to indicate a multi-layered cloud and also by the cloud EDRs which follow in the processing architecture. These flags also can aid in cloud phase assessment.

Detection of single versus multi-layered clouds is done once all of the cloud mask tests have been performed on a pixel. By looking at the cloud tests results one can infer the presence of a possible multi-layered clouds presence. This is due to some cloud tests detecting the presence of high clouds only, while others are sensitive to the presence of low clouds. The results of this test are useful to an analyst and will benefit the Cloud Cover Imagery EDR.

Sun glint pixels possess glitter contamination. Consequently, the pixels in which possible sun glint is occurring need to be identified. Solar channel threshold values need to be adjusted for these pixels. Sun glint will not prevent a cloud mask from being generated. In the case of sun glint the solar tests performance may be inhibited, but the thermal channel tests will still be done to generate the equivalent of a nighttime cloud mask. Knowledge of sea surface winds may be included in the sun glint test; surface winds can narrow the region in which sun glint may occur. There is a justifiable concern that cloud detection will not be as reliable in glitter-contaminated regions. A classification as clear is probably correct, but a classification as cloudy may actually be due to the glitter effect as opposed to a cloud. Sun glint will be considered over both land and water areas. Land regions are included because spatially unresolved water bodies, snow, or recent rainfall can also cause sun glint.

Sun glint may occur when the reflected sun angle  $\theta_r$ , is  $0^\circ$  to  $36^\circ$ , where:

$$\cos\theta_r = \sin\theta\sin\theta_o\cos\phi + \cos\theta\cos\theta_o \quad (2.1)$$

where  $\theta_o$  is the solar zenith angle,  $\theta$  is the viewing zenith angle, and  $\phi$  is the azimuthal angle (*Ackerman et al.*, 1997).

Sun glint is also a function of the oceans surface state, which is affected by sea surface winds. Two sunglint products are generated; one considering the geometric region mentioned above in Eq. (2.1) and another taking into account input wind fields; this output will be used by the ocean and aerosol EDRs to identify sunglint regions.

The VIIRS Cloud Phase (VCP) algorithm determines if a pixel, which has been classified as cloudy by the VCM, contains a cloud which is composed of predominantly liquid water or ice. This processing is done in the VCM algorithm. A detailed description of the VCP algorithm is included in the Appendix C of this thesis.

### 2.3 Cloud Mask Over Varying Surface Types

Cloud masking over varying surface types requires the use of different thresholds to be applied over the different surfaces. The pixels are classified within a specific region based upon their geolocation, day/night, land/water, and other categories. The pixel level thresholds being applied over the regions presently considered are shown in Table 2.6. As the VCM evolves, additional regions may be added to improve the results of the cloud mask. New thresholds for specific regions will be developed.

A conceptual flow of the cloud mask algorithm performed over land surfaces is illustrated in Figure 2.9. After a pixel has been identified to be within a land region, it is first classified as day or night. For the purposes of the cloud mask, “day” is defined as when the solar zenith angle of the pixel is less than 85 degrees. Larger solar zenith angles are considered as “night”. After designation of day land or night land, the

snow/ice detection is applied. Presently, the land type is only subdivided into vegetated land and desert ecosystems. In the future, it is expected that the number of different ecosystems considered will increase. Table 2.6 displays the cloud tests which are performed over the vegetated land surface type and the thresholds presently being applied.

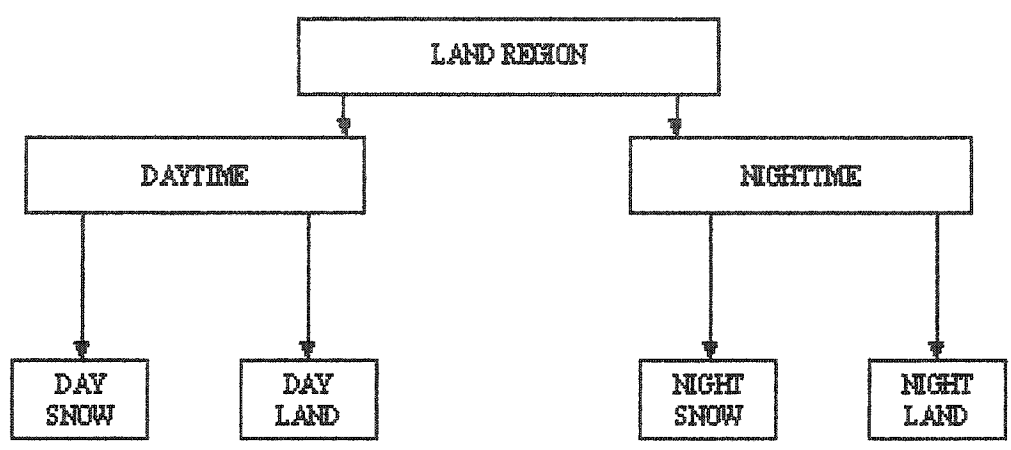


**Figure 2.9:** Conceptual flow of the VCM over land regions.

Pixels in regions between the land and open ocean are classified as coastal regions. As was described previously, the classification is subdivided into day and night. Then the scene is further classified into either day snow, day coastal, night snow, or night coastal. The coastal region is designated as a separate subregion due to cloud classification problems which are likely to occur over coastal areas. Within coastal regions, the confidence of the cloud mask will be assumed to be lower than for other regions. Presently the coastal region thresholds have not been developed for the VCM. In the future the MCM approach will be reviewed to determine if the MCM thresholds can be used in the VCM.

Pixels which are designated as water follow the conceptual flow shown in Figure 2.10. The water surface region is subdivided into day and night cases, and then further

subdivided into snow/ice covered surfaces. Water surface reflectances are low across the Visible Near-Infrared (VNIR) spectral regions. The reflectance is uniformly low across the spectrum. As a result of this low reflectance for a water surface, the detection of highly reflective clouds is expected to be very successful. Another beneficial property of water surfaces is that the temperature of water must be greater than 270 K. This allows BT tests to also be more successful. The thresholds for cloud detection over water are shown in Table 2.6.

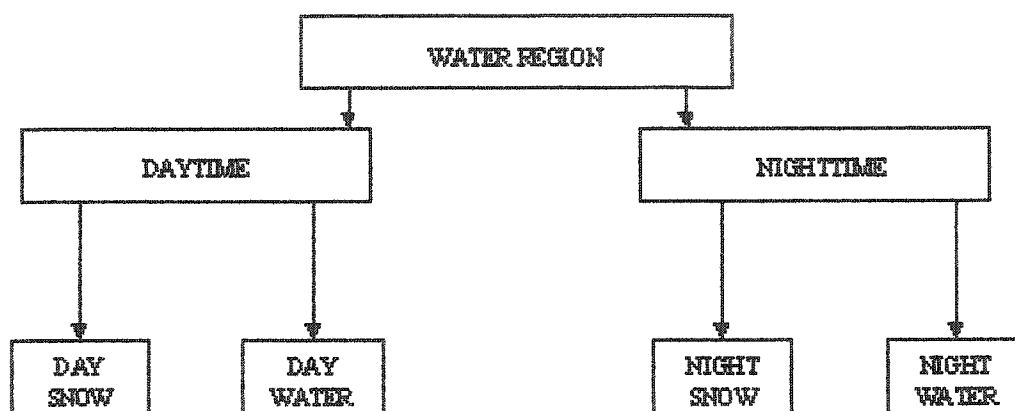


**Figure 2.10:** Conceptual flow of the VCM over water regions.

Regions which are located north of 36 degrees latitude in the Northern hemisphere, or south of 50 degrees latitude in the Southern hemisphere, are designated as polar regions. The reason for the lower latitude, 36 degrees, in the northern hemisphere is to cover the Great Lakes Region. For pixels in the polar region a conceptual flow is shown in Figure 2.11. The latitudinal extent of the polar regions is defined based on the historical range that sea ice is found in the ocean, or where ice covers land. The complexity of the classifications for polar regions is displayed in the conceptual flow diagram. Another aspect of the polar regions is the decreased amount of atmospheric water vapor present, relative to other regions of the Earth. This will require

modified thresholds to be applied to the R1.38 tests, which are sensitive to the amount of atmospheric water vapor.

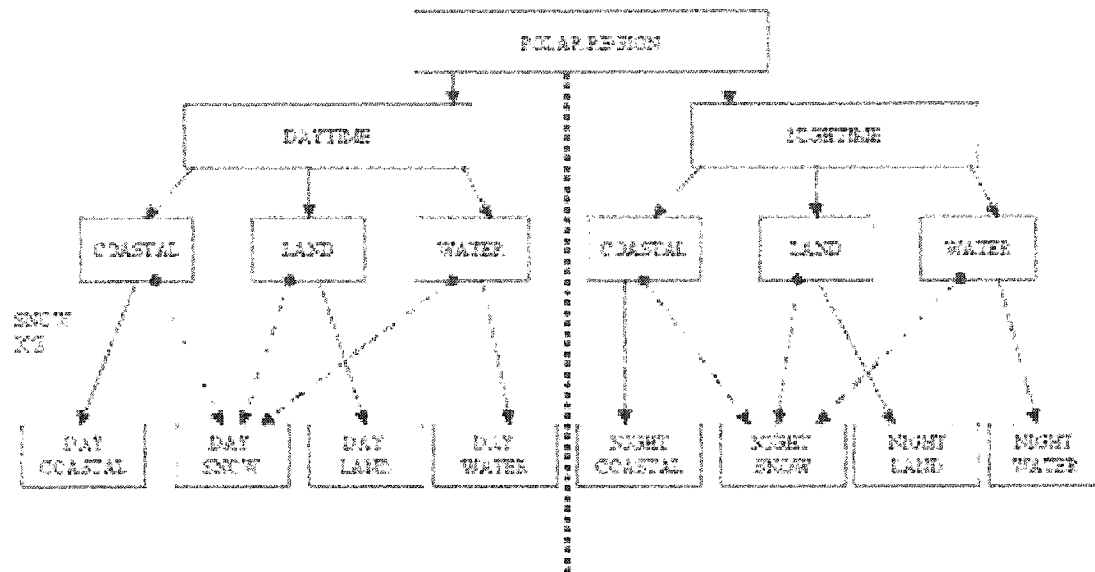


**Figure 2.11:** Conceptual flow of the VCM over polar regions.

Cloud detection over snow/ice covered regions is the most difficult. Each of these surfaces has a high reflectance in the visible combined with a low surface temperature. These traits lead to common confusion/misclassification in the presence of clouds, so cloud detection can be difficult. The confidence of cloud detection in such regions will be low. The thresholds applied across snow/ice covered regions are shown in Table 2.6. As is apparent from this table, the number of tests done in the case of a snow/ice covered region is quite limited. This is a direct result of the reflectance and temperature traits of snow and ice.

## 2.4 Error Budget and Flowdown Results

Based on error budget and stratification studies, detailed in Appendix D, key error sources for the VCM were identified and discussed. These studies provided a guide to instrument and algorithm developers to areas where improvements will have the greatest impact. Ultimately good error budgets lead to tighter specifications when margin can be tightened due to risk reduction based on reliable error estimation. The design process used was a spiral process in which the specifications and performance of the sensor and algorithm design were improved iteratively. After the initial flowdown activity the algorithm data definitions provided requirements from each EDR to the sensor. The most stressing of these requirements became the first iteration for the sensor model.

The errors are assumed to be independent so that the total error is the square root of the sum of the squared errors, also called the Root Sums Squared (RSS). This assumption is made for both precision and accuracy. An exception are the error budgets based on probabilities. In those cases the total probability is either the product of its factors (for typing probability), or, for misclassification, the product of all misclassification probabilities.

There are three categories of error sources. These error sources being sensor, ancillary and auxilliary data, and intrinsic algorithm error sources. The sensor error components are the sensor noise, which is determined by the noise components of the baseline sensor model and Modulation Transfer Function (MTF) model. A band-to-band mis-registration study has been performed in which the radiance of all bands used by the VCM were mis-registered horizontally and vertically. This study shows that gross errors in the VCM occur when band-to-band mis-registration exceeds 20%. This study is

detailed in chapter 3. A discussion of the error budget and flowdown process employed is contained in the Appendix D of this thesis.

#### 2.4.1 Sensor Noise Flowdown

Thus far, cloud detection does not appear to be a major VIIRS sensor driver, for sensor noise. The sensor noise flowdown is detailed in Appendix E. For sensor noise flowdown cirrus cases were analyzed. Cirrus cloud cases are considered to be the most challenging cases for cloud detection, stressing the cloud detection capabilities of algorithms under development. The sensor noise flowdown employed scenarios used in the radiative transfer cloud scene generation, and modeling assumptions and approximations made within the testbed environment.

#### 2.4.2 Cloud Cover Flowdown Analysis

The VCM algorithm has been employed to determine the cloud cover for several cloud scenarios, outlined in Appendix E, in which representative results of that flowdown analysis for a cirrus cloud case is considered.

The SNR tests addressed in Appendix E consider the impact of SNR on both pixel-level retrievals and retrievals when the pixel-level retrievals are aggregated (averaged) to VIIRS SRD horizontal cell size (HCS). The required HCS is a function of EDR parameter; threshold and objective values are stated. For the study aggregations are done at the cloud cover HCS threshold (25 km) and HCS objective (5 km). The VCM test results are presented separately for the daytime and nighttime cases.

Analyses done show for the 25 km threshold HCS during day and night the cloud cover's objective precision and accuracy is attainable for the thin cirrus case over land at nadir out to sensor noise model five, defined in *Kealy (2000)*. Flowdown also indicates that

for the 2 km HCS cloud cover the daytime cases are good out to noise model five, exceeding objective for the accuracy and attaining objective for the precision. However, for the nighttime case the cloud cover does not meet threshold. When the cloud detection thresholds are more precisely set in the developmental stage of the VCM, the accuracy of the cloud cover retrieval will be between threshold and objective.

## **2.5 Cloud Mask Validation**

The VCM algorithm validation has been based on the comparison of cloud radiances computed using radiative transfer codes for the true cloud scenes and real cloud radiances from MODIS Airborne Simulator (MAS) cloud scenes. The synthetic cloud imagery generation process and validation of the cases simulated are addressed in Appendix F.

### **2.5.1 VCM Retrieval Examples on MAS Data**

In addition to the VIIRS Cloud Mask (VCM) being developed from simulated cloud imagery, the VCM has also been tested and validated against MODIS Airborne Simulator (MAS) data. In the next chapter Figure 3.1 (right) is an example of the VCM applied over a MAS image, taken during the Arctic Radiation Measurement in Column: Atmosphere-Surface (ARMCAS) campaign of June 1995, in which a large cumulonimbus cloud had formed. In this image on the right is the RGB (Red-Green-Blue) composite image of the 2.14, 1.60, and the 0.65  $\mu\text{m}$  bands, which are used to demonstrate the multispectral capabilities of the VIIRS bands. The MAS bands are spectrally quite similar to the analogous VIIRS bands. The image on the left demonstrates the present VCM being applied over a MAS image. The benefit of testing the VCM against MAS data lies in the great variety of cloud types, optical thicknesses, and underlying surface types these data provide. Also due to the VIIRS bandset being



very 'MODIS/MAS – like' in band positions, the MAS data represent effectively a 'realistic' synthetic VIIRS dataset.

Development of the VCM for application to challenging imagery with snow/ice surfaces has been done. The VCM has been applied over sea/ice MAS data to develop its masking capabilities. Figure 2.12 is an example of an application of the VCM over the sea ice in the Bering Sea from the MAS ARMCAS campaign. The panel to the left is an Red-Green-Blue (RGB) (Red = 1.88  $\mu\text{m}$ , Green=1.6  $\mu\text{m}$ , Blue= 0.55  $\mu\text{m}$ ) composite which demonstrates the multi-spectral capabilities of the VCM, in which the 1.88  $\mu\text{m}$  band is analogous in behavior to the 1.38  $\mu\text{m}$  band of the VCM and the 0.55  $\mu\text{m}$  band is analogous to the 0.65  $\mu\text{m}$  band. In the image one can see the stratus deck quite clearly and the thin cirrus is bright in the 1.88  $\mu\text{m}$  band, depicted as red in this RGB. The image to the right in this figure depicts the VCM results applied over this scene. The capability of the cloud mask to detect thin cirrus clouds, near the bottom of the scene, is noteworthy.

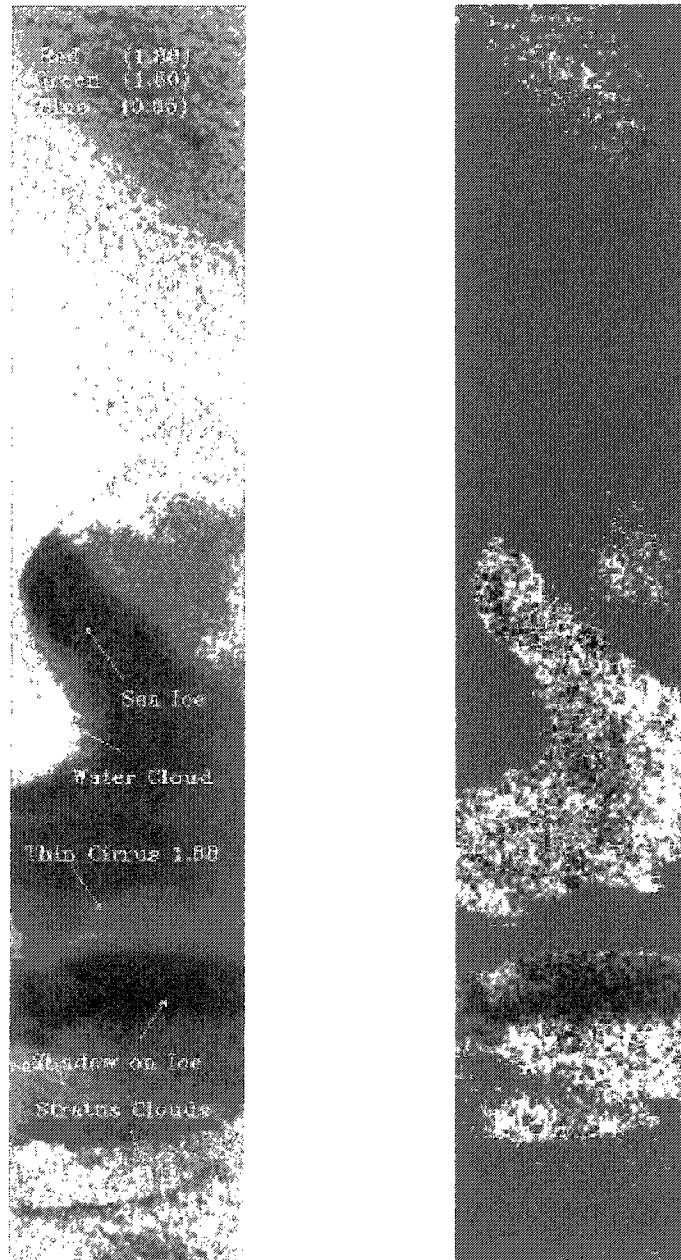


**Figure 2.12:** VCM over sea ice. An RGB composite of MAS imagery and VCM over sea ice. The data were taken during the MAS ARMCAS campaign.

### 2.5.2 Predicted Performance of the Cloud Mask

The probability of correct typing of the cloud mask is shown in Table 2.7 (a-b). These values are based upon the assessed performances of the MCM, which the VCM is expected to equal or exceed, and upon the Cloud Scene Simulation Model (CSSM) and the University of California Los Angeles (UCLA) radiative transfer code simulated scenes used in the VCM development. The assessment of the MCM was performed by a cloud imagery analyst, and the MCM performances are shown in Table 2.7 (a-b).

The probability of correct typing performance of the MCM and thus the VCM was assessed by considering MAS scenes with ice and water clouds, of varying optical thickness. Optical thickness was known for the simulated data, and for MAS scenes it was assessed by the analyst. The probability of correct typing performance of the VCM is in general 99.99% for very thick clouds, of greater than 10.0 optical thickness. The lowest probability of correct typing occur for optically thin clouds at night, being approximately 82%. From Table 2.7 (a-b) one can infer that the performance for the cloud mask for optically thick clouds, of greater than 5.0 optical depth is greater than 99%, while for thin clouds, of less than 0.5 optical depth, the performance range is between 82 and 89%. In general the performance of the cloud mask increases towards Edge of Scan (EOS), and is better at day than at night due to the wealth of spectral information available during day vs. night. Also, over snow/ice and desert surfaces the cloud detection is less reliable than over water and land surfaces.

**Table 2.7 (a):** Daytime probability of correct typing of the VCM.

Cloud Type	Day			Probability of Correct Typing			
	Optical Depth	Nadir	EOS	Vegetated Land	Water	Desert	Snow/ice
Water	0.03 - 0.5	X		87.00	92.00	87.00	88.00
Water	0.03 - 0.5		X	88.00	92.00	88.00	89.00
Water	0.5 - 1.0	X		99.90	98.90	97.00	95.00
Water	0.5 - 1.0		X	99.90	99.10	98.85	96.00
Water	1.0 - 10.0	X		99.96	99.99	98.90	96.00
Water	1.0 - 10.0		X	99.97	99.99	99.50	96.00
Water	> 10.0	X		99.99	99.99	99.99	99.50
Water	> 10.0		X	99.99	99.99	99.99	99.50
Ice	0.03 - 0.1	X		88.00	92.00	90.00	85.00
Ice	0.03 - 0.1		X	89.00	95.00	92.00	88.00
Ice	0.1 - 1.0	X		99.20	97.50	95.00	93.00
Ice	0.1 - 1.0		X	99.25	98.50	96.00	94.50
Ice	1.0 - 10.0	X		99.90	99.94	97.50	95.00
Ice	1.0 - 10.0		X	99.90	99.96	98.50	95.50
Ice	> 10.0	X		99.99	99.99	98.40	96.00
Ice	> 10.0		X	99.99	99.99	98.50	96.50

The greatest potential for increase in performance, and enhanced probability of correct typing, is expected to occur in the optically thin cloud cases and over the desert and snow/ice surface types. It is expected that these values will improve with the proper setting of the cloud detection thresholds and with additional tests being performed by the VCM beyond those done by the MCM. Subpixel cloud detection using the imagery bands is also expected to assist greatly in the detection of clouds, and thus enhance the performance of the VCM.

Table 2.7 (b): Nighttime probability of correct typing of the VCM.

Night				Probability of Correct Typing			
Cloud Type	Optical Depth	Nadir	EOS	Vegetated Land	Water	Desert	Snow/Ice
Water	0.03 - 0.5	X		87.00	90.00	86.00	85.00
Water	0.03 - 0.5		X	88.00	91.00	87.00	86.00
Water	0.5 - 1.0	X		97.50	96.50	94.00	90.00
Water	0.5 - 1.0		X	98.00	97.50	95.00	91.00
Water	1.0 - 5.0	X		98.50	99.50	96.50	92.00
Water	1.0 - 5.0		X	98.75	99.50	97.00	93.50
Water	5.0 - 10.0	X		99.99	99.99	97.50	96.00
Water	5.0 - 10.0		X	99.99	99.99	98.00	97.00
Water	> 10.0	X		99.99	99.99	98.50	98.50
Water	> 10.0		X	99.99	99.99	99.00	99.50
Ice	0.03 - 0.1	X		87.00	90.00	86.00	85.00
Ice	0.03 - 0.1		X	88.00	91.00	87.00	86.00
Ice	0.1 - 1.0	X		93.00	94.00	89.00	87.00
Ice	0.1 - 1.0		X	94.00	95.00	90.00	88.00
Ice	1.0 - 5.0	X		96.00	96.00	94.00	90.00
Ice	1.0 - 5.0		X	96.50	97.50	95.00	91.00

## 2.6 Summary

The background required to derive the Environmental Data Requirement (EDR) of the VIIRS Cloud Mask (VCM) has been explained in this chapter. In explaining the VCM, a review of the processing done by the algorithm has been done, along with necessary data inputs to and outputs from the algorithm. The error budget of the VCM has been discussed by doing a flowdown analysis of error sources and their magnitude. Additionally, the accuracy and precision of the generated binary cloudy/not cloudy result have been studied with both simulated cloud multispectral VIIRS imagery, and with MAS data. The cloud mask described in this chapter is part of the Cloud Cover/Layers EDR developed for the National Polar Orbiting Environmental Satellite System (NPOESS)/VIIRS software package of EDRs.

## Chapter 3

### Effect of Band-to-Band Mis-registration on Cloud Detection

#### 3.0 Band-to-Band Mis-registration Flowdown Study

Band-to-Band Mis-registration (BBM) is a phenomenon which occurs in imagery when pixels from multiple bands are not completely co-registered to the same location on the earth. The BBM is either a result of the sensor imaging optical array defects, focal plane mis-alignment, or a result of errors in geolocation processing. Because the VIIRS Cloud Mask algorithm employs multiple bands which may be mis-registered, it is considered sensitive to BBM. An assessment of the effects of BBM on the VCM is presented in this chapter.

To assess the effects of BBM a flowdown study was done using a set of multi-spectral imagery bands analogous to those used by the VCM. This multi-spectral imagery was a representative MODIS Airborne Sensor (MAS) scene, illustrated in Figure 3.1. This scene contains a variety of cloud types (cumulus, cumulonimbus, and cirrus) over a uniformly vegetated land surface. All of the multi-spectral bands used by the VCM were mis-registered at two magnitudes, 0-30% and 0-60%. This MAS scene was selected because it is an example of an easy cloud detection case over a uniform surface, in which clouds should be correctly flagged in well registered imagery. For mis-registration by the algorithm every band has been randomly shifted by different amounts and the Root Mean Square (RMS) mis-registration determined. The RMS mis-registration is used to quantify the the total mis-registration of all the bands for a given cloud-mask generation. A total of 800 of these mis-registered masks were performed, producing a large statistical ensemble of simulations of the VCM to assess the effect of BBM on both the cloud mask misclassification and the cloud cover accuracy and precision.

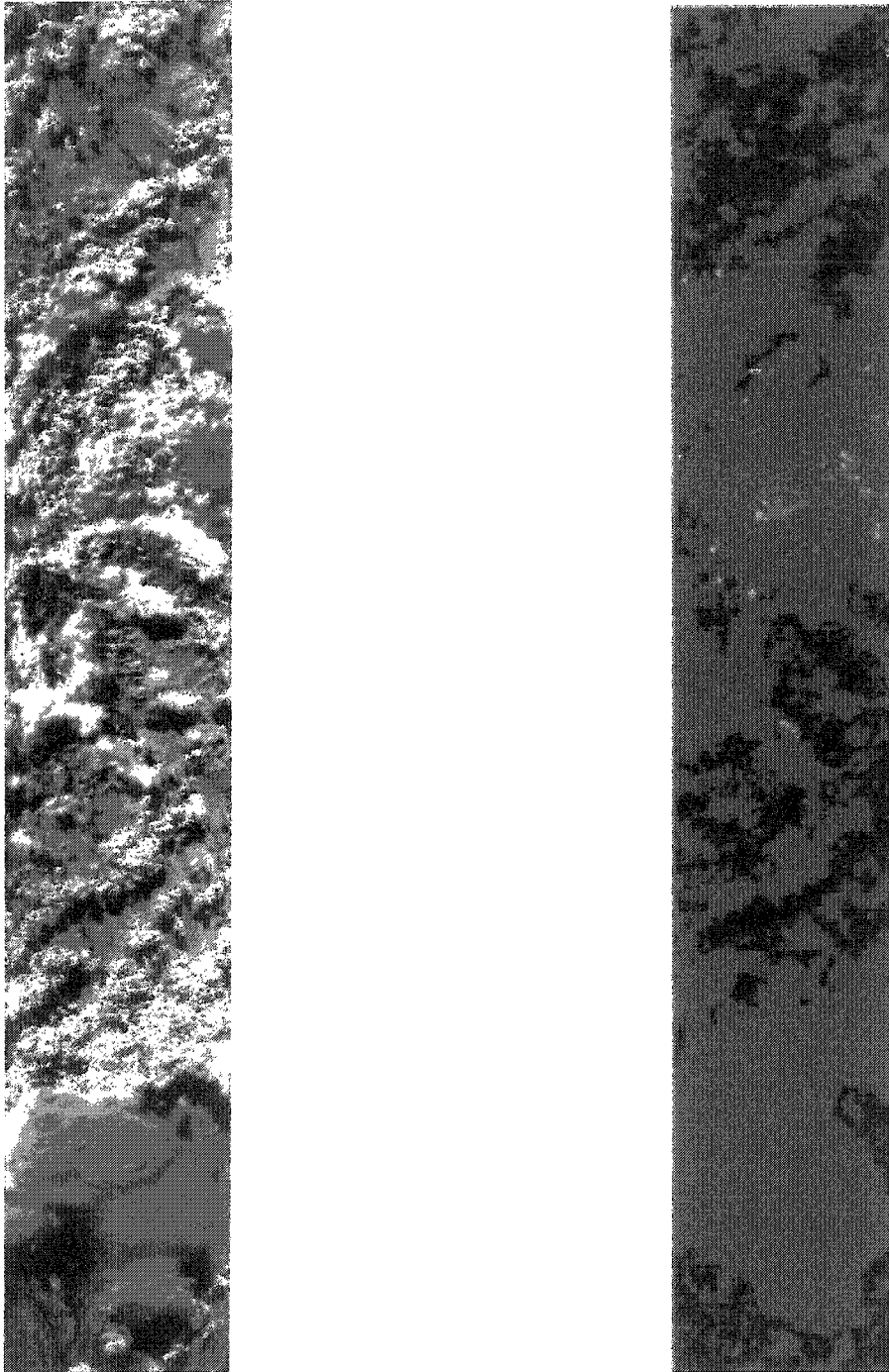


**Figure 3.1:** MAS scene used in BBM study. Figure on left an RGB of the scene. Figure on right is the VCM results overlaid on the 0.645  $\mu\text{m}$  band.



### 3.1 Analysis

The flowdown of this BBM study was performed with one cloudy MAS scene at a resolution of 50 m (at nadir). Cloud mask truth was computed by aggregation of all the multi-spectral imagery used to a horizontal size of 1.3 km. the TOA radiances in seven MAS bands were used by the VCM to determine cloudy pixels. The solar zenith angle was taken from the MAS data. The MAS scene is shown as Figure 3.1 (left image), at a resolution of 50 m, at nadir. Figure 3.1 (right image) shows the cloud mask truth at 1.25 km horizontal cell size.

The effect of BBM was simulated by displacing the 50 m multi-spectral MAS imagery for each band by a random number of integer steps in both cross-track (X) and along-track (Y) directions. Simulated mis-registrations are therefore quantized by 50 m, equivalent to 1/13 of a Ground Sample Distance (GSD) for a GSD = 0.65 km, and 1/25 of a GSD for a GSD = 1.25 km. The quantization limit was set by the inherent resolution of the original MAS scene. There were 800 simulated mis-registrations generated, to represent a spectrum of mis-registrations over a range of +/- 0.5 GSD in each direction. As mentioned above, all of the multi-spectral bands used by the VCM were mis-registered at two magnitudes, 0-30% and 0-60%.

Each randomly mis-registered MAS image then had the multi-spectral radiances converted to reflectances or Brightness Temperatures (BT), for input to the VCM algorithm. These reflectances and BT-values were used in the VCM for cloud detection.

The VCM was then applied to retrieve cloudy/clear results. The misclassification of the mis-registered images cloud mask was then determined from the cloud mask truth, at the 1.3 km horizontal cell size. 800 computed misclassifications were derived, corresponding to 5600 random band mis-registrations. The misclassification of the scene versus the RMS mis-registration is shown in Figures in this chapter, where the RMS mis-registration is given by:

$$\text{RMS mis-registration} = \text{SQRT}(\Sigma\Delta X^2 + \Sigma\Delta Y^2) \quad (3.1)$$

where  $\Delta X$  and  $\Delta Y$  are the random distributions in the vertical and horizontal directions respectively. Note that X and Y were considered for both positive and negative shifting. The random number generator used is Gaussian with different seeds used for each mis-registration case. This provides the mean random mis-registration of the masked scene considered, which is then plotted against the percent misclassification of the mis-registered scene from the true cloud mask, as illustrated in Figure 3.2.

### 3.2 Assumptions

There are a number of assumptions considered in the BBM study that should be mentioned. The BBM has been modeled as a random variation in cross-track and along-track directions, with the mis-registration of each band uncorrelated with that of any other band. A real focal plane/scan design however, will have correlated mis-registrations. A sensor-design based analysis accounting for correlated mis-registrations of known sensor effects would be considered more reliable. However until the sensor is operational, the degree of correlated mis-registrations of the multi-spectral bands is unknown.

The along-track pixel size is additionally assumed to be equal to the cross-track size (square “pixels”), while the actual sensor will have pixel growth towards Edge of Scan (EOS) and unequal along-track and along-scan pixel size. This leads to the assumption that the MAS data pixels could be treated as being 50 m out to the EOS, where pixels are approximately 74 m. All pixels within the MAS data scenes are treated as being at the same. Another assumption is that the error in MAS data radiances are not considered a factor in BBM. As with the correlation of the multi-spectral bands, a future sensor-design based analysis is recommended to assess radiance errors.

Also, errors due to Modulation Transfer Function (MTF), the sensitivity of the sensor to varying spatial frequencies of imagery, are not considered in BBM. It is

desirable to consider both sources of error in the same analysis. This analysis has not done so. Non-spatial errors are for this study assumed to be uncorrelated with MTF and resultant BBM errors. Additionally, stray light (far field) focal plane errors are assumed to be uncorrelated with MTF (near field) errors. No image restoration, MTF repair, has been performed upon the multi-spectral imagery prior to the BBM. For a more accurate assessment of BBM effects a complete flowdown of spatial errors would need to include the multi-spectral bands MTF, and also MTF repair. This is proposed to be included as part of future sensor studies for the post-launch VIIRS system.

### **3.3 Effect of BBM on Cloud Mask and Cloud Cover**

The BBM explained in the Analysis section above was performed in order to assess the effects of BBM on VCM misclassification. The RMS mis-registration given by Eq. (3.1) provided the mean random mis-registration of the multi-spectral radiances used in the VCM. When the RMS mis-registration is plotted against the percent misclassification of the mis-registered scene from the true cloud mask, Figure 3.2 (a-c), the BBM was found to affect the VCM significantly .

The BBM was found to increase the misclassification of the cloud mask, with BBM greater than 20% having the greatest effects. Looking at Figure 3.2(a), the BBM of greater than 20% created a 4-12% total misclassification of the cloud, with a mean of approximately 8%. On the other hand, a mis-registration of less than 20% creates a total misclassification of up to 6%, with a mean of approximately 3%.

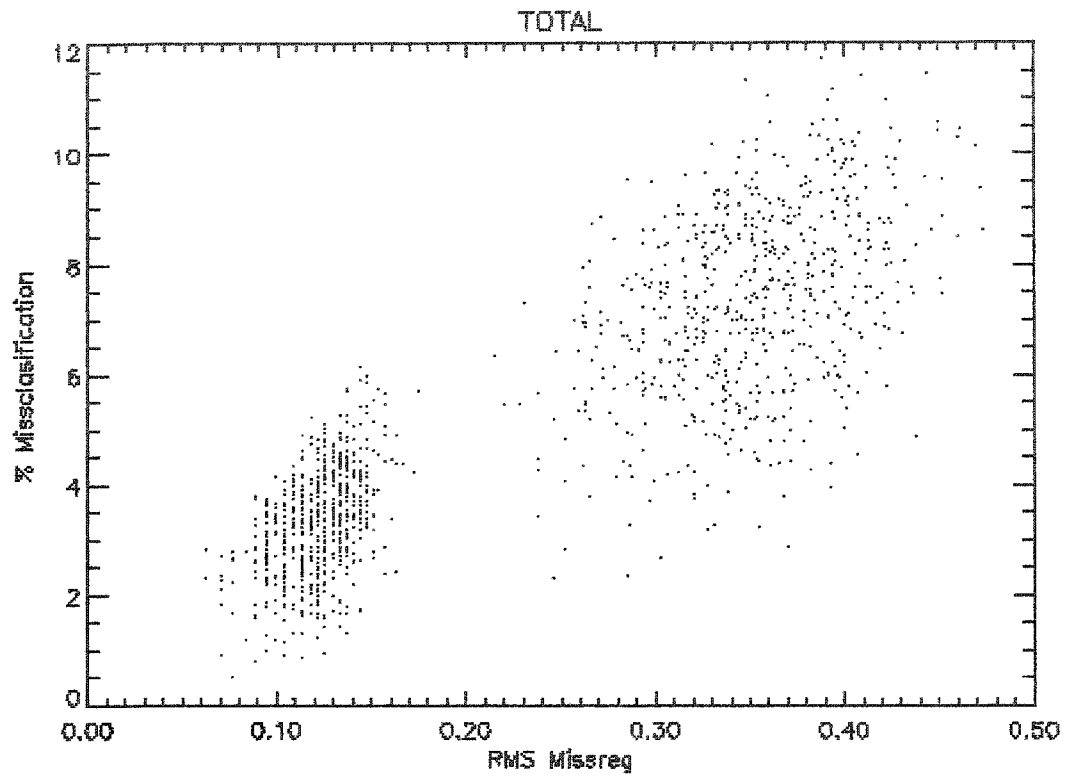
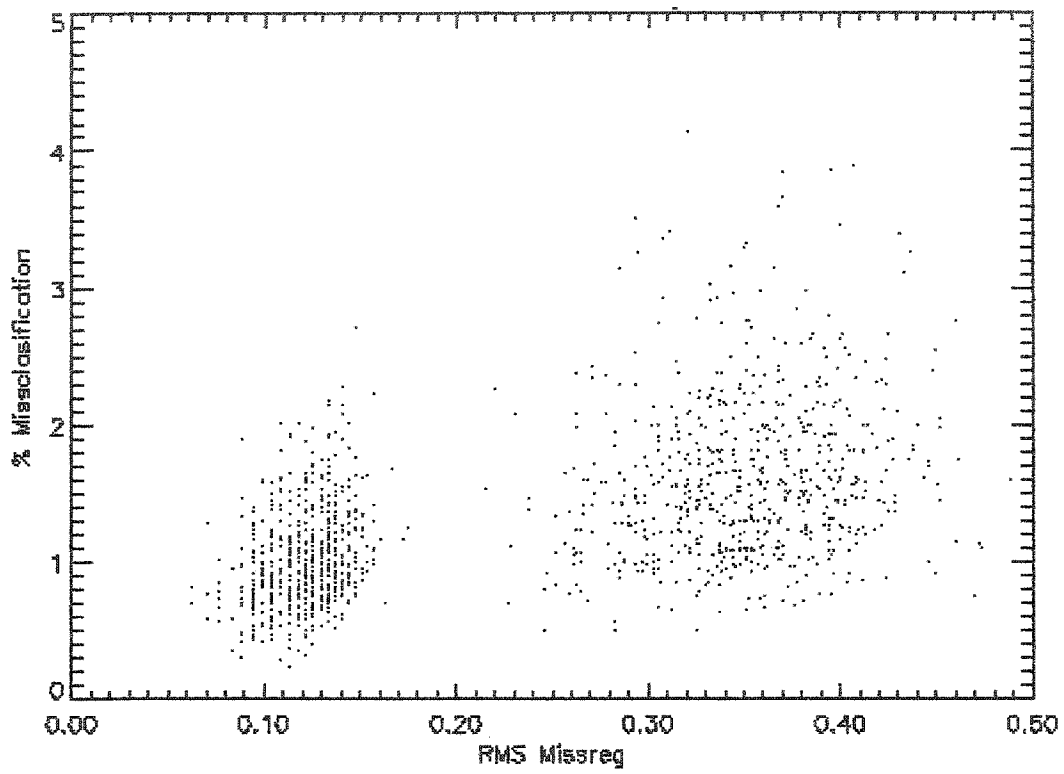
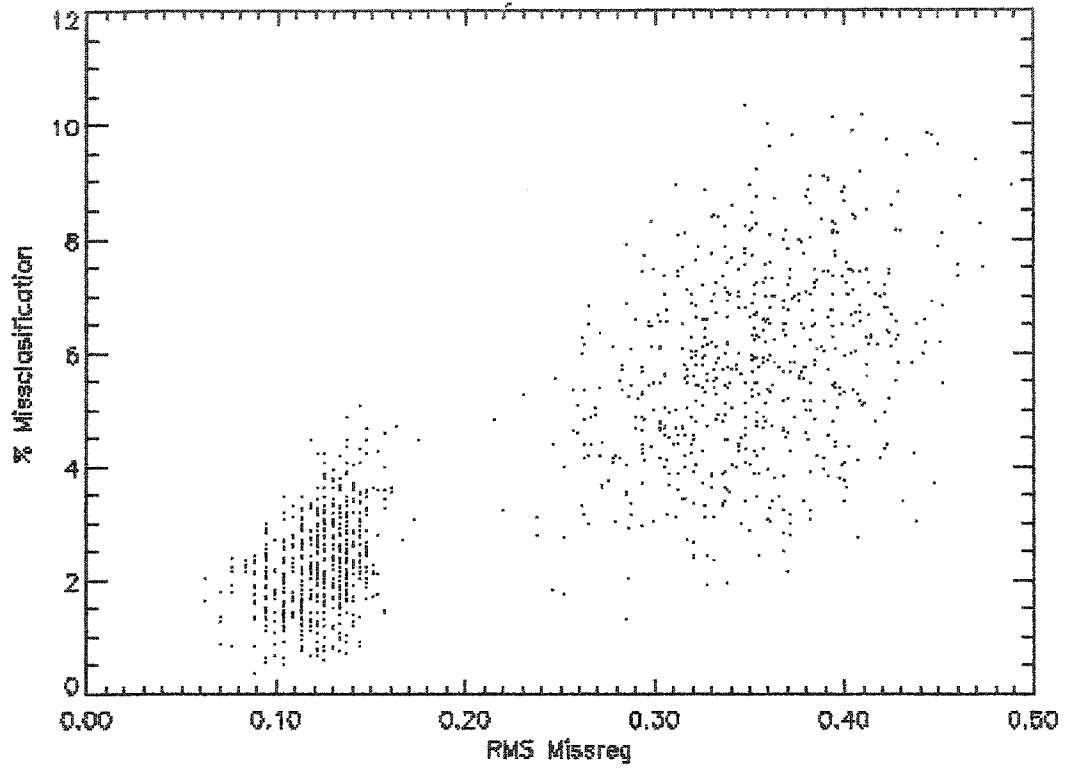


Figure 3.2 (a): Total misclassification due to BBM.



**Figure 3.2 (b):** The cloudy-when-clear misclassification due to BBM.



**Figure 3.2 (c):** The clear-when-cloudy misclassification due to BBM.

A significant finding was that this misclassification of the cloud mask may be divided into two components, cloudy-when-clear (Figure 3.2(b)) and clear-when-cloudy (Figure 3.2(c)). For mis-registration less than 20% the cloudy-when-clear component has a mean of approximately 2%, while the clear-when-cloudy component has a mean of approximately 1%. For a BBM greater than 20% the cloudy-when-clear component has a mean of approximately 7%, while the clear-when-cloudy component has a mean of approximately 2%.

From these misclassifications, illustrated in Figure 3.2(a-c), one infers that the effect of a BBM on the cloud mask is significant when the mis-registration is greater than 20%. Also, the ratio of cloudy-when-clear to clear-when-cloudy misclassifications was found to increase as a result of BBM, going from a ratio of 2:1 to a ratio of 7:1 (producing biased results).

Because the largest misclassification component is the cloudy-when-clear one the misclassification caused by BBMs will have the greatest effect on the cloud products, causing clear regions to be misclassified as cloudy more often than cloudy regions as clear. These errors of omission/commission do not affect the accuracy of other land products dependent on the cloud mask, but will cause clear regions not to be considered by the land products and in turn adversely affect the accuracy and precision of the cloud products.

The cloud masks misclassification as a result of BBMs is summarized in Table 3.1. Note that the values do not depict the full ranges of misclassifications, but seek to summarize the overall results.

If no BBMs were assured by the instrument design the cloud mask could operate on a 2x2 aggregate. However running the mask at lower spatial resolution causes increased errors in misclassification.

**Table 3.1:** Effect of BBM upon cloud mask misclassification.

<b>RMS Mis-registration</b>	<b>&lt; 10%</b>	<b>10% – 20%</b>	<b>20% - 30%</b>	<b>30% - 40%</b>
<b>Total</b>	2%	4%	7%	10%
<b>Cloudy When Clear</b>	1%	1.5%	2%	2%
<b>Clear When Cloudy</b>	1%	2.5%	5%	8%

The BBM explained in the Analysis section, and the VCM misclassification sections above was also considered in the generated cloud cover Horizontal Cell Size (HCS) accuracy and precision. This was performed in order to assess the effects of BBM on cloud cover accuracy and precision. The cloud cover itself is a VIIRS product, as was explained in Chapter 1, which is a result of the VCM. The cloud cover is a ratio of the number of cloudy pixels in a scene to the total number of pixels in the scene. Misclassification errors in the cloud mask, due to BBMs, would therefore propagate into the cloud cover accuracy and precision. The RMS mis-registration given by Eq. (3.1) provided the mean random mis-registration of the multi-spectral radiances used in the VCM. Therefore, the RMS mis-registration may be plotted against the cloud cover accuracy and precision of the mis-registered scene. As illustrated in Figure 3.3 (a-h), BBMs have significant effects upon the cloud cover accuracy and precision.

Studies were performed to assess the effect of cloud mask mis-registration upon the accuracy and precision of cloud cover as a function of HCS. Figures 3.3(a-h) depict the accuracies and precisions for a given HCS for varying degrees of mis-registration.

For cloud cover, cases of mis-registration were unable achieve threshold accuracy at a 2 km objective HCS, for all BBMs considered, 10-60%. For HCS greater than 6 km, the cloud cover has an accuracy better than threshold, and in some cases better than objective, for BBMs less than 20%.



For BBMs greater than 20%, there is a severe effect upon the cloud cover. Referring to Figures 3.3(a-h) one may assess the performance of the cloud cover due to BBMs. At the 2 km objective HCS, the cloud cover accuracy did not reach threshold with a mean accuracy of 0.2, twice the objective, and a standard deviation of approximately 0.05, based the on 2.5 km HCS BBM results illustrated in Figure 3.3 (g-h).

For lower resolution cloud cover BBMs were found to have pronounced effects. For a cloud cover assessed over 6.5 km HCS, Figure 3.3(e-f), the mean of the accuracy obtained is at the threshold for cloud cover 0.1, with a standard deviation of approximately 0.04. At a cloud cover assessed over 13 km HCS, the mean accuracy of the cloud cover is below threshold, being 0.08, with a standard deviation of 0.04. At a cloud cover assessed over a cloud cover at the 25 km threshold HCS the accuracy has a mean of 0.07 with a standard deviation of 0.04. For this latter case, it is worth noting that approximately 30% of the results inspected did not make threshold of 0.1 accuracy.

The precision of the cloud cover has also been found sensitive to mis-registration, illustrated in Figure 3.3(a-h). For all HCSs considered greater than 6 km, cloud cover precision reached objective,  $<0.15$ , and was better than threshold at a threshold HCS of 25 km. At a threshold HCS of 2 km the precision did not reach objective. The cloud cover was found to have better precision at lower mis-registrations and as the cloud cover HCS was increased. In Figure 3.3(a-h) the mean of the distributions (solid line) and the standard deviation (dashed lines) are also illustrated..

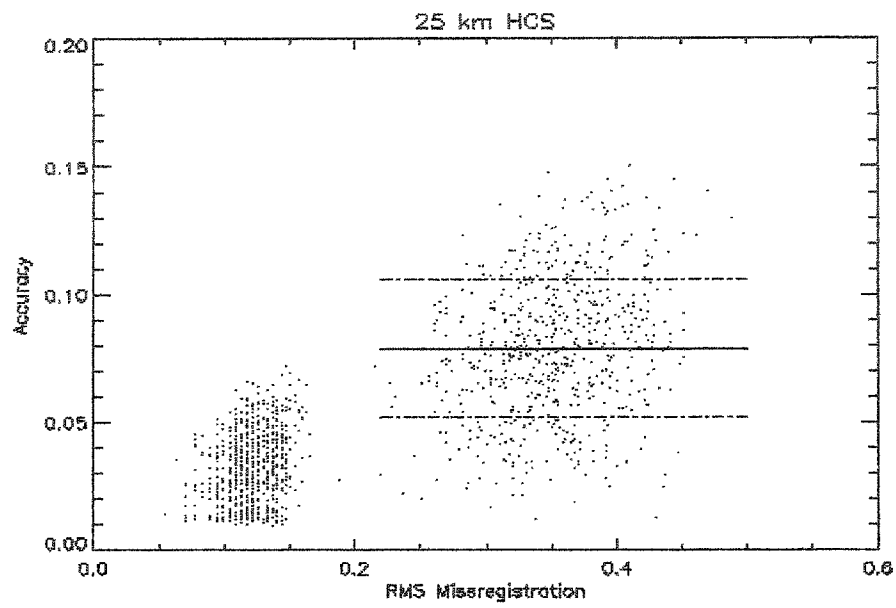


**Figure 3.3 (a):** Cloud cover accuracy for 25 km HCS.

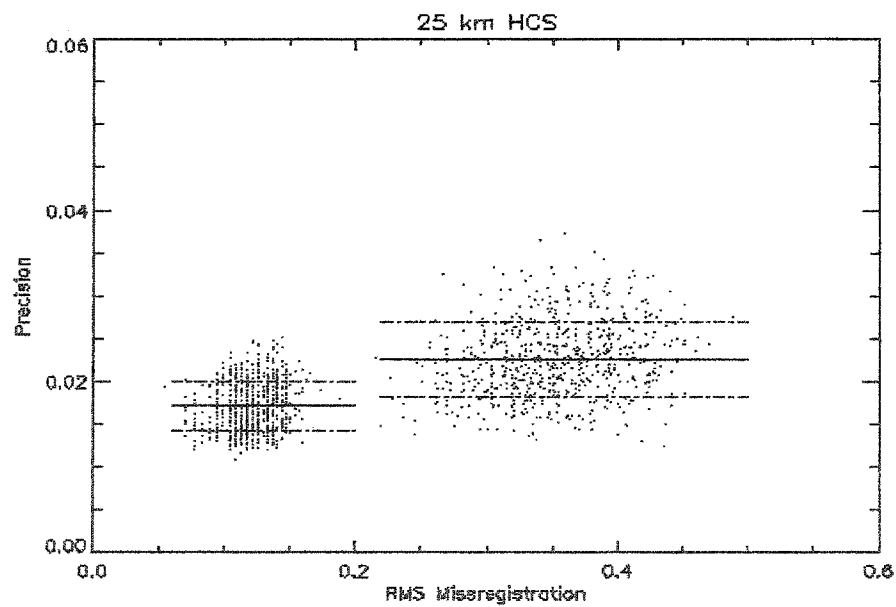


**Figure 3.3 (b):** Cloud cover precision for 25 km HCS.

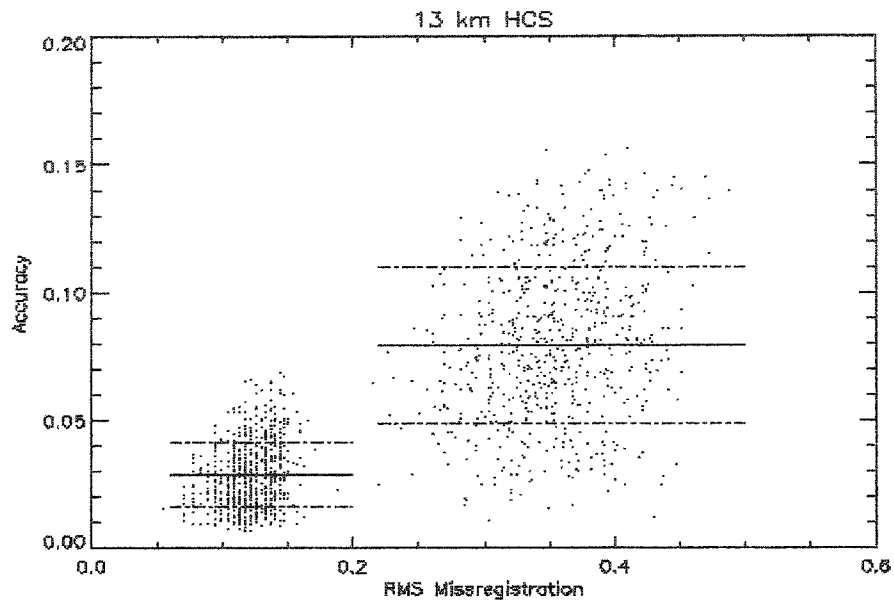


**Figure 3.3 (c):** Cloud cover accuracy for 13 km HCS.

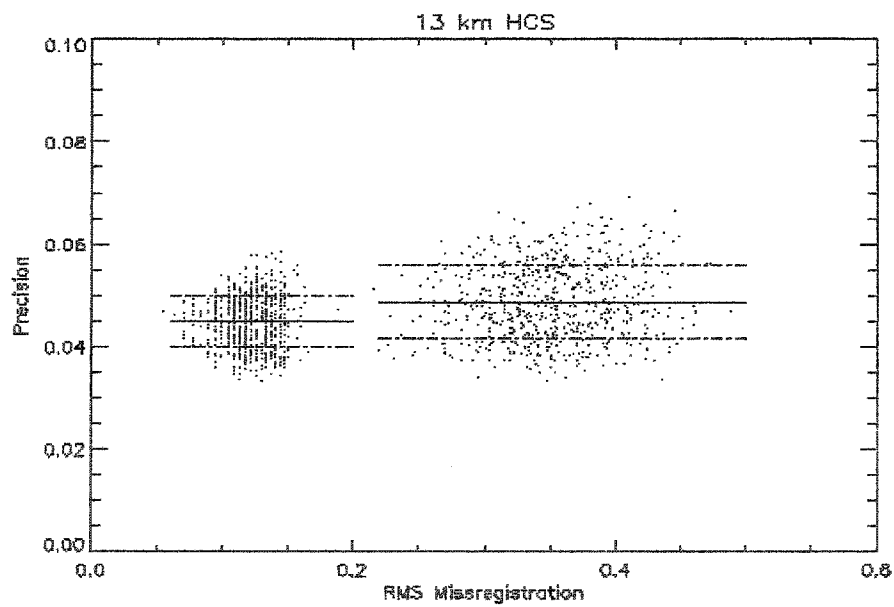


**Figure 3.3 (d):** Cloud cover precision for 13 km HCS.

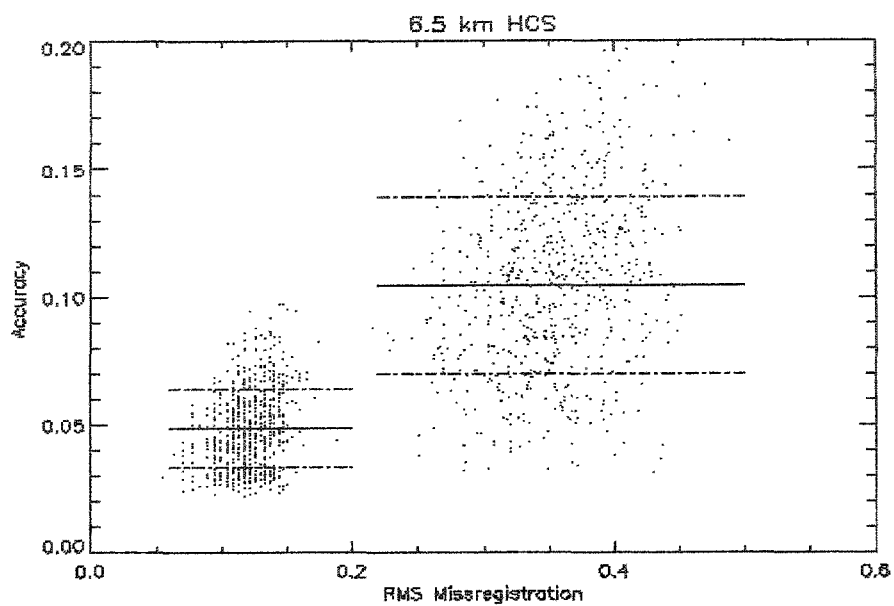


**Figure 3.3 (e):** Cloud cover accuracy for 6.5 km HCS.

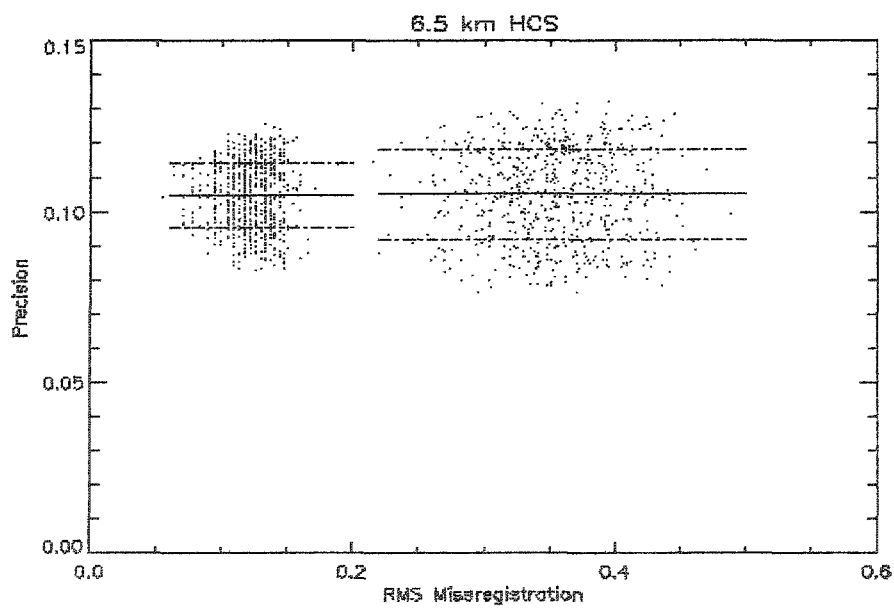


**Figure 3.3 (f):** Cloud cover precision for 6.5 km HCS.

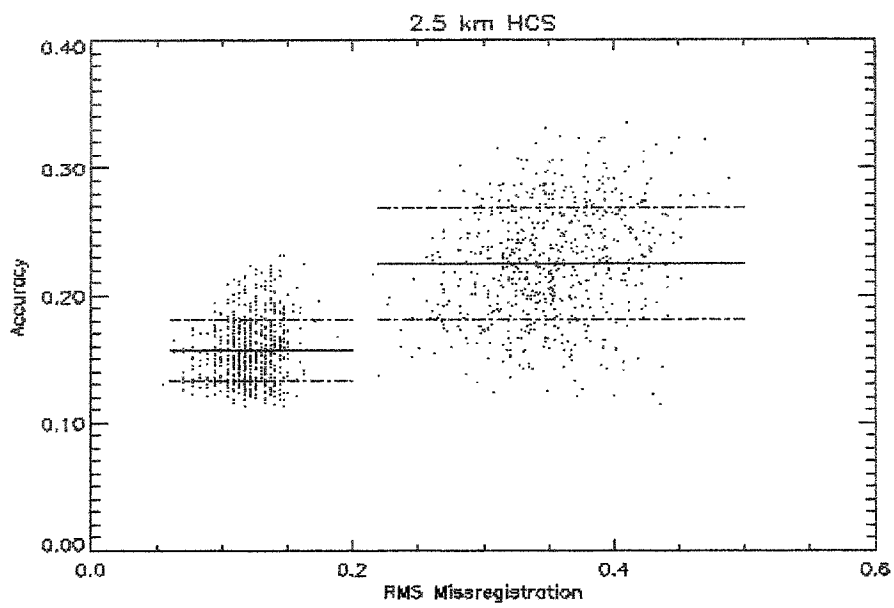


**Figure 3.3 (g):** Cloud cover accuracy for 2.5 km HCS.

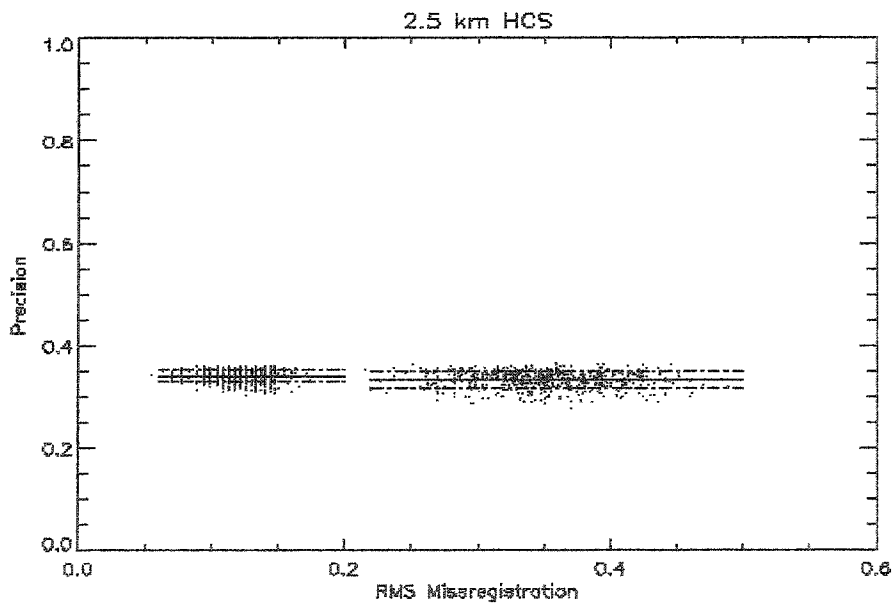


**Figure 3.3 (h):** Cloud cover precision for 2.5 km HCS.

The conjecture is that a BBM error less than 20% is sufficient to meet requirements down to a HCS of 6.5 km. Larger than 20% mis-registration results in an inability to meet accuracy requirements for the Cloud Cover EDR (*NPOESS IPO*, 2000a). In addition to the above, BBMs larger than 20% has a significant effect on the Cloud Cover EDR performance. Cloud cover is an aggregation of the cloud mask results. As a result of this, the misclassification of the cloud mask discussed above has a significant impact upon the inferred cloud cover.

The cloud cover misclassification as a result of BBMs discussed above is summarized in Table 3.2a-b. Note that the values do not depict the full ranges of misclassifications, but seek to summarize the overall results.

**Table 3.2 (a): Effect of BBM upon cloud cover accuracy.**

RMS Mis-registration	< 10%	10% – 20%	20% - 30%	30% - 40%
25 km HCS Accuracy	0.03	0.05	0.08	0.09
13 km HCS Accuracy	0.03	0.05	0.09	0.10
2.5 km HCS Accuracy	0.15	0.18	0.22	0.25

**Table 3.2 (b): Effect of BBM upon cloud cover precision.**

RMS Mis-registration	< 10%	10% – 20%	20% - 30%	30% - 40%
25 km HCS Accuracy	0.02	0.02	0.025	0.03
13 km HCS Accuracy	0.05	0.05	0.05	0.06
2.5 km HCS Accuracy	0.30	0.30	0.30	0.30

For mitigation of this significant BBM effect cloud cover can be produced by first aggregating 2x2 pixels. These will then be collected to the relevant HCS level. This sum-algorithm-sum technique would mitigate BBM errors. However, this cannot be done without introducing additional errors of the type described in the cloud mask

above. This is considered a possible method to minimize BBM effects. Results of these studies have led to a systems specification for the VIIRS sensor to keep band-to-band mis-registration less than 20%.

### 3.4 Conclusions

A band-to-band mis-registration study has been performed in which the radiance of all bands used by the VCM were mis-registered horizontally and vertically. Multi-spectral MAS imagery was used as a surrogate for VIIRS. This multi-spectral imagery was generated with band-to-band registration errors of different degrees, and automated analyses of simulated imagery were then compared against ground truth cloud masks used to generate the synthetic data.

It was found that the misclassification may be divided into two components, depicted in Figure 3.2 (b-c). A misclassification of clear when the pixel is cloudy, and a misclassification of cloudy when the pixel is clear. The larger term of these two misclassifications is the cloudy when clear. This means that the cloud EDRs will be affected the greatest by misclassifications of the cloud mask, while surface EDRs, which are retrieved in regions the cloud mask designates as clear, are affected the least. In essence a 'cloud confident' cloud mask results in misclassification errors more likely to classify clear regions as cloudy. This causes misclassified regions to be more likely to be passed onto the cloud EDRs than other EDRs.

This behavior is believed to be due to the cloud conservative behavior of the cloud mask itself. For example the ratio of clear when cloudy to cloudy when clear misclassifications is roughly equal for BBM less than 20%, but as misclassification increases beyond 20% results have shown that the ratio goes as high as 7:1. Large BBMs have their largest effects upon surface EDRs, which are determined when a cloud is not detected. Therefore, it is recommended that BBMs be kept less than 20%.

The effects of BBMs upon cloud cover of varying HCS were also assessed. The conjecture is that a BBM error less than 20% is sufficient to meet requirements down to a HCS of 6.5 km. Larger than 20% mis-registration results in an inability to meet accuracy requirements for the Cloud Cover EDR (*NPOESS IPO*, 2000a). In addition to the above, BBMs larger than 20% have a significant effect on the Cloud Cover EDR performance. Cloud cover is an aggregation of the cloud mask results. As a result of this, the misclassification of the cloud mask discussed above has a significant impact upon the inferred cloud cover.

These studies of BBM effects have shown that band-to-band RMS mis-registrations greater than 20% can lead to misclassifications of greater than 10% in the VCM. Also, BBMs affect the clear when cloudy misclassification much more than the cloudy when clear misclassification. These studies resulted in a VIIRS sensor specification to requirement that BBMs be kept less than 20% (*Larsen*, 2000b; *Kealy and Ardamy*, 2000a).



## Chapter 4

### Use of Shadows to Retrieve Water Vapor in Hazy Atmospheres

#### 4.0 Introduction

Techniques aimed at retrieving water vapor from satellite data of reflected near-infrared solar radiation have progressed significantly in recent years. These techniques rely upon observation of water vapor attenuation of near infrared solar radiation reflected by the Earth's surface. Ratios of measured radiances at wavelengths inside and outside of water vapor absorbing channels are used for retrieval purposes. These ratios partially remove the dependence of surface reflectance on wavelength, and are used to retrieve the total column water vapor amount. Hazy atmospheric conditions, however, introduce errors into this widely used technique. A new method based upon radiance differences between clear and nearby shadowed surfaces, combined with ratios between water vapor absorbing and window regions, is presented which improves water vapor retrievals under hazy atmospheric conditions. Radiative transfer simulations are used to demonstrate the advantage offered by this technique. This chapter has been submitted for publication (*Larsen and Stamnes, 2005a*).

Water vapor is an important variable constituent of the atmosphere. It plays an important role in the redistribution of water and energy within the global atmosphere-land-ocean system. The annual average of columnar water vapor varies between 0.25 g/cm<sup>2</sup> in polar regions, to 5 g/cm<sup>2</sup> in the tropics (*Peixoto and Oort, 1992*).

Prior to the 1990's remote sensing of water vapor from space utilized costly sensors based on measurements of Infra-Red (IR) and microwave radiation emitted by the atmosphere. Methods employing the split window technique in the 11.0 - 13.0  $\mu\text{m}$  were developed for the retrieval of total column water vapor amount over the oceans, and over land areas covered by green vegetation (*Chesters et al., 1983*). For the remote

sensing of water vapor profiles the IR emission channels have historically been used in conjunction with an initial guess of atmospheric temperature and moisture profiles in the inversion (*Suskind et al.*, 1984). In addition, passive microwave remote sensing techniques were developed that work well over the ocean, but have limitations over land surfaces (*Prabhakara et al.*, 1982; *Ferraro et al.*, 1996).

Research in the late 1980's and throughout the 1990's has led to the development of a total column water vapor retrieval algorithm using backscattered Near-InfraRed (NIR) solar radiance near 1  $\mu\text{m}$  (e.g., *Conel et al.*, 1988; *Gao and Goetz*, 1990; *Frouin et al.*, 1990; *Kaufman and Gao*, 1992; *Borel et al.*, 1996; *Bouffies et al.*, 1997; *Thai and Schonermark*, 1998; *Vesperini et al.*, 1999). A major benefit of this approach is that it employs channels near 1  $\mu\text{m}$ , which significantly reduces the cost to build sensors. This technique has been further developed into an operational tool for total water vapor retrieval (*Gao et al.*, 2003), which is currently used to retrieve the total column water vapor amount from the Moderate Resolution Imaging Spectroradiometer (MODIS), (*Salomonson et al.*, 1989) deployed on the NASA Terra and Aqua spacecraft platforms. An inherent limitation to this technique is that under hazy atmospheric conditions (with visibilities less than 10 km), or when surface reflectance near 1  $\mu\text{m}$  is small, the derived amounts in total column water vapor may be off by as much as 10% if aerosol effects are not properly corrected for (*Gao and Kaufman*, 1998). To compensate for the atmospheric aerosol effects an aerosol correction module has been developed. This module employs Look Up Tables (LUTs) generated from radiative transfer simulations based on DISORT (*Stamnes et al.*, 1988). This chapter presents a method which helps eliminate the effects of haze on the retrieved water vapor column by using Top of Atmosphere (TOA) radiances from clear as well as nearby shadowed regions.

#### 4.1 Overview and Background

As stated above the NIR technique for column water vapor retrieval is based on measured TOA radiances within the water absorption band located at 945 nm, as illustrated in Figure 4.1. This figure as well as all the other computations reported on in this chapter are based on MODTRAN (*Berk et al.*, 1989; *Anderson et al.*, 2000). The retrieval of total column water vapor is based on the use of reflected radiances within this water vapor absorption band and in a channel just outside this band. The radiance within the absorption band measured by the satellite-deployed sensor is due to sunlight that has been attenuated by atmospheric water vapor absorption along its path from the TOA to the surface, and after reflection by the surface, attenuated once more along its path from the surface to the entrance aperture of the sensor. Sunlight in a nearby window region outside the water vapor absorption band follows similar radiometric paths except that it is not subject to water vapor absorption.

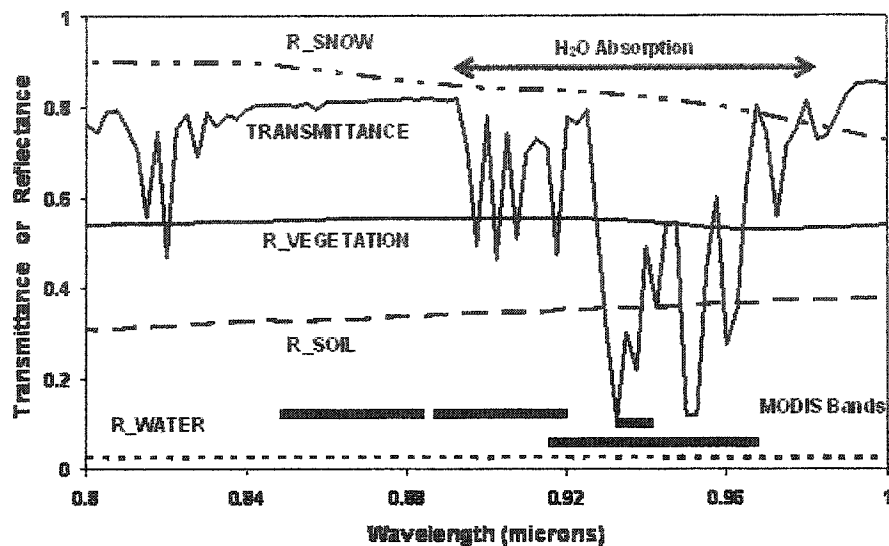


**Figure 4.1:** Atmospheric transmission across the NIR spectral region. Spectral transmission of the midlatitude summer atmosphere (*McClatchey et al.*, 1972; *Anderson et al.*, 1986), with rural aerosol extinction (visibility 25 km), an overhead sun and a nadir view in the presence of water vapor. The water vapor absorption region, the MODIS Near-Infrared bands, and the spectral reflectance of snow, vegetation, soil, and water surfaces are also shown.

A disadvantage of using the NIR region for water vapor retrieval compared to longer IR wavelengths is that aerosol scattering can be significant. For clear sky conditions, however, atmospheric scattering is small and may not be ignored. This is not true for low visibility conditions, and this is the problem addressed in this chapter. The monochromatic radiance at wavelength  $\lambda$  measured by a downward looking spaceborne sensor can be approximated (*Hansen and Travis, 1974; Thomas and Stamnes, 1999*) as:

$$I_{\lambda}(\theta_v, \theta_o, \Delta\phi) = I_{\lambda, \text{diff}}(\theta_v, \theta_o, \Delta\phi) + \frac{\mu_o F_{o\lambda}}{\pi} T_{\lambda}(\theta_o) T_{\lambda}(\theta_v) \rho_{\lambda}(\theta_v, \theta_o, \Delta\phi) \quad (4.1)$$

where  $F_{o\lambda}$  is the extraterrestrial solar irradiance (normal to the solar beam),  $\theta_o$  is the solar zenith angle,  $\mu_o = \cos\theta_o$ ,  $\theta_v$  is the sensor viewing angle, and  $\Delta\phi$  is the difference in azimuth between the sun and the sensor. The amount of attenuated sunlight striking the surface in direction  $\theta_o$  that is reflected in direction  $(\theta_v, \Delta\phi)$  of the sensor is described by  $\rho_{\lambda}(\theta_v, \theta_o, \Delta\phi)$ , the Bidirectional Reflection Distribution Function (BRDF). The second term in Eq. (4.1) is due to radiance that is directly transmitted through the atmosphere, first in the downward direction described by the direct transmittance  $T_{\lambda}(\theta_o)$ , and then (after reflection by the surface) in the upward direction towards the sensor described by the direct transmittance  $T_{\lambda}(\theta_v)$ . This term can be evaluated by atmospheric transmittance codes such as LOWTRAN (*Kneizys et al., 1988*), FASCODE (*Clough et al., 1986*) based upon tabulated water vapor absorption cross sections (available for example in the HITRAN database (*Rothman et al., 1998*)) provided the BRDF,  $\rho_{\lambda}(\theta_v, \theta_o, \Delta\phi)$  is known.

The diffuse or scattered radiation due to multiple scattering is described by the first term  $I_{\lambda,diff}(\theta_v, \theta_o, \Delta\phi)$  which is much more problematic because it involves scattering by atmospheric aerosols whose optical properties, including absorption and scattering coefficients and optical depth (depending on mass loading), are poorly known. In fact, these optical properties are known to vary considerably in space and time. Moreover, they depend on the chemical composition of the aerosol particles as well as their increase in size and resulting change in the index of refraction due to uptake of water in response to increased humidity which in turn depends on the atmospheric water vapor content (*Shettle and Fenn, 1976; Tsay and Stephens, 1990; Yan et al., 2002*), the column amount of which is desired to measure. Finally this term also depends on the surface BRDF,  $\rho_\lambda(\theta_v, \theta_o, \Delta\phi)$ .

Nevertheless, in high visibility situations (low aerosol loading), it may be justifiable to ignore this term due to scattering and absorption by aerosols as well as the radiance contribution due to scattering by molecules (Rayleigh scattering) which is small in the NIR spectral range. Then, if one invokes the customary assumption that the surface is a Lambertian reflector so that the BRDF is isotropic, i.e.,  $\rho_\lambda(\theta_v, \theta_o, \Delta\phi) \equiv \rho_{\lambda,L}$ , Eq. (4.1) reduces to (*Fraser and Kaufman, 1985; Gao and Kaufman, 2003*):

$$I_\lambda(\theta_v, \theta_o, \Delta\phi) = \frac{\mu_o F_{o\lambda}}{\pi} T_\lambda(\theta_o) T_\lambda(\theta_v) \rho_{\lambda,L} \quad (4.2)$$

The water vapor absorption feature in the 1  $\mu\text{m}$  NIR spectral region is attractive for retrievals of water vapor because this technique relies on the assumption that the surface reflectance,  $\rho_{\lambda,L}$ , is uniform or varies linearly with wavelength across both the absorption region and the nearby window region used for retrieval. Also, for this retrieval algorithm to be reliable the surface reflectance must be greater than 0.1, which is true for vegetated surfaces, desert regions, and snow, but not for ice or liquid water.

Figure 4.1 depicts the surface reflectance of four common surface types across this spectral region.

If one divides Eq. (4.2) by the incident irradiance,  $\mu_o F_{o\lambda}$ , one obtains the (radiance) reflectance, defined as:

$$\rho_\lambda(\theta_v, \theta_o, \Delta\phi) \equiv \frac{I_\lambda(\theta_v, \theta_o, \Delta\phi)}{\mu_o F_{o\lambda}} = \frac{T_\lambda(\theta_o)T_\lambda(\theta_v)\rho_{\lambda,L}}{\pi} \quad (4.3)$$

and if one also multiplies by  $\pi$  one obtains the *apparent* (radiance) reflectance, defined as:

$$\rho_\lambda^*(\theta_v, \theta_o, \Delta\phi) = \pi\rho_\lambda(\theta_v, \theta_o, \Delta\phi) = T_\lambda(\theta_o)T_\lambda(\theta_v)\rho_{\lambda,L} \equiv T_\lambda^{tot}(\theta_v, \theta_o)\rho_{\lambda,L} \quad (4.4)$$

having defined the total transmittance,  $T_\lambda^{tot}(\theta_v, \theta_o) \equiv T_\lambda(\theta_o)T_\lambda(\theta_v)$ , as the product of the downward direct and upward direct transmittances. Applying Eq. (4.4) to the water vapor absorption band (denoted by subscript 1) as well as the nearby window region (denoted by subscript 2), and taking the ratio produces:

$$\frac{T_1^{tot}(\theta_v, \theta_o)}{T_2^{tot}(\theta_v, \theta_o)} = \frac{\rho_1^*(\theta_v, \theta_o, \Delta\phi) / \rho_{L,1}}{\rho_2^*(\theta_v, \theta_o, \Delta\phi) / \rho_{L,2}} \quad (4.5)$$

Here there is an assumption that the same sun/sensor geometry and surface reflectances apply for both bands. Thus, when the scattered radiation can be ignored Eq. (4.5) shows that if the surface reflectance is independent of wavelength ( $\rho_{L,1} \approx \rho_{L,2}$ ), the ratio of the transmission in the water vapor absorbing channel to that in the non-absorbing channel is equal to the ratio of the corresponding TOA radiance reflectances.

Assuming that atmospheric transmission is multiplicative, one may write  $T^{tot} = T_w^{tot} T_{air}^{tot}$  where  $T_w^{tot}$  is due to water vapor and  $T_{air}^{tot}$  is due to molecular scattering as well as attenuation due to aerosol scattering and absorption. With further assumption that  $T_{air}^{tot}$  is approximately constant across the spectral region covering the two wavelengths used for water vapor retrieval, Eq. (4.5) may be written as

$$T_w^{tot} = \frac{\rho_1^*(\theta_v, \theta_o, \Delta\phi) / \rho_{L,1}}{\rho_2^*(\theta_v, \theta_o, \Delta\phi) / \rho_{L,2}} \quad (4.6)$$

An important aspect of this retrieval technique is that when the surface BRDF is spectrally flat ( $\rho_{L,1} \approx \rho_{L,2}$ ), the water vapor retrieval is independent of the surface BRDF. The solid line in Figure 4.2 depicts simulated two-channel TOA reflectance ratios (absorption channel divided by window channel) as a function of precipitable water for clear sky conditions. A weakness of this retrieval is that the amount of atmospheric haze is unknown. Therefore, the use of clear-sky generated LUTs leads to incorrect water vapor retrieval amounts. The ratios for the low visibility haze cases depicted are less than the clear sky ratios for all three channels shown in Figure 4.2.



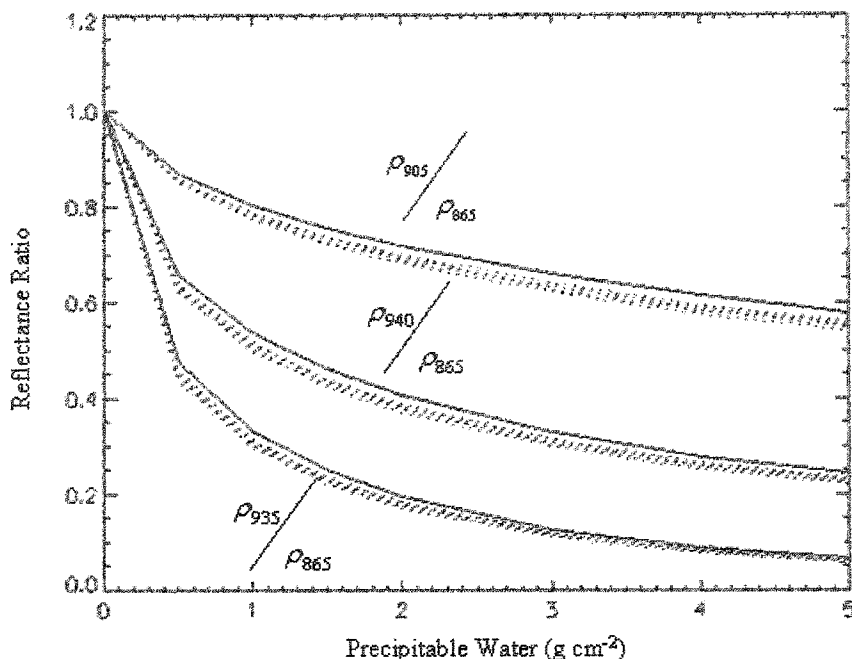


**Figure 4.2:** Gao method of reflectance ratio vs. precipitable water. The ratio of the reflectance in the water vapor channel to that in a nonabsorbing channel (865 nm) for clear sky, and hazy conditions as a function of total precipitable water in the atmosphere. Ratios depicted are at a weakly absorbing water vapor channel (905 nm), a moderately-absorbing water vapor channel (940 nm), and a strongly-absorbing water vapor channel (935 nm). The solid line is for a clear sky case; the others are for visibilities of 10, 8, 5, 3, and 2 km. These calculations were done for a surface albedo = 0.5, a sensor looking at nadir, and a solar zenith angle of 45 degrees.

For cases in which the surface reflectance varies linearly with wavelength, an empirical expression for  $T_w^{tot}$ , based on three channels, one in the water vapor absorption band, and the two others in window regions at 865 and 1240 nm, has been developed (Gao and Kaufman, 2003). According to this empirical expression, the transmittance in the absorbing channel at 945 nm may be written as:

$$T_w^{tot} = \frac{\rho_1^*(\theta_v, \theta_o, \Delta\phi)}{C_1 \rho_2^*(\theta_v, \theta_o, \Delta\phi) + C_2 \rho_3^*(\theta_v, \theta_o, \Delta\phi)} \quad (4.7)$$

where the empirical coefficients are  $C_1 = 0.8$  and  $C_2 = 0.2$ . According to *Gao and Kaufman* (2003) the denominator in Eq (4.7) is the estimated 945 nm TOA reflectance in the absence of water vapor absorption based on the two atmospheric window channels centered at 865 and 1240 nm through linear interpolation. The same assumptions were invoked to arrive at Eq. (4.7) as those used to derive (4.6). For the MODIS sensor both the two and three channel ratioing techniques in Eqs. (4.6) and (4.7) are used to derive the atmospheric transmission of water vapor absorption channels. For this purpose radiances from the five MODIS channels centered at 865, 905, 935, 940, and 1240 nm are used to derive water vapor transmittances at 905, 935, and 940 nm, which are inverted to yield water vapor amounts. Because the three channels have very different absorption coefficients, they have different sensitivities to water vapor and will yield different column amounts for a given atmospheric condition. The band at 935 nm with strong absorption is most sensitive under dry atmospheric conditions, while channel at 905 nm with the weaker absorption is most sensitive under humid atmospheric conditions. Therefore, a weighted average of the three retrieved values is used to represent the total column water vapor amount, and retrievals are obtained over clear areas as well as ocean areas which possess sun glint.

Based on Eqs. (4.6) and (4.7) an atmospheric transmittance code (LOWTRAN7 (*Kneizys et al.*, 1988), MODTRAN (*Berk et al.*, 1989; *Anderson et al.*, 2000), or a line-by-line code such as FASCOD (*Clough et al.*, 1986)) can be used to generate Look Up Tables (LUTs) for  $T_w^{tot}$  as a function of the sun/sensor geometry. Figure 4.2 provides examples of two channel ratios (the absorbing channel divided by window channel) as a function of total column water vapor for a specific sun/sensor geometry. The MODIS NIR water vapor algorithm searches transmittance LUTs generated by radiative transfer simulations to infer  $T_w^{tot}$  which is then used to retrieve the total water vapor amount

accounting for the appropriate sun/sensor geometry. Sensitivity studies have shown that for MODIS an error of 0.01 in the transmittances derived from using the ratio techniques based on Eq (4.6) and (4.7) above implies a 2.5% error in the retrieved column water vapor amount (*Gao and Kaufman, 1998*).

The effect of haze on remote sensing of water vapor depends upon the aerosol optical depth and the magnitude of the surface reflectance. Under 'non-hazy' atmospheric conditions, with visibilities of 20 km or greater, the impact of aerosols on water vapor retrievals is expected to be insignificant for land surfaces with reflectances between 0.2 and 0.4 in the 0.8 -1.3  $\mu\text{m}$  spectral range. This is due to the self-compensation between the aerosol absorption and scattering effects (*Fraser and Kaufman, 1985*). However under hazy conditions (visibility less than 10 km) or when the surface reflectance near 1  $\mu\text{m}$  is small (less than 0.10), errors can be 10% or slightly greater in the MODIS-retrieved water vapor amounts based upon an atmospheric transmission model with no correction for aerosol effects (*Gao and Kaufman, 2003*).

For level two processing of water vapor a module aimed at correcting for aerosol effects has been developed and implemented in the MODIS retrieval algorithm. This correction uses scaling factors that are derived from aerosol optical depths and lookup table procedures. The scaling factors are then applied to the water vapor images to produce a final aerosol-corrected water vapor image. Two pre-calculated lookup tables are used to generate the scaling factors using apparent reflectance at 865 and 940 nm. These LUTs are generated using DISORT (*Stamnes et al., 1988*) with k-distribution coefficients as input, in order to properly account for water vapor absorption.

The aerosol-corrected water vapor amounts are retrieved on a pixel-by-pixel basis using the Near-IR technique described above. The method presented below based upon shadows does not work on a pixel-by-pixel basis, and therefore is not a replacement for the MODIS technique. Rather that presented is a method for retrieving water vapor using shadowed regions, which removes the effects of haze on the radiation field and thereby improves the accuracy of the retrieval.

## 4.2 Description of the Shadow Algorithm

### 4.2.1 Basic Equations

The approximations leading to Eqs. (4.6) and (4.7) ignore the term  $I_{\lambda,diff}(\theta_v, \theta_o, \Delta\phi)$  in Eq. (4.1). This term represents diffuse or scattered radiation due to light scattering by molecules and particles in the atmosphere and reflection by the underlying surface. Under hazy atmospheric conditions this scattered light is a significant component of the total TOA upward radiation field. Thus, leaving out this term leads to errors under hazy atmospheric conditions as mentioned above.

To use shadowed regions to improve the accuracy of water vapor retrievals under hazy atmospheric conditions one must take a closer look at the term  $I_{\lambda,diff}(\theta_v, \theta_o, \Delta\phi)$  in Eq. (4.1). Assuming that the surface is a Lambert reflector and that plane-parallel geometry applies, one then has (see e.g. *Thomas and Stamnes*, 1999, p. 205)

$$\rho_{\lambda,tot}(\theta_v, \theta_o, \Delta\phi) = \rho_{\lambda,black}(\theta_v, \theta_o, \Delta\phi) + \frac{T_{\lambda}(\theta_o, 2\pi)\tilde{T}_{\lambda}(\theta_v, 2\pi)\rho_{\lambda,L}}{\pi[1 - \tilde{\rho}_{\lambda}\rho_{\lambda,L}]} \quad (4.8)$$

where  $\rho_{\lambda,black}(\theta_v, \theta_o, \Delta\phi)$  is the contribution from the atmosphere for a black surface ( $\rho_{\lambda,L} = 0$ ), and the second term is the additional contribution due to the presence of the surface. The quantities appearing in the second term of Eq. (4.8) may be interpreted as follows:

$T_{\lambda}(\theta_o, 2\pi)$  = the total (direct + diffuse) transmitted radiance in direction  $\theta_o$  for uniform illumination of the atmosphere from above;

$\tilde{T}_{\lambda}(\theta_o, 2\pi)$  = the total (direct + diffuse) transmitted radiance in direction  $\theta_v$  for uniform illumination of the atmosphere from below;

$\tilde{\rho}_\lambda$  = the spherical albedo of the atmosphere for uniform illumination of the the atmosphere from below.

If the visibility is high ( $\tilde{\rho}_\lambda \ll 1$ ) or the surface albedo is low ( $\rho_{\lambda,L} \ll 1$ ), Eq. (4.8) becomes

$$\rho_{\lambda,tot}(\theta_v, \theta_o, \Delta\phi) = \rho_{\lambda,black}(\theta_v, \theta_o, \Delta\phi) + \frac{T_\lambda(\theta_o, 2\pi)\tilde{T}_\lambda(\theta_v, 2\pi)\rho_{\lambda,L}}{\pi} \quad (4.9)$$

Before proceeding, the following observations are noteworthy. Firstly, the first term on the right hand side (RHS) of Eq. (4.8) is due entirely to scattering in the atmosphere. Secondly, noting the formal similarity between the second term in Eq. (4.9) [containing total transmittances], and the RHS of Eq. (4.3) [containing direct transmittances]. Thirdly, whereas the direct transmittance in [Eq. (4.3)] is the same for illumination (in the same direction) from above and below, the total transmittances are different [ $\tilde{T}_\lambda(\theta, 2\pi) \neq T_\lambda(\theta, 2\pi)$ ] unless the atmosphere is homogeneous. Fourthly, the enhancement of the surface contribution to the TOA radiance due to the factor  $[1 - \tilde{\rho}_\lambda \rho_{\lambda,L}]^{-1}$  in Eq. (4.8) is caused by multiple reflections between the surface and the atmosphere (primarily the aerosol layer). This enhancement becomes important when the aerosol layer is sufficiently thick ( $0 \ll \tilde{\rho}_\lambda < 1$ ) and the surface reflectance is sufficiently large ( $0 \ll \rho_{\lambda,L} < 1$ ). Finally, noting for completeness that the apparent reflectance defined in Eq. (4.4) is obtained by simply multiplying Eq. (4.8) by  $\pi$ . Thus, the total apparent reflectance becomes

$$\rho_{\lambda,tot}^*(\theta_v, \theta_o, \Delta\phi) = \pi \rho_{\lambda,black}(\theta_v, \theta_o, \Delta\phi) + \frac{T_\lambda(\theta_o, 2\pi)\tilde{T}_\lambda(\theta_v, 2\pi)\rho_{\lambda,L}}{[1 - \tilde{\rho}_\lambda \rho_{\lambda,L}]} \quad (4.10)$$

### 4.2.2 Derivation of the Shadow Algorithm

Figure 4.3 depicts the shadowed and non-shadowed regions which will be considered in these derivations. It should be noted that Eq. (4.10) provides a complete description of the TOA radiance that will be measured by a downward-looking sensor deployed in space when the following assumptions are valid: (i) the atmosphere-surface system can be adequately represented by a vertically inhomogeneous slab of scattering and absorbing molecules and particles over a flat, homogenous surface; (ii) the surface reflects radiation isotropically (Lambert reflector). Thus, so-called “adjacency effects” associated with departure from horizontal homogeneity invoked in the above two assumptions are neglected. Nevertheless, Eq. (4.10) is expected to be very useful for exploring the effects of atmospheric scattering by aerosol particles and reflection by the underlying surface, which are ignored in Eq (4.4). Thus, one assumes that Eq. (4.10) provides an adequate expression for the apparent TOA radiance reflectance under non-shadowed hazy atmospheric conditions.

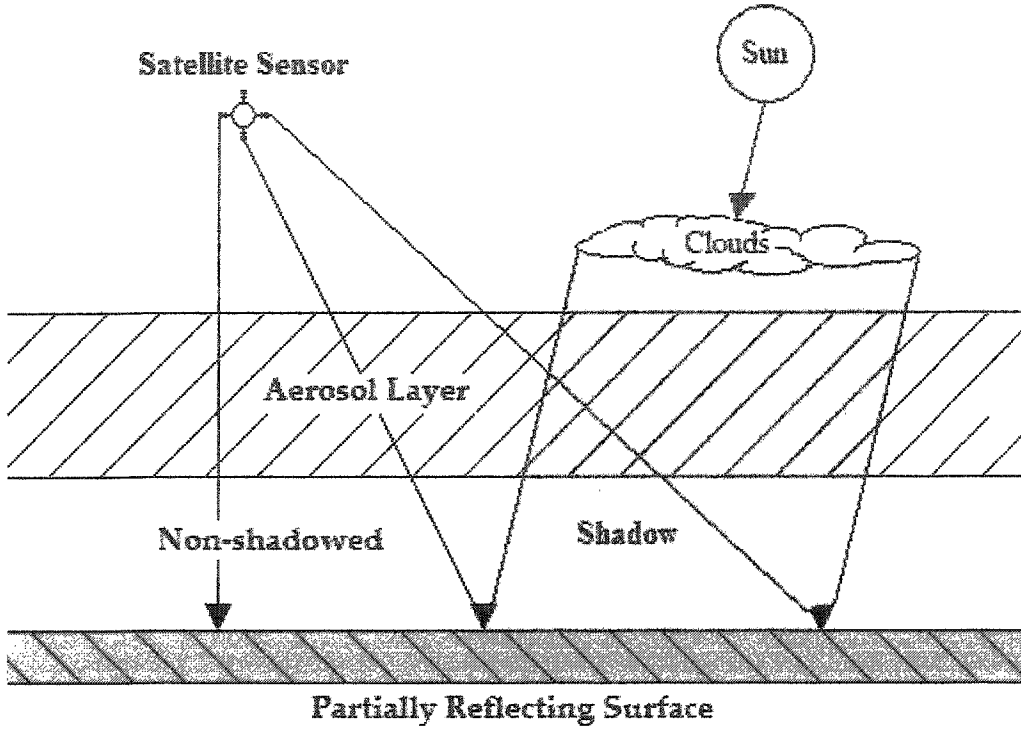


**Figure 4.3:** Conceptual illustration of the shadow method.

Since the total reflectance is the sum of the direct and diffuse part,  
 $T_\lambda(\theta_o, 2\pi) = T_\lambda(\theta_o, 2\pi) + t_\lambda(\theta_o, 2\pi) \equiv T_\lambda + t_\lambda$ , one may rewrite Eq (4.10) as (omitting the angular dependence):

$$\begin{aligned} \rho_{\lambda,tot}^* &= \pi\rho_{\lambda,black} + \frac{(T_\lambda + t_\lambda)(\tilde{T}_\lambda + \tilde{t}_\lambda)\rho_{\lambda,L}}{[1 - \tilde{\rho}_\lambda\rho_{\lambda,L}]} \\ &= \pi\rho_{\lambda,black} + \frac{(T_\lambda\tilde{T}_\lambda + t_\lambda\tilde{T}_\lambda + T_\lambda\tilde{t}_\lambda + t_\lambda\tilde{t}_\lambda)\rho_{\lambda,L}}{[1 - \tilde{\rho}_\lambda\rho_{\lambda,L}]} \end{aligned} \quad (4.11)$$

For shadowed regions, caused for example by a cloud of finite horizontal extent, one assumes that the two terms in the above equation proportional to the direct downward transmittance  $T_\lambda$ , are negligible. Thus, one obtains

$$\rho_{\lambda,tot}^{*,SH} = \pi\rho_{\lambda,black} + \frac{(t_\lambda \tilde{T}_\lambda + t_\lambda \tilde{t}_\lambda)\rho_{\lambda,L}}{[1 - \tilde{\rho}_\lambda \rho_{\lambda,L}]} \quad (4.12)$$

Subtracting the apparent radiance in the shadowed region [Eq. (4.12)], from that in the non-shadowed region [Eq. (4.11)], one finds

$$\Delta\rho_\lambda^* \equiv \rho_{\lambda,tot}^* - \rho_{\lambda,tot}^{*,SH} = \frac{(T_\lambda \tilde{T}_\lambda + T_\lambda \tilde{t}_\lambda)\rho_{\lambda,L}}{[1 - \tilde{\rho}_\lambda \rho_{\lambda,L}]} \equiv T_{eff,\lambda} \rho_{eff,\lambda} \quad (4.13)$$

where

$$T_{eff,\lambda} \equiv T_\lambda \tilde{T}_\lambda + T_\lambda \tilde{t}_\lambda \quad \text{and} \quad \rho_{eff,\lambda} \equiv \frac{\rho_{\lambda,L}}{[1 - \tilde{\rho}_\lambda \rho_{\lambda,L}]} \quad (4.14)$$

One has assumed that the atmospheric contribution  $\rho_{\lambda,black}$  is the same in both regions, and that the surface reflectance is also the same. Note that the subtraction has eliminated the term due to scattered radiation in the atmosphere ( $\rho_{\lambda,black}$ ) and the term proportional to the downward scattered transmission or “skyshine” radiance [Eq. (4.12)], because they are approximately the same for both shadowed and un-shadowed regions. The calculation in Eq. (4.13) above is done for both the band inside the water vapor absorbing region (945 nm called band 1) and the band outside the absorption region (865 nm or band 2). Also, the same surface reflectance and sun/sensor geometry are assumed



to exist in each band. Then by taking the ratio of the two TOA reflectance  $\Delta\rho_\lambda^*$  in the water vapor absorbing band and the non-absorbing band 2, one finds

$$\frac{\Delta\rho_1^* / \rho_{eff,1}}{\Delta\rho_2^* / \rho_{eff,2}} = \frac{T_{eff,1}}{T_{eff,2}} \quad (4.15)$$

which is of the same form as Eq. (4.5). Equation (4.15) shows that when the surface reflectance is constant with wavelength, the ratio of the transmission in the water vapor absorbing channel to that in the non-absorbing channel is equal to the ratio of the TOA reflectance differences. The non-absorbing (window) channel transmission,  $T_{eff,2}$ , can be accurately computed. Unlike the calculations which led to Eq. (4.5) the radiation due to aerosol scattering and surface reflection have been properly included in this calculation.

Assuming that atmospheric transmission is multiplicative, one may write  $T_{eff} = T_w^{tot} T_{air}^{tot}$ , where  $T_w^{tot}$  is due to water vapor and  $T_{air}^{tot}$  is due to molecular scattering as well as attenuation due to aerosol scattering and absorption. If one further assume that  $T_{air}^{tot}$  is approximately constant across the spectral region covering the two wavelengths used for the water vapor retrieval, Eq. (4.15) may be written as

$$T_w^{tot} \approx \frac{\Delta\rho_1^* / \rho_{eff,1}}{\Delta\rho_2^* / \rho_{eff,2}} = \frac{\Delta\rho_1^*}{\Delta\rho_2^*} \quad (4.16)$$

where in the final step one has assumed that the surface reflectance is independent of wavelength.

An important aspect of this shadow differencing water vapor retrieval method is that for uniform spectral reflectance the water vapor retrieval is independent of the surface reflectance. In addition, this method takes into account all contributions to the radiance under hazy atmospheric conditions. Thus, it represents an improvement of the heritage water vapor retrieval technique relying on Eq. (4.5), which ignored aerosol scattering.

### 4.2.3 Simulations and Comparisons

In Figure 4.4 is shown a plot of simulated ratios of TOA reflectance differences between non-shadowed and shadowed regions under hazy atmospheric conditions as a function of the total column water vapor amount.

All three reflectance ratios in Figure 4.4 show little difference between the clear sky cases and the low visibility cases for atmospheric water vapor amounts above  $3 \text{ g/cm}^2$ . Unlike the analogous Figure 4.2, under hazy atmospheric conditions the ratios are typically both smaller in magnitude and greater than the clear sky ratios, for total precipitable  $\text{H}_2\text{O}$  greater than  $0.05 \text{ g/cm}^2$ . To compare the shadow approach (Figure 4.4) to the Gao approach (Figure 4.2) the differences between the clear and hazy atmosphere ratios (transmission differences) for the Gao and shadow approaches are illustrated in Figure 4.5 and Figure 4.6 respectively.

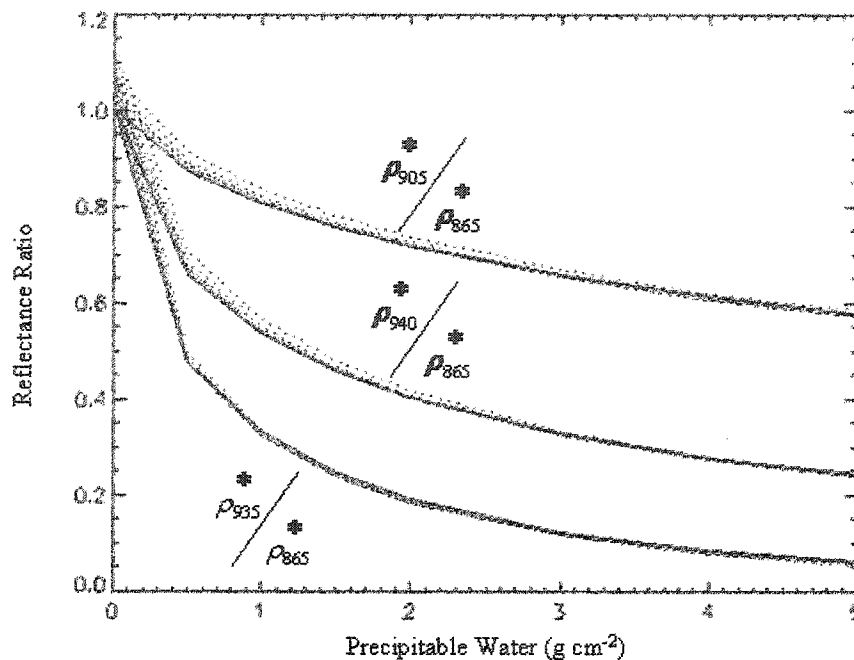


**Figure 4.4:** Shadow method of reflectance ratio vs. precipitable water. The ratio of the reflectance difference in the water vapor band to that in a nonabsorbing channel (865 nm) as a function of total precipitable water in the atmosphere [Eq.(4.15)] for clear sky, and hazy conditions. Ratios depicted are the clear minus shadow ratios at a weakly absorbing water vapor channel (905 nm), a moderately-absorbing water vapor channel (940 nm), and a strongly-absorbing water vapor channel (935 nm). The solid line is for a clear sky case, whereas the others are for visibilities of 10, 8, 5, 3, and 2 km. These calculations were done for a surface albedo = 0.5, a sensor looking at nadir, and a solar zenith angle of 45 degrees.

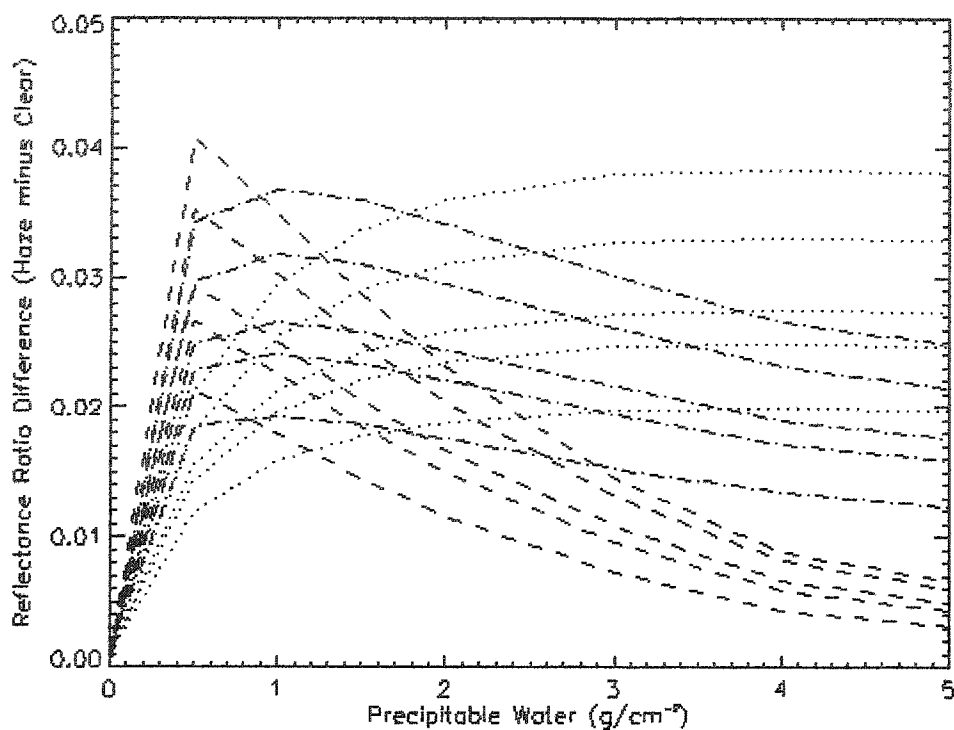


**Figure 4.5:** Gao method reflectance ratio haze and clear sky difference. Difference in reflectance ratio (or transmission) of the haze cases minus the clear ratio cases depicted in Figure 4.2 (Gao approach) The five ratio difference lines depicted are for visibilities of 10, 8, 5, 3, and 2 km. The dotted lines are the differences between the clear and the hazy conditions for the reflectance ratio 905 nm/865 nm, the dashed lines are for the reflectance ratio 940 nm/865 nm, and the dash-dot lines are for the reflectance ratio 935 nm/865 nm.

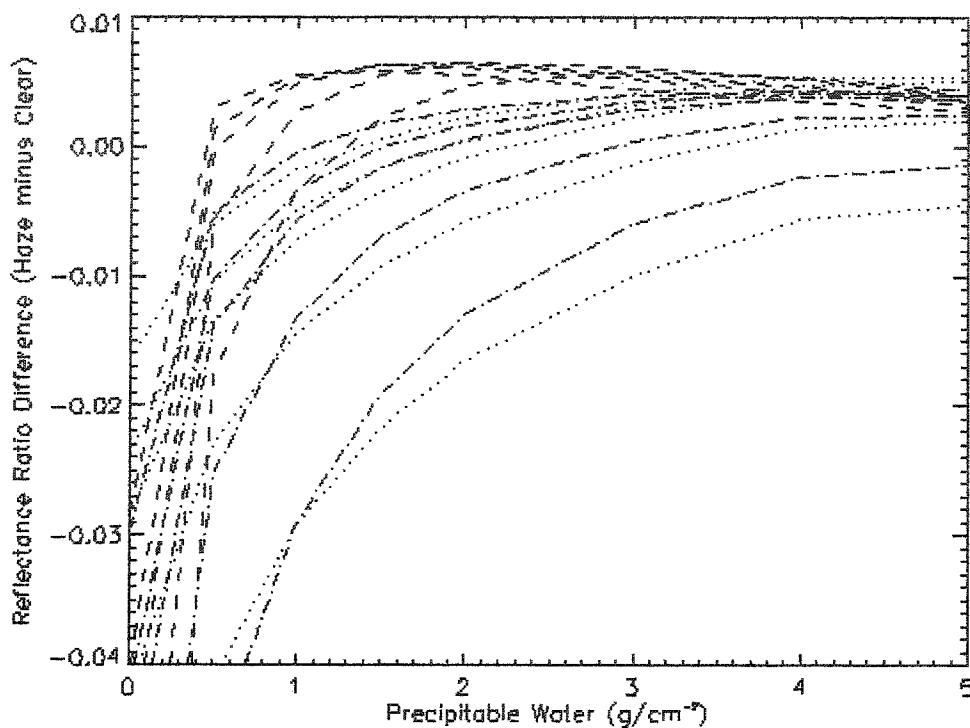


**Figure 4.6:** Shadow method reflectance ratio haze and clear sky difference. Difference in reflectance ratio (or transmission) of the haze cases minus the clear ratio cases depicted in Figure 4.4 (shadow approach). The five ratio difference lines depicted are for visibilities of 10, 8, 5, 3, and 2 km. The dotted lines are the differences between the clear and hazy conditions for the reflectance ratio 905 nm/865 nm, the dashed lines are for the reflectance ratio 940 nm/865 nm, and the dash-dot lines are for the reflectance ratio 935 nm/865 nm.

From Figure 4.5, which illustrates the Gao approach, one may note that the difference between the clear and low visibility haze conditions is up to 0.04 when the total column water vapor in the atmosphere larger than  $0.5 \text{ g/cm}^2$ . Previous research has shown that a 0.01 difference in the reflectance ratio contributes a 2.5% error in water vapor estimation, which leads to a 10% error under low visibility conditions (*Gao and Kaufman, 1998*). This 10% error is illustrated by the 0.04 differences in Figure 4.5 for the hazy cases. Figure 4.6 illustrates that for the shadow approach, the magnitude of the difference between the clear and low visibility haze conditions is 0.01 – 0.02 for total column water vapor amounts larger than  $0.5 \text{ g/cm}^2$ . This is roughly half to a quarter of

the difference resulting from the Gao approach. This would lead to a 2.5% - 5.0% error under low visibility conditions. It is worth noting that with the shadow approach for visibilities down to 5 km the error is less than 2.5%, and for visibilities less than 3 km the errors go up to 5%, whereas for the Gao approach an error of 5% - 10% exists for all visibilities. For low total column water vapor amounts less than  $0.5 \text{ g/cm}^2$  the differences between the clear and lower visibility hazy atmospheres are greater with the shadow method than with the Gao approach. This is because haze is still included in the direct transmission curves, and its effect is suppressed in the Gao approach because errors in the upward radiance are present in both the numerator and denominator of the ratios. Overall though for typical water vapor amounts and low visibilities the shadow approach has less error.

### 4.3 Practical Considerations

The aerosol-corrected water vapor amounts are retrieved on a pixel-by-pixel for MODIS basis by the Near-IR Gao approach. The method presented here based on the use of shadows does not work on a pixel-by-pixel basis, and therefore is not a replacement for the MODIS technique. Rather that which is presented is a method for retrieving water vapor using shadowed regions, which by subtraction effectively removes the effects of haze and thereby improves the accuracy of the retrieval. In order for the shadow approach to be applied however, the detection of shadows and hazy atmospheric regions is necessary. The MODIS team has developed algorithms which do both.

To use shadows for water vapor retrievals, the presence of shadows need to be detected in the imagery. The detection of shadows is a problem that has not been adequately addressed in the literature. For clear sky scenes shadowed regions may theoretically be computed given the sensor viewing geometry, solar azimuth and zenith angles, cloud/object edges distribution, and cloud/object top altitude. This approach, however, is computationally intensive, and the height of clouds/objects is generally not

available to all sensors. For shadow detection, a simple reflectance thresholding shadow detection algorithm has been developed by the MODIS team. The shadow detection is performed operationally for the MODIS sensor, being output as a pixel level flag in the MODIS Cloud Mask (*Ackerman et al.*, 1997). This algorithm checks for shadows whenever a highly confident clear scene has been detected. The shadow detection is based upon TOA reflectance at 0.95, 0.87, and 0.65  $\mu\text{m}$ . A shadow is identified when  $R_{0.95} < 0.12$  and  $R_{0.87}/R_{0.65} > 0.9$  (*King et al.*, 1998). This shadow detection has exhibited good performance over vegetated surface regions. Regions are identified as vegetated by the ecosystem type based on geographical location.

In addition to detecting shadowed regions MODIS team has developed simple algorithms to detect if an atmosphere is heavily laden with aerosols. These tests were developed to detect if a region has a thick haze layer which might be misinterpreted as a cloud. This information is available as an output from the cloud detection algorithms for developed for MODIS (*Ackerman et al.*, 1997). The tests were developed to be conservative so that thin aerosol layers are often flagged as clear (*King et al.*, 1998). The technique for the detection of hazy atmospheres is based upon the observation that the reflectance at 2.1  $\mu\text{m}$  is largely unaffected by heavy aerosol loadings and can be used to detect aerosols over dark surface targets, such as vegetation. Using observed correlations between surface reflectances at 0.66  $\mu\text{m}$  and 2.1  $\mu\text{m}$  it was found that the reflectance at 0.66  $\mu\text{m}$  may be well approximated as half of the reflectance at 2.1  $\mu\text{m}$  (*Kaufman et al.*, 1997). If the  $R_{2.1}$  is larger than 0.2 then no haze is detected because the haze detection algorithm works only over dark surfaces. When  $R_{2.1} < 0.2$  and  $R_{0.66} > (0.04 + R_{2.1})$  then a hazy atmosphere is detected.

For sensors with higher spatial resolution, such as LANDSAT and IKONOS, which possess 15 m and 1-4 m resolution respectively, shadowed regions will occur more frequently in the imagery, and less of a mixture between shadowed and non-shadowed pixels will be present. Thus, the shadow method presented here can be used to improve the accuracy of the Gao approach under high haze conditions.

#### 4.4 Conclusions

A method has been developed to augment current state-of-the-art total column water vapor retrievals. It is based on the use of ratios of reflectances within and outside the Near-IR water vapor absorption band. This new method, called the 'shadow' method, improves water vapor retrievals under hazy atmospheric conditions by employing radiance differences between non-shadowed and shadowed regions. The improvement in water vapor retrieval, achievable by application of the shadow method, is obtained by considering all contributions to the reflected radiance in the derivation of the total water vapor amounts. By comparison the heritage water vapor retrieval method is based on approximations that are avoided in the shadow method. A complete derivation of the shadow method has been provided, and supporting radiative transfer simulations have been carried out to demonstrate its merit. These simulations show that under hazy atmospheric conditions, and for typical column water vapor amounts, the shadow method can be used to infer total water vapor amounts with a 2.5% error, while, the heritage method yields an error up to 10% in total water vapor amount.



## Chapter 5

### Methane Detection from Space: Use of Sun Glint

#### 5.0 Introduction

Methane seepage is indicative of petroleum or natural gas reserves. Techniques aimed at detecting methane seepage with surface based instrumentation have progressed significantly in recent years. These instruments rely upon measurement of light attenuation due to methane absorption of Short Wave Infrared (SWIR) radiation. Detection of methane seepage over water bodies with electro-optical remote sensing has been limited due to the low surface reflectance of water. Also, due to sensor saturation, imagery over sun glint is commonly discarded in satellite remote sensing, because the glint conditions produce high surface reflectance. However, recent measurements in the SWIR of sun glint regions have revealed that the surface reflectance is spectrally flat and enhanced without causing saturation. This higher surface reflectance in sun glint regions allow for retrieval of total column methane amount using ratios of measured radiances at wavelengths inside and outside of methane absorbing SWIR channels. The methane retrieval method presented here, based on short wave infrared ratios in sun glint regions, allows for detection of methane seepage over the Earth's oceans and lakes, and the detection of possible petroleum or natural gas reserves. Radiative transfer simulations are used to demonstrate the capabilities offered by this technique. This chapter has been submitted for publication (*Larsen and Stamnes, 2005b*).

Methane is a colorless and odorless gas which since the pre-industrial era has steadily increased in the atmosphere, more than doubling in concentration in the last two to three hundred years (*Rasmussen and Khalil, 1984*). Much of the increase in methane is caused by human activity. *Safley et al. (1992)* reported that the atmospheric concentration of methane is currently about 1.7 ppm and increasing at a rate of 1% per

year. Methane is a greenhouse gas, second in importance to carbon dioxide as a global warming agent. Methane absorbs infrared radiation, converting radiation emitted by the Earth to heat, rather than allowing it to escape to space. There is significantly less methane in the atmosphere, compared to carbon dioxide, but one molecule of methane traps approximately 30 times as much radiant energy as does one molecule of carbon dioxide. The global warming due to atmospheric methane increase is approximately half that due to carbon dioxide (*Dickinson and Cicerone, 1986; Ramanathan et al., 1985*). Continued increase in atmospheric methane of 1% a year is believed to be likely to contribute more to climate change than any other gas except carbon dioxide (*Cicerone and Oremland, 1988*).

The primary source of atmospheric methane is due to the microbial decay of organic matter under anoxic conditions in wetlands. Compared to the natural methane emissions, anthropogenic sources are twice as large and includes contributions due to rice cultivation, bacterial decay in landfills, sewage, leakage due to the mining of fossil fuels, leakage from natural gas pipelines, and biomass burning.

## **5.1 Overview and Background**

### **5.1.1 Methane Sources**

The occurrence of hydrocarbon seeps at the Earth's surface indicates that there is leakage from a hydrocarbon reservoir. These hydrocarbon seep gases are composed of 80 – 90% methane (*Hornafius, 1999*). Seeps play an important role in the exploration of new natural gas basins or petroleum producing regions. Petroleum exploration began with the search for oil that flowed from surface rocks. Petroleum seeps leaking from subsurface reservoirs recorded have been recorded as far back as 3000 B. C. (*Tedesco, 1995*), and Drake's historic well near Titusville, Pennsylvania was drilled on the basis of a seep in the adjacent creek bed. The importance of seeps has been minimized in an era

of increased use of sophisticated instrumentation, and decreased use of ground surveys. Nearly all important oil-producing regions of the world were first discovered by surface oil and gas seeps (*Hunt, 1981*). These seeps can be active, macroseepage, in which there is commonly oil and gas seepage which is visible to the human eye. Or they may be passive, microseepage, in which there are temporarily elevated concentrations of analytically detectable volatile or semi volatile hydrocarbons, or hydrocarbon-induced changes, in soils and sediments overlying a petroleum accumulation. (*Link, 1952*) was the first to separate macroseeps from microseeps, which can only be detectable by geochemical means. By the 1920's nearly all of the visible macroseeps had been drilled (*Tedesco, 1995*). Microseeps are usually detectable only by sensitive instruments, or by the visible result of their effect on the near-surface environment. These microseeps, although perhaps not as obvious or dramatic as macroseeps, are just as valuable for the exploration of undiscovered reserves.

### **5.1.2 Ground-based Methane Remote Sensing Techniques**

Hydrocarbons generated and trapped beneath the seafloor seep to the surface in varying but detectable quantities. These phenomena occur because processes and mechanisms such as diffusion, effusion, and buoyancy allow hydrocarbons to escape from reservoirs and migrate to the surface where they may be retained in the sediments and soils or diffuse into the atmosphere or water columns (*Klusman, 1993; Schumacher and Abrams, 1996*). Based upon these assumptions, various techniques have been developed to identify the surface or near surface occurrences of hydrocarbons. Surface geochemical prospecting for hydrocarbons consists of direct and indirect methods to identify hydrocarbon seepage. For environmental and economic reasons, future petroleum exploration needs to be both non-invasive and cost-effective. Remote sensing can allow for continuous sampling, without the need for permits or direct access to rough

and hostile environments, and allow large areas to be explored rapidly. For these reasons remote sensing is increasingly being used for exploration.

Remote sensing for hydrocarbons has typically focused on the identification of indirect evidence of its presence, such as by the identification of minerals associated with seeps, the detection of seeps based on spectral signatures of stressed vegetation (Everett *et al.*, 2002; Yang *et al.*, 1998), and the identification of favorable petroleum reservoir structures (Halbouty, 1976). Additional research has resulted in the development of approaches based on microwave techniques (Gournay *et al.*, 1979; Thompson, 1981) and surface based laser systems. Laser systems have been built to measure numerous atmospheric species coincident with seeps. The more recent systems have been developed to measure primarily methane and ethane in the atmosphere for petroleum exploration by detecting microseeps, and for monitoring leaks in gas pipelines.

A newer technique being employed for remote sensing of seeps is Light Detection and Ranging (LIDAR). LIDAR uses light from a tunable laser to selectively detect methane and heavier gases by their absorption (Grant and Menzies, 1983). A LIDAR pulses light into the atmosphere where aerosols, liquid droplets, and gaseous molecules scatter and absorb the light. Methane absorption features commonly used for LIDAR instruments are in the SWIR and MidWave-InfraRed (MWIR) spectral regions, located near 1650, 2200, and 3200 nm. A LIDAR works because some of the scattered light is backscattered to the sensor and measured. The length of time between transmission and reception indicates from what distance the light was backscattered and the light intensity indicates the concentration of the gas encountered. These LIDARs are commonly truck or airborne mounted systems which are capable of range resolving the location and concentrations of atmospheric gas clouds. In addition, surface methane detection has been used to identify gas leaks from buried, above ground, and underwater pipelines. These LIDARS have been used as a cost-effective way to detect macroseeps and microseeps in unexplored regions. Methane surface seepage concentrations have

been measured at 50-60 ppm over pavement with broken underground gas pipes beneath (SRI Int., 2004), at 100 ppm range over seepage regions on the surface of the ocean (Ophir Corp., 2003), and at a broad range of surface concentrations, from 6-910 ppm (McLaren et al., 2001).

The final method used in remote sensing of seeps is one which analyzes the condensate carbon traces on aerosols carried by the atmosphere in thermals (Barringer, 1981). Gas bubbles in seeps diffuse to the water surface where a fraction of them emerge into the overlying atmosphere and give rise to aerosols through gas-to-particle conversion processes. These aerosols are collected from large volumes of air by an airborne cyclone sampler carried on board an aircraft which is typically flown at 30 m. Subsequently these aerosols are examined by a flame ionization detector for hydrocarbon content.

### 5.1.3 Satellite Remote Sensing Potential

Methane is emitted in large amounts from the bottom sediments on the sea floor, and is released in the seawater, where it is partly oxidized and consumed by bacterial activity. Nevertheless, appreciable amounts of methane are released to the atmosphere at the sea surface. Methane from high-intensity seeps that vigorously eject methane into the water column is likely to reach the upper part of the water column and to have a pronounced effect on atmospheric composition.

Recently spaceborne sensors using gas correlation spectroscopy, such as the Measurements of Pollution in the Troposphere (MOPITT) sensor, have been deployed to measure total column amounts of methane. However this sensor has coarse spatial resolution of 22 km at nadir and its use is primarily for studying environmental change, rather than for petroleum research.

Some satellite-borne sensors avoid using data in regions of sun glint, e.g., Sea-viewing Wide Field-of-view Sensor (SEA WIFS), because no useful retrievals were

envisaged during its design and due to sensor saturation problems (*Gatebe et al.*, 2005). However, it has been demonstrated that the sun glint in the near-infrared spectral region may be useful for aerosol absorption (*Kaufman et al.*, 2002) and for the retrieval of precipitable water vapor amounts (*Kleidman et al.*, 2000). Additionally, one may use sun glint for the retrieval of surface methane amounts using the SWIR spectral region.

Use of methane features in the SWIR spectral region for retrieval of atmospheric methane amounts over water bodies from spaceborne sensors is limited by the low surface reflectance of water across this spectral region (approximately 0.02) which is an order of magnitude lower than the reflectance due to sun glint. This low reflectance is due to absorption by water of the radiation that survives atmospheric attenuation, leading to little reflected light reaching the Top of Atmosphere (TOA). However, under conditions of sun glint the surface reflectance increases significantly, allowing more radiance to reach the sensor, despite the methane absorption. In remote sensing imagery sun glint regions possess high reflectance, which is also spectrally flat across the SWIR spectral region. Recent measurements with the Cloud Absorption Radiometer (CAR) instrument, (*King et al.*, 1986), over sun glint regions have demonstrated high uniform surface reflectance in the SWIR spectral region (*Gatebe et al.*, 2002).

#### 5.1.4 Sun Glint Features

The diameter of a sun glint region observed by a satellite at an altitude of 800 km often exceeds 100 km, and the reflectance of this spot is greater than 0.2 (*Hagolle et al.*, 2004). The region of the sun glint depends mainly on the geometrical conditions and on the ocean surface roughness, which is controlled mainly by wind speed. Sun glint patterns are much wider when the surface winds are strong and the solar zenith angle is large, which favors an elliptical shape elongated towards the horizon accompanied by a broader reflectance peak. Small solar zenith angles ( $\theta_0 < 20^\circ$ ) seem to favor a circular sun glint pattern and a relatively smaller peak, (*Gatebe et al.*, 2005). Other researchers

(*Cox and Munk, 1954a; Cox and Munk, 1954b*) pointed out that the width of the glint pattern is an indication of the maximum slope of the sea surface. A calm flat mirror-like ocean has a much higher reflectance in the specular direction than a windswept ocean. However, the principal effect of an agitated sea is to reflect the direct solar beam into a range of angles; the rougher the sea the wider the range (*Su et al., 2002*). The overall effect of this is that the range of angles from which a sensor may observe the sun glint is wider. Sun glint may occur when the reflected sun angle, i.e., the angle  $\theta_r$  between the sun direction and satellite direction lies between  $0^\circ$  and  $36^\circ$ . This angle is determined by the cosine law of spherical geometry (as illustrated in Figure 5.1):

$$\cos(\theta_r) = \sin(\theta_v) \sin(\theta_o) \cos(\Delta\phi) + \cos(\theta_v) \cos(\theta_o) \quad (5.1)$$

where  $\theta_o$  is the solar zenith angle,  $\theta_v$  is the sensor viewing zenith angle, and  $\Delta\phi$  is the difference between the sun and sensor azimuthal angles (*Ackerman et al., 1997*).

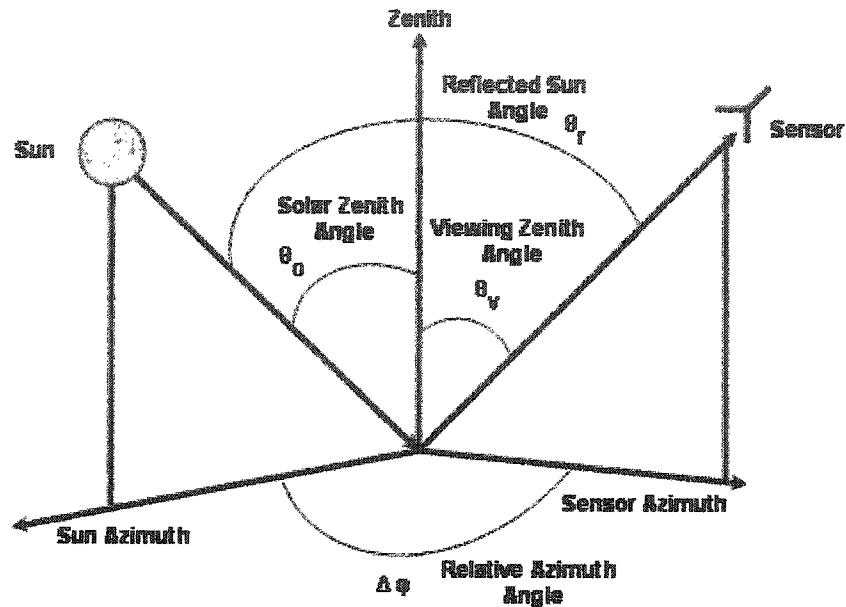


**Figure 5.1:** Solar and viewing angles definition.

The overall effect of higher wind speeds is to cause a region of sun glint to decrease in size and to be less uniform. With winds of speeds greater than 7 m/s, white caps usually appear on the ocean (Koepeke, 1984). These white caps can affect surface reflectance in sun glint regions, and are to be avoided to have the uniform spatial and spectral reflectance in the SWIR across the regions of sun glint. Recently, Hagolle et al. (2004) simulated this uniform SWIR spectral reflectance, which agrees with spaceborne measurements, over sun glint regions for a variety of wind speeds. These simulations of spectrally uniform SWIR surface reflectance ranged from 0.55 for 2 m/s winds to 0.15 for 7 m/s winds. Additionally, measurements taken with the CAR instrument at 10 m



resolution have identified spectrally uniform SWIR reflectance across sun glint regions within this range (*Gatebe et al.*, 2005). For simulations, a uniform SWIR reflectance of 0.15 and 0.55 have been used as estimates of surface reflectance in the sun glint region. Additionally, the technique presented should be applied only over oligotrophic open ocean regions to limit additional uncertainties which might occur in the uniformities in surface reflectance from shallow nutrient and sediment laden littoral water regions.

One may envision this method being used as a survey tool to explore large areas for microseeps. Once microseeps are detected, then more advanced and sophisticated exploration tools such as 3-D seismic surveys could be applied to the more promising seepage areas. An important aspect of this approach is that it directly detects the natural resource of interest. This is in contrast to many other geochemical or spectral techniques (e.g. hyperspectral imaging) in which the measurements represent direct evidence of subsurface accumulation.

Retrieving of methane in sun glint region is possible by using technologies developed for retrieving water vapor amount in the 1980's and 1990's. This approach employs backscattered Near-InfraRed (NIR) solar radiance near 1000 nm for the retrieval of water vapor amounts, and has been further developed into an operational tool for total water vapor retrieval (*Gao et al.*, 2003), which is currently used to retrieve the total column water vapor amount from the Moderate Resolution Imaging Spectroradiometer (MODIS) (*Salomonson et al.*, 1989) deployed on the NASA Terra and Aqua spacecraft platforms. An inherent limitation to this technique is that under hazy atmospheric conditions (with visibilities less than 10 km), or when surface reflectance near 1000 nm is small, the derived amounts in total column water vapor may be off by as much as 10% if aerosol effects are not properly corrected for (*Gao and Kaufman*, 1998). To compensate for the atmospheric aerosol effects, an aerosol correction module was developed which employs Look Up Tables (LUTs) generated from radiative transfer simulations based on DISORT (*Stamnes et al.*, 1988). The

method developed for methane retrieval employs the TOA reflectance ratios technique developed by (Gao *et al.*, 2003), but rather than using water vapor absorption regions in the NIR, use is made of the methane absorption features in the SWIR located near 2200 nm. In the SWIR region scattering effects due to atmospheric aerosols are minimal (King, 1998), however simulations have shown that under low visibility atmospheric conditions that the error due to haze is non-negligible in methane retrieval.

## 5.2 Description of the Algorithm

As was previously stated, the SWIR technique for column methane retrieval is based on measured TOA radiances within the methane absorption band, using the SWIR region located near 2200 nm, depicted in Figure 5.2. This figure, and all the other computations reported on in this paper are based on MODTRAN (Berk *et al.*, 1989; Anderson *et al.*, 2000). The horizontal lines in Figure 5.2 illustrate the bandwidth of the window region centered at 2125 nm, and the three absorption regions centered at 2225, 2275, and 2325 nm. The window centered at 2125 nm is apparent by the lower solid line plot being zero throughout a significant wavelength region of this window. Likewise the other three absorption bands are nonzero, indicating stronger methane absorption with increasing wavelength. The spectral range between 2150 and 2200 nm was not considered because absorption features due to both weak methane and water vapor absorption occur across this spectral range. Wavelength regions beyond 2350 nm were not considered due to water vapor absorption as well. The retrieval of total column methane is based on the use of reflected radiances within the methane absorption bands and in channels just outside the bands. The radiance within the absorption band measured by the satellite-deployed sensor is due to sunlight that has been attenuated by atmospheric methane absorption along its path from the TOA to the surface, and after reflection by the surface, attenuated once more along its path from the surface to the entrance aperture of the sensor. Radiation in a nearby window region outside the

methane absorption bands follows similar radiometric paths except that it is not subject to methane absorption.

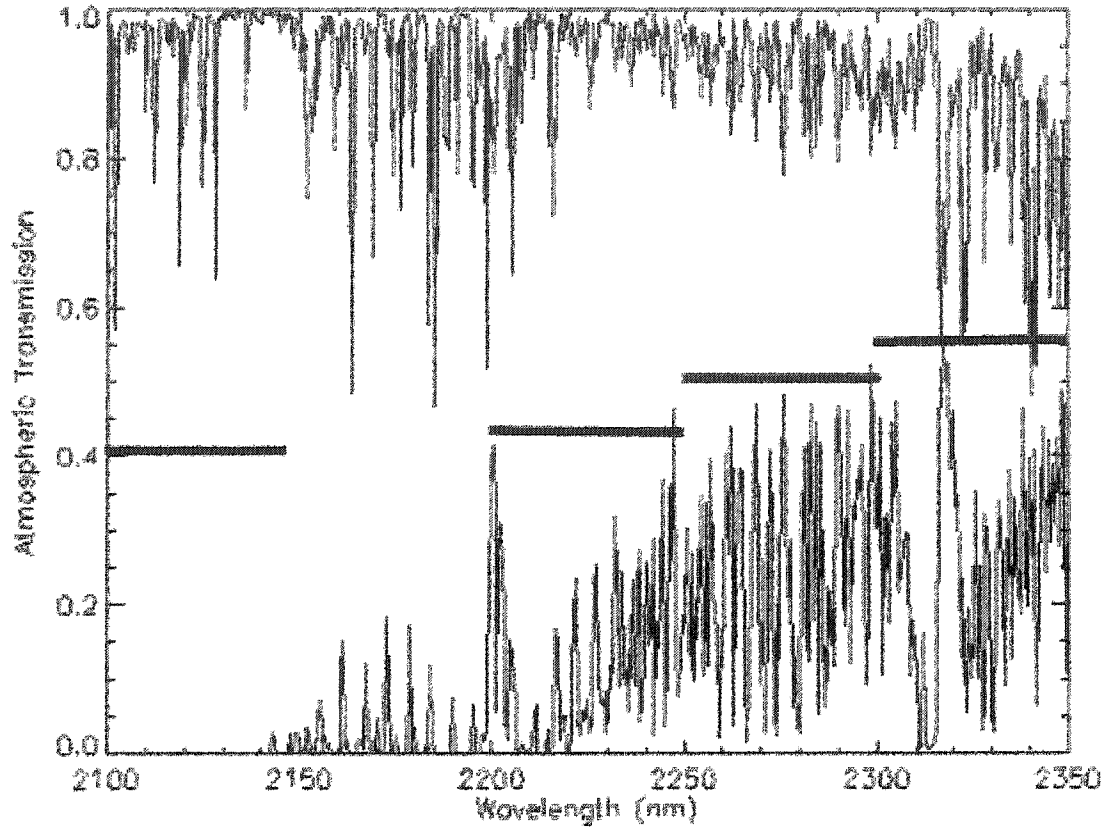


**Figure 5.2:** SWIR atmospheric transmission 2100 - 2350 nm. Upper solid line is for the total atmospheric transmission of the standard atmosphere with 1.7 ppm methane. Lower solid line is the transmission difference between the upper line and the same atmosphere with 1000 ppm surface methane. The straight solid lines from left to right are the bands considered in simulations, the window region centered at 2125, and absorption regions centered at 2225, 2275, and 2325 nm.

The monochromatic radiance at wavelength  $\lambda$  measured by a downward looking spaceborne sensor can be approximated as (*Hansen and Travis, 1974; Thomas and Stamnes, 1999*):

$$I_{\lambda}(\theta_v, \theta_o, \Delta\phi) = I_{\lambda, \text{diff}}(\theta_v, \theta_o, \Delta\phi) + \frac{\mu_o F_{o\lambda}}{\pi} T_{\lambda}(\theta_o) T_{\lambda}(\theta_v) \rho_{\lambda}(\theta_v, \theta_o, \Delta\phi) \quad (5.2)$$

where  $F_{o\lambda}$  is the extraterrestrial solar irradiance (normal to the solar beam),  $\theta_o$  is the solar zenith angle,  $\mu_o = \cos\theta_o$ ,  $\theta_v$  is the sensor viewing angle, and  $\Delta\phi$  is the difference in azimuth between the sun and the sensor. The amount of attenuated sunlight striking the surface in direction  $\theta_o$  that is reflected in direction  $(\theta_v, \Delta\phi)$  of the sensor is described by  $\rho_\lambda(\theta_v, \theta_o, \Delta\phi)$ , the bidirectional reflection distribution function (BRDF). The second term in Eq. (5.2) is due to radiance that is directly transmitted through the atmosphere, first in the downward direction described by the direct transmittance  $T_\lambda(\theta_o)$ , and then (after reflection by the surface) in the upward direction towards the sensor described by the direct transmittance  $T_\lambda(\theta_v)$ . This term can be evaluated by atmospheric transmittance codes such as LOWTRAN (Kneizys *et al.*, 1988), FASCODE (Clough *et al.*, 1986) based upon tabulated methane absorption cross sections (available for example in the HITRAN database (Rothman *et al.*, 1998)) provided the BRDF,  $\rho_\lambda(\theta_v, \theta_o, \Delta\phi)$ , is known.

The diffuse or scattered radiation due to multiple scattering is described by the first term  $I_{\lambda,diff}(\theta_v, \theta_o, \Delta\phi)$ , which is much more problematic because it involves scattering by atmospheric aerosols whose optical properties, including absorption and scattering coefficients and optical depth (depending on mass loading), are poorly known. In fact, these optical properties are known to vary considerably in space and time. Moreover, they depend on the chemical composition of the aerosol particles as well as their increase in size and resulting change in the index of refraction due to uptake of water in response to increased humidity which in turn depends on the atmospheric water vapor content (Shettle and Fenn, 1976; Tsay and Stephens, 1990; Yan *et al.*, 2002). Finally this term also depends on the surface BRDF,  $\rho_\lambda(\theta_v, \theta_o, \Delta\phi)$ .

Nevertheless, in high visibility situations (low aerosol loading), it may be justifiable to ignore this term due to scattering and absorption by aerosols as well as the radiance contribution due to scattering by molecules (Rayleigh scattering) which are

both small in the SWIR spectral range. Then, if one invokes the customary assumption that the surface is a Lambertian reflector so that the BRDF is isotropic, i.e.,

$\rho_\lambda(\theta_v, \theta_o, \Delta\phi) \equiv \rho_{\lambda,L}$ , Eq. (5.2) reduces to (Fraser and Kaufman, 1985; Gao and Kaufman, 2003)

$$I_\lambda(\theta_v, \theta_o, \Delta\phi) = \frac{\mu_o F_{o\lambda}}{\pi} T_\lambda(\theta_o) T_\lambda(\theta_v) \rho_{\lambda,L} \quad (5.3)$$

The methane absorption features in the 2200 nm SWIR spectral region are attractive for retrievals of methane over sun glint regions because the surface reflectance,  $\rho_{\lambda,L}$ , is constant with wavelength across both the absorption region and the nearby window region used for retrieval. Also, for this methane retrieval algorithm to be reliable the surface reflectance must be greater than 0.1, which is true for sun glint regions across the SWIR spectral region (Hagolle *et al.*, 2004).

If one divides Eq. (5.3) by the incident irradiance,  $\mu_o F_{o\lambda}$ , one obtains the (radiance) reflectance, defined as:

$$\rho_\lambda(\theta_v, \theta_o, \Delta\phi) \equiv \frac{I_\lambda(\theta_v, \theta_o, \Delta\phi)}{\mu_o F_{o\lambda}} = \frac{T_\lambda(\theta_o) T_\lambda(\theta_v) \rho_{\lambda,L}}{\pi} \quad (5.4)$$

and if one then multiplies by  $\pi$  one obtains the *apparent* (radiance) reflectance, defined as:

$$\rho_\lambda^*(\theta_v, \theta_o, \Delta\phi) = \pi \rho_\lambda(\theta_v, \theta_o, \Delta\phi) = T_\lambda(\theta_o) T_\lambda(\theta_v) \rho_{\lambda,L} \equiv T_\lambda^{tot}(\theta_v, \theta_o) \rho_{\lambda,L} \quad (5.5)$$

In which the total transmittance is defined,  $T_\lambda^{tot}(\theta_v, \theta_o) \equiv T_\lambda(\theta_o) T_\lambda(\theta_v)$ , as the product of the downward direct and upward direct transmittances. Applying Eq. (5.5) to the

methane absorption band (denoted by subscript 1) as well as the nearby window region (denoted by subscript 2), and taking the ratio one finds:

$$\frac{T_1^{tot}(\theta_v, \theta_o)}{T_2^{tot}(\theta_v, \theta_o)} = \frac{\rho_1^*(\theta_v, \theta_o, \Delta\phi) / \rho_{L,1}}{\rho_2^*(\theta_v, \theta_o, \Delta\phi) / \rho_{L,2}} \quad (5.6)$$

Here one has assumed that the same sun/sensor geometry and surface reflectances apply for both bands. Thus, when the scattered radiation can be ignored, as it can in the SWIR spectral region, Eq. (5.6) shows that if the surface reflectance is independent of wavelength ( $\rho_{L,1} \approx \rho_{L,2}$ ), the ratio of the transmission in the methane absorbing channel to that in a non-absorbing channel is equal to the ratio of the corresponding TOA radiance reflectances.

Assuming that atmospheric transmission is multiplicative, one may write

$T^{tot} = T_M^{tot} T_{air}^{tot}$  where  $T_M^{tot}$  is due to methane and  $T_{air}^{tot}$  is due to molecular scattering as well as attenuation due to aerosol scattering and absorption. If one further assumes that  $T_{air}^{tot}$  is approximately constant across the spectral region covering the two wavelengths used for methane retrieval, Eq. (5.6) may be written as:

$$T_M^{tot} = \frac{\rho_1^*(\theta_v, \theta_o, \Delta\phi) / \rho_{L,1}}{\rho_2^*(\theta_v, \theta_o, \Delta\phi) / \rho_{L,2}} \quad (5.7)$$

An important aspect of this retrieval technique is that when the surface BRDF is spectrally flat ( $\rho_{L,1} \approx \rho_{L,2}$ ) as it is in regions of sun glint (Hagolle *et al.*, 2004), the methane retrieval is independent of the surface BRDF. The solid line in Figure 5.3 depicts simulated two-channel TOA SWIR reflectance ratios (absorption channel

divided by window channel) around 2200 nm as a function of total methane for clear sky conditions. A limitation of the heritage water vapor retrieval method (*Gao et al.*, 2003), which the present methane retrieval method builds upon, is the possible impact of haze on the retrieval. When the amount of atmospheric haze is unknown there are errors introduced into the retrievals. Therefore, for the heritage ratio retrieval algorithms, the use of clear-sky generated LUTs may lead to incorrect retrieval amounts under low visibility conditions. To assess the sensitivities of total column methane retrievals to haze, simulations with low visibility will be considered in addition to clear atmospheric conditions.

### 5.3 Radiative Transfer Simulations

Figures 5.3 and 5.4 depict simulations of the TOA reflectance ratios of absorption band to window region about 2200 nm. They were done for surface methane amounts between a 1.7 ppm normal concentration level and a 1000 ppm, in the first 3 m above the surface, and 1.7 ppm above this thin methane layer. These simulations were done over sun glint regions with a surface reflectance of 0.15 and 0.55, for varying visibilities, and at high and medium solar/sensor viewing zenith angles. In addition to the 2200 nm methane features being studied for retrievals, the methane features near 1650 nm were also considered. However the 1650 nm absorption features were found to be far weaker than those in the 2200 nm region. Extensive simulations in the 1650 nm region revealed no significant change in the TOA reflectance ratios with increasing surface methane concentrations, and therefore no sensitivity to methane in this spectral region.

Figures 5.3 and 5.4 depict the ratios of the three methane absorption bands and the window region depicted in Figure 5.2 for two different sun glint reflectance-values (0.15 and 0.55), different atmospheric visibilities, and varying surface methane amounts,

between 1.75 and 1000 ppm, in the first 3 m above the surface. The most significant difference between Fig 5.3 and 5.4 is the differences in the sun/sensor viewing zenith angles, from roughly  $40^\circ$  to  $75^\circ$  for both the sun and sensor angles. The simulated reflectance ratio decreases with total column methane amount for all three of the ratios. Thus, these ratios can be used to generate Look Up Tables (LUT) for retrieval of total column methane amounts. There are no significant differences between the ratios for different surface reflectance-values, which illustrates their versatility for application under a variety of surface reflectance regimes in the glint region due to varying surface wind speeds. For the increasing path lengths caused by the  $75^\circ$  sun/sensor view angles in Figure 5.4 compared to roughly  $40^\circ$  in Figure 5.3, all of the three ratios are decreased in reflectance ratio values, and the rate of decline of reflectance ratios with increasing surface methane amounts is greater. This is indicative of the increased methane retrieval capabilities due to longer path lengths resulting from larger solar/sensor zenith angles in the sun glint region.

The lower visibility cases, those less than 10 km, introduce the greatest problems in retrieving the total column methane amount. In simulations, the methane is assumed to be located just above the surface, while the haze responsible for the lower visibilities is assumed to be located above the methane layer. This haze will backscatter radiation to the satellite sensor before it encounters the surface methane layer, which leads to an increase in the radiance at the entrance aperture of the sensor accompanied by a depression of the ratios for low visibility cases as illustrated in Figures 5.3 and 5.4. The effect of haze upon the methane retrievals is to decrease the ratios, which will lead to the retrieved methane column amounts retrieved to be higher than they should be, because under clear sky conditions a lower ratio corresponds to a higher total column methane amount. The impact of haze is therefore an important issue, as it is for the heritage NIR water vapor retrieval techniques. Thus, for the low visibility situations the haze effect would need to be quantified and removed. The greatest differences, aside from the hazy atmospheric conditions, between Figures 5.3 and 5.4 are the different path lengths due to



different viewing geometries. Thus, in the absence of haze the LUTs should be generated for varying sun/sensor zenith angles, and varying surface methane amounts. Minimal sensitivity to surface reflectance (in the absence of haze) implies that it can be ignored in the generation of LUTs. Since the typical amount of methane is 1.7 ppm in the absence of a seep, one may look at sun glint regions under typical conditions to decide if haze effects are sufficiently large to warrant consideration.

The only modification in the methane atmospheric profiles used in the simulations is in the first 3 m above the surface, leaving the rest of the atmospheric methane profile unchanged. This allows the rescaling of the horizontal axis of Figure 5.3 to be in ppm methane rather than in total column methane. This rescaling has been done to generate Figure 5.5, which is a plot of the TOA reflectance of the 2325 nm absorbing band and the TOA reflectance of the 2125 nm window band. The ppm rescaling allows the direct retrieval of the surface methane amounts from the LUTs.

In the absence of haze a spectrally flat surface reflectance does not affect the retrieval, as is evident from Eq. 5.7 and the solid lines in Figures 5.3, 5.4, and 5.5. To illustrate the effect of haze on the retrieval two additional cases are included in Figure 5.5 corresponding to visibilities of 10 km and 5 km, respectively, for each of the two surface-reflectance values. For these hazy atmospheric conditions there are significant differences between the reflectance ratios simulated with different surface reflectance values. This is caused by multiple reflections between the surface and haze layer. The higher surface reflectance the stronger this multiple reflection effect, as is evident from the difference between the 0.15 (dashed lines) and the 0.55 (dotted lines) reflectance values depicted in Figure 5.5.

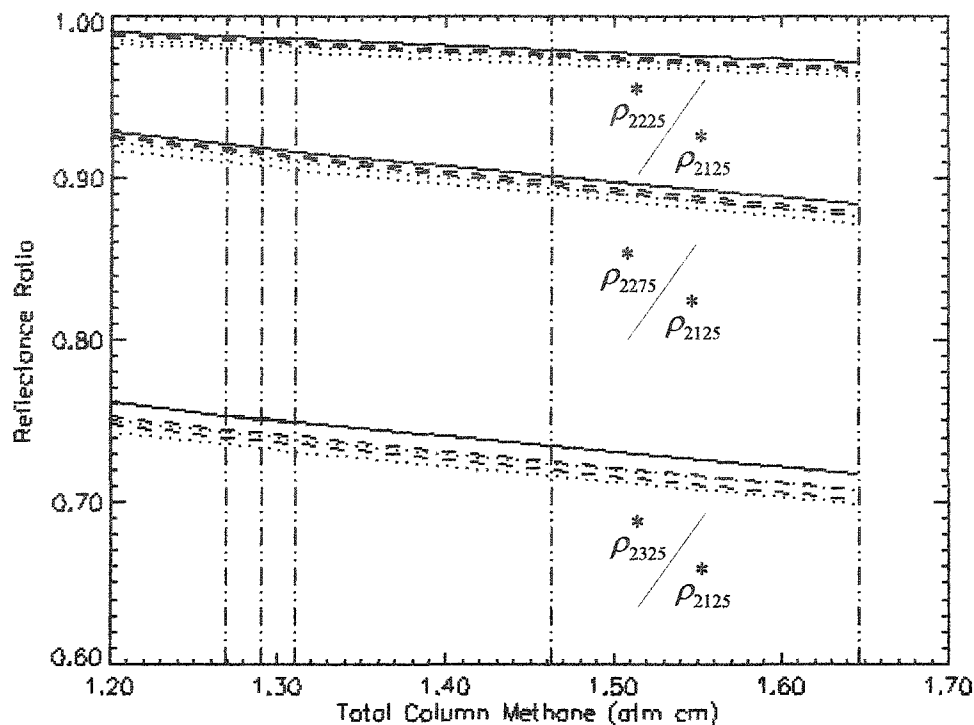


**Figure 5.3:** Reflectance ratios versus total column methane for a short path length. The ratio of the reflectance in the methane absorption channel to that in a nonabsorbing channel (2125 nm) for clear sky, and hazy conditions as a function of total column methane in the atmosphere. Ratios depicted are at a weakly absorbing methane channel (2225 nm), a moderately-absorbing methane channel (2275 nm), and a strongly-absorbing methane channel (2325 nm). The solid line is for a clear sky case; the others are for visibilities of 10 and 5 km. The vertical dash-dot-dot lines are from left to right for a 3 m thick surface layer 1.7, 50, 100, 500, and 1000 ppm in concentration. These calculations were done for a sun glint reflectance of 0.15 and 0.55, and a sun/sensor configuration  $\theta_o = 40^\circ$ ,  $\theta_v = 43.5^\circ$ ,  $\Delta\phi = 174^\circ$ .

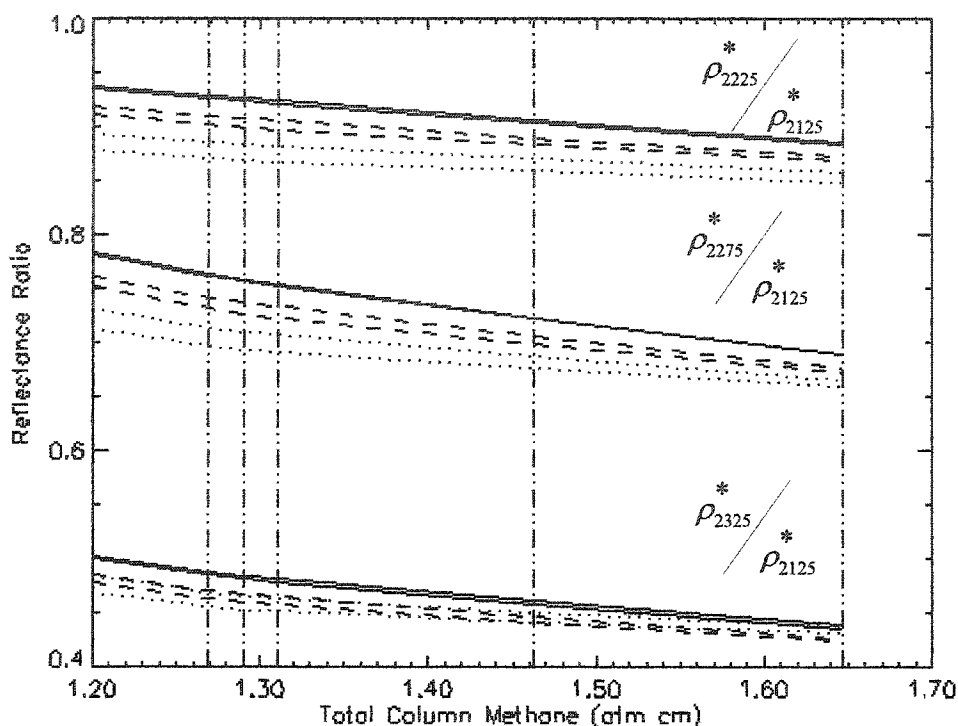


**Figure 5.4:** Reflectance ratios versus total column methane for a long path length. The ratio of the reflectance in the methane absorption channel to that in a nonabsorbing channel (2125 nm) for clear sky, and hazy conditions as a function of total column methane in the atmosphere. Ratios depicted are at a weakly absorbing methane channel (2225 nm), a moderately-absorbing methane channel (2275 nm), and a strongly-absorbing methane channel (2325 nm). The solid line is for a clear sky case; the others are for visibilities of 10 and 5 km. The vertical dash-dot-dot lines are from left to right for a 3 m thick surface layer 1.7, 50, 100, 500, and 1000 ppm in concentration. These calculations were done for a sun glint reflectance of 0.15 and 0.55, and a sun/sensor configuration  $\theta_o = 75^\circ$ ,  $\theta_v = 75^\circ$ ,  $\Delta\phi = 174^\circ$ .

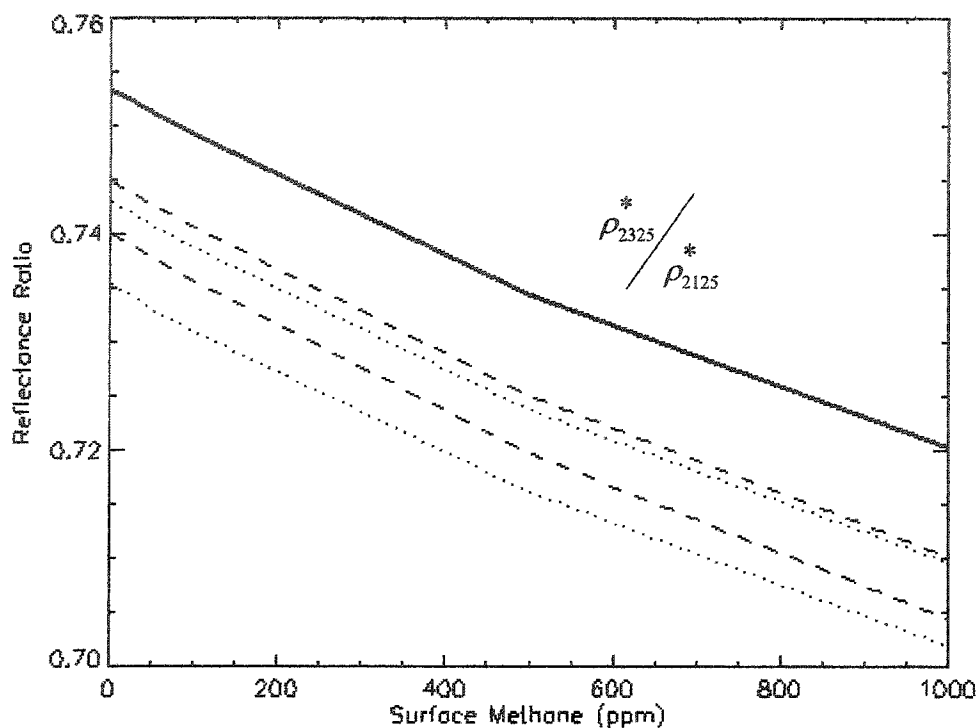


**Figure 5.5:** Reflectance ratios versus surface methane for a short path length. The ratio of the TOA reflectance in the methane absorption channel at 2325 nm to that in the non-absorbing window region 2125 nm for clear sky, and hazy conditions as a function of the methane concentration (in ppm) of a 3 m thick surface layer. The solid line is for a clear sky case; the others are for visibilities of 10, and 5 km. These simulations were done for a sun glint reflectance of 0.15 (dashed lines) and 0.55 (dotted lines), for a sun/sensor viewing configuration  $\theta_o = 40^\circ$ ,  $\theta_v = 43.5^\circ$ ,  $\Delta\phi = 174^\circ$ .

#### 5.4 Practical Considerations

The methane amounts over sun glint regions can be retrieved on a pixel-by-pixel basis using the SWIR technique described above. However the methane retrieval technique is limited in that it can only do retrievals in regions where the sun/sensor geometry and wind speed allow sun glint to occur. Sensors would need to be developed to do glint-looks, in which a sensor looks in specific sun/sensor geometries into likely glint regions over water. To find regions of possible sun glint one may use light at wavelengths shorter than the SWIR, where sun glint leads to saturation of visible and NIR sensors. The method developed here can be used to similarly detect atmospheric amounts of other gaseous species with specific absorption features. Therefore this technique may have applications beyond the retrieval of methane amount.

Clouds are a significant issue for the retrieval of methane in regions of sun glint. The reflectance of clouds across the SWIR spectral region is similar to that of sun glint water regions, in being higher than over non-glint water regions. The clouds however are located at varying heights above the water surface. Thus it would be necessary to do a cloud screening or detection of the sun glint regions to discriminate cloud from glint regions. However, the sun glint reflectance is spectrally flat across the SWIR, whereas there is a decrease in TOA cloud reflectance spectrally from 850 to 1600 to 2200 nm. This can be used to help reject the regions of the sun glint from being used for methane retrievals when clouds are present to eliminate them as an error source.

Atmospheric haze is the most significant issue in using this method for retrieving surface methane amounts. In simulations, it was found that low visibility conditions lead to an overestimation of surface methane amounts unless one corrects for the haze effect. To compensate for the atmospheric aerosol effects in analogous total column water vapor retrieval algorithms an aerosol correction module was developed which employs Look Up Tables (LUTs) generated from radiative transfer. A similar module can be

developed to account for the atmospheric aerosol effects on surface methane retrievals. Methods for aerosol corrections, similar to those developed and used for atmospheric correction of MODIS and SeaWiFS data, could be used to deal with the aerosol correction issues.

## 5.5 Conclusions

A method has been developed to retrieve total column methane amount using a technique similar to that currently employed to retrieve total column water vapor. It is based on the use of ratios of reflectances within and outside the SWIR methane absorption bands. This new method allows for total column methane retrieval under conditions of sun glint from water bodies including oceans, lakes and rivers. A complete derivation of the method has been provided, and supporting radiative transfer simulations have been carried out to demonstrate its merit. These simulations show this retrieval method can be used to infer total methane amounts under clear atmospheric conditions. Under lower visibility hazy atmospheric conditions the effect of the haze must be taken into account in the methane retrieval. Methane amounts over sun glint regions can be retrieved on a pixel-by-pixel basis using this SWIR technique. It is envisioned that this method can be used as a survey tool to explore large areas for microseeps. Once microseeps are detected, then more costly exploration tools such as 3-D seismic surveys could be applied to the most promising source areas. An important aspect of this approach is that it directly detects the natural resource of interest. This is in contrast to many other geochemical or spectral techniques (e.g. hyperspectral imaging) in which the measurements represent direct evidence of subsurface accumulation.

## Chapter 6

### Summary and Discussion

The main contributions of this thesis are summarized as follows:

(1) Cloud detection algorithms constitute an initial step in satellite remote sensing processing. Such algorithms discriminate cloudy from clear regions and enable additional processing to be done upon the discriminated regions. To this end a cloud detection algorithm has been developed for the VIIRS sensor. In the development of the VIIRS cloud detection algorithm the theoretical background required to derive the Environmental Data Requirement (EDR) of the VIIRS Cloud Mask (VCM) was explained. Also, a review of the processing developed for the algorithm was provided, along with necessary data input and outputs. A description of the cloud mask error budget was provided including a flowdown analysis of error sources and their magnitudes. In addition, the accuracy and precision of the binary cloudy/not cloudy flag, generated in this manner, have been studied with both simulated cloud multispectral VIIRS imagery, and with MAS data. The cloud mask developed in Chapter 2 of this thesis is part of the Cloud Cover/Layers EDR required for the National Polar Orbiting Environmental Satellite System (NPOESS)/VIIRS software package of EDRs, to be launched in 2008.

(2) A study has been conducted of the effects of Band-to-Band Mis-Registration (BBM) upon the multi-spectral VIIRS cloud detection algorithm. The BBM occurs in imagery when pixels from multiple bands are not completely co-registered to the same location on the Earth. Because the VIIRS Cloud Mask algorithm employs multiple bands which may be mis-registered, such mis-registration could possibly affect the cloud detection. The study of the sensitivity of the of cloud detection to BBMs is presented Chapter 3. Errors in the VCM leading to misclassifications greater than 10% were found to occur when BBMs exceed 20%. Additionally the BBM was found to affect the clear-

when-cloudy classifications much more than the cloudy-when-clear classifications, by a factor of 7:1, beyond 20% BBM. These studies resulted in a recommendation to the VIIRS sensor developers that BBMs be kept less than 20% in sensor development and design.

Once cloud detection is accomplished, using a multi-spectral algorithm such as the one developed for MODIS or VIIRS, additional algorithms may be used to retrieve other data products. Two new techniques of retrieving atmospheric information, which may be applied to sensors deployed on future satellite remote sensing platforms, have been developed. Both of these new techniques have been developed as part of this thesis. The results and conclusions of these efforts are expanded upon in items 3 and 4 below.

(3) An algorithm has been developed to use cloud shadows to improve upon water vapor retrievals under hazy atmospheric conditions. This method has been developed to augment current state-of-the-art total column water vapor retrievals. It is based on the use of ratios of reflectances within and outside the Near-IR water vapor absorption band. This new method, called the 'shadow' method, improves water vapor retrievals under hazy atmospheric conditions by employing radiance differences between non-shadowed and shadowed regions. The improvement in water vapor retrieval, achievable by application of the shadow method, is obtained by considering all contributions to the reflected radiance in the derivation of the total water vapor amounts. By comparison, the heritage water vapor retrieval method is based on approximations that are avoided in the shadow method. A complete derivation of the shadow method has been provided, and supporting radiative transfer simulations have been carried out to demonstrate its merit. These simulations show that under hazy atmospheric conditions, and for typical column water vapor amounts, the shadow method can be used to infer total water vapor amounts with a 2.5% error, while the heritage method yields an error up to 10% in total water vapor amount.



(4) A method has been developed to retrieve total column methane amount using a technique similar to that currently employed by MODIS to retrieve total column water vapor. This technique is based on the use of ratios of reflectances within and outside the methane absorption bands around 2.2 microns. This new method allows for total column methane retrieval under conditions of sun glint from water bodies including oceans, lakes and rivers. A complete derivation of the method has been provided, and supporting radiative transfer simulations have been carried out to demonstrate its merit. These simulations show that this retrieval method can be used to infer total methane amounts under clear atmospheric conditions. Under lower visibility hazy atmospheric conditions the effect of the haze must be taken into account in the methane retrieval. Methane amounts over sun glint regions can be retrieved on a pixel-by-pixel basis using this technique. It is envisioned that this method can be used as a survey tool to explore large areas for microseeps. Once microseeps are detected, then more costly exploration tools such as 3-D seismic surveys could be applied to the most promising source areas. An important aspect of this approach is that it directly detects the natural resource of interest in contrast to geochemical or spectral techniques (e.g. hyperspectral imaging) in which the measurements represent evidence of subsurface accumulation.

The VIIRS cloud detection algorithm developed in this thesis, with its supporting studies, is part of a future operational satellite system for use globally to assist in monitoring the Earth's environment, and it is a prerequisite for the retrieval of numerous environmental data products. The shadow method can enhance algorithms currently used on operational satellites to retrieve atmospheric trace gas measurements globally under hazy atmospheric conditions. Finally, the methane retrieval method can be applied to previously discarded sun glint imagery data to reduce costly exploration for petroleum resources globally.

## Appendix A

### Ancillary Data of Future Use to VIIRS

In addition to several input data sources described above, other non-VIIRS data that may prove useful for the VCM is summarized in Table A-1. These data are not required by the VCM for operation; however, if they were to be available to the VCM, improvements in the VCM's performance would be expected.

**Table A-1:** Ancillary non-VIIRS data useful for the VCM.

<b>Input data</b>	<b>Source of Data</b>
OMPS radiances	OMPS
OMPS EDRs	OMPS
CRIS radiances	CRIS
CRIS vertical EDRs	CRIS
CMIS radiances	CMIS
CMIS EDRs	CMIS

Radiances from the Ozone Mapping Profiling Suite (OMPS) (*NPOESS IPO*, 1999a) instrument may improve cloud detection. At the time of the writing of this thesis, the bands for the OMPS instrument are as yet To Be Determined (TBD). The OMPS bands will be located in the ultraviolet (UV) spectral region. The use of OMPS bands needs to be investigated to determine their utility in the detection of high Polar Stratospheric Clouds (PSC). The PSC are sub-visual and are not detectable with VIIRS bands. Both the nadir and limb scanning instruments of the OMPS may be useful for cloud detection.

OMPS EDR and Sensor Data Records (SDRs) may be useful for cloud detection in the VCM. The OMPS EDR/SDRs of Total Ozone, Ozone Profile, Tropospheric Ozone, Ozone Profile, and Aerosol Absorptance Index could be used to adjust the thresholds of UV cloud detection techniques reliant upon OMPS UV radiance measurements.

Cross Track Infrared Sounder (CRIS) (*NPOESS IPO*, 1999b) radiance data may be useful for cloud detection in the VCM. These data might be used whenever a CRIS and a VIIRS instrument coexist. The use of the CRIS radiance data (for all three bands), needs to be investigated for the potential to improve cloud detection techniques. The nighttime cloud detection capabilities might benefit most from the CRIS data. MODIS investigations are presently underway with MODIS Airborne Simulator (MAS) data. Richard Frey, at the University of Wisconsin (UW), has in the past used the 13  $\mu\text{m}$  channel in the MODIS Cloud Mask to demonstrate the utility of the radiances in the CRIS channels.

Measurements of vertical temperature, pressure, and water vapor may improve the capabilities of the VCM. These profiles are modified in the presence of a cloud. Knowledge of water vapor profiles may assist in setting cloud detection thresholds for thin cirrus cloud detection tests at 1.375  $\mu\text{m}$ , and other cloud detection tests. Knowledge of the amount of liquid water and ice in the atmosphere may assist cloud phase determination as well.

Use of Conical Scanning Microwave Image/Sounder (CMIS) (*NPOESS IPO*, 2001) radiance data may improve cloud detection capabilities of the VCM, particularly at night. Passive microwave measurements over cloudy areas differ from those over clear regions. The amount of liquid water and ice in the atmosphere may be determined with CMIS data. This would directly assist in cloud detection. The value of atmospheric profiles has been mentioned previously for the CRIS vertical EDRs. Use of CMIS atmospheric profiles may improve cloud detection.

## **Appendix B**

### **Cloud Mask Software Architecture**

This appendix demonstrates the VCM component level software architecture, which deals with the module-level data flows in the context of the VIIRS system data processing chain. Further details on the module-level data flows across the interfaces, both input data and output data, their formats and the relationships which exist between them are provided in the VCM Component Level Software Architecture Document (*Larsen, 2000c*) which forms the basis for the detailed design of the Cloud Mask SDR algorithm code. For a summary of the overall software structure of the VIIRS system the reader is directed to *Kuin (2000)*. Two illustrations in Figure B-1 and B-2 demonstrate the division of the cloud mask into its major software architecture sublevels. These are the cloud mask context level and the component level data flow diagrams.

The context data flow diagram shown in Figure B-1 is the Level 1 data flow diagram for the cloud mask component. It identifies the major data flows, sources and sinks. Sources are considered to be the data input, while sinks are considered to be the data output. The data flows will map to the interfaces named in the Chapter 2. In this Level 1 data flow diagram the cloud mask output is considered an Intermediate Product (IP) to other VIIRS data products.

The component level data flow diagrams are the first level of decomposition of the context level diagram. In the component diagram (Figure B-2) major data flows for the VCM algorithm are broken down into their constituent flows. Further decomposition of the VCM may be done for the individual modules, but the VCM will not be broken down to this level of detail.

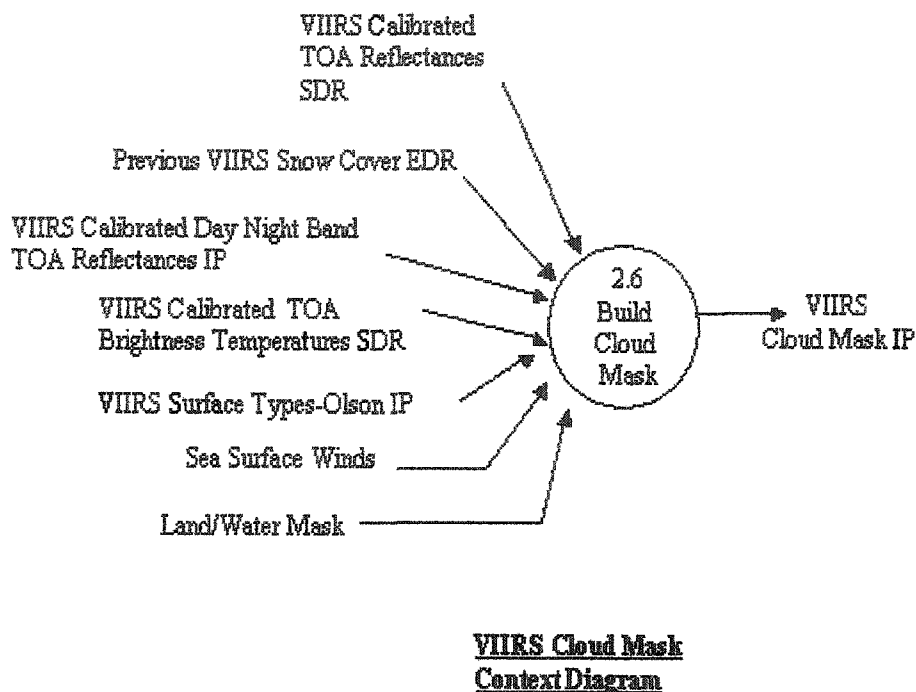


**Figure B-1:** VIIRS Cloud Mask context level data flow diagram.

Similar to the discussion and figures presented earlier in this appendix, the component diagram shows the flow of the VCM algorithm. In addition it contains the data which are transferred from module to module within the VCM. Initially the ancillary data, which have previously been formatted into Supplemental Data Records (SDRs) format, are read into the VCM algorithm. Then the internal arrays of the code are populated with the data which are used by the VCM with a Logical Flag Array (LFA), containing all of the results of the logical decisions arrived at in the cloud detection process. This internal LFA array is updated throughout the VCM code processing, until for every pixel of the VCM the LFA is populated with cloud detection results. The VCM is designed to consider an entire image, moving along the image pixel by pixel. Within each pixel, or context region, a logical sequence of steps is performed. These steps are shown in Figure B-2. Once the cloud detection results are done for an

image the output is packed into an SDR output file. The structure of this output file is shown in Chapter 2.

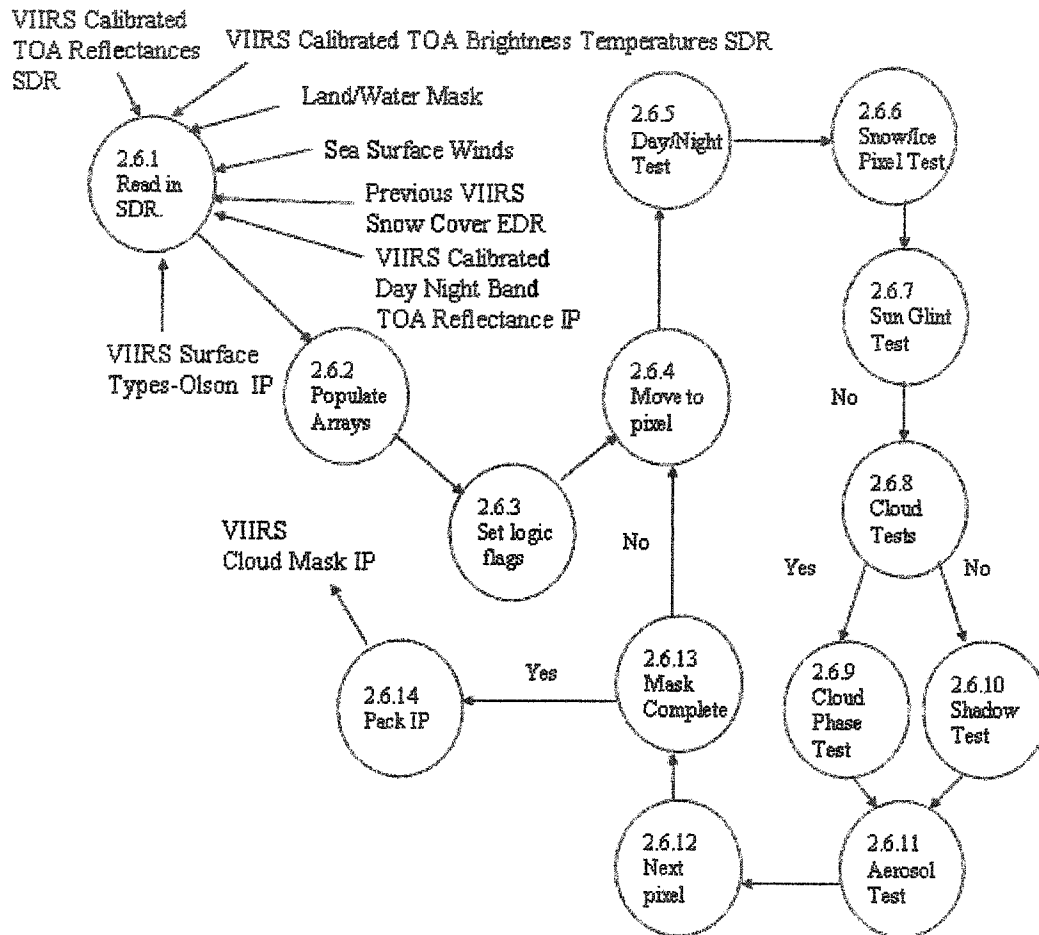


**Figure B-2:** VIIRS Cloud Mask component level data flow diagram.

## Appendix C

### The VIIRS Cloud Phase Product

The VIIRS Cloud Phase (VCP) product is developed from a hybrid of the MODIS, AVHRR, and Geostationary Operational Environmental Satellite (GOES) Cloud Phase detection techniques. In being a hybrid algorithm, it utilizes the best cloud phase determination features from all of these cloud phase assessment techniques. The overall processing structure is a direct result of a modularized flow which is expected to decrease both necessary processing time and efficiently determine cloud phase.

Generation of the cloud phase occurs routinely within the VCM as part of the first level of EDR processing. The cloud phase pixel level results are then used at a pixel level by the other cloud EDRs. The results of the cloud phase algorithm will define the pixel as containing a cloud which is predominantly liquid water, ice, or undetermined. Figure C-1 illustrates the VCP algorithm and a discussion follows.

The first pre-processing step, which is depicted in the VCP algorithm, in Figure C-1, is the determination by the VCM of a presence of a cloud. For clear pixels, the VCP algorithm will not be executed. In addition to the pixel being detected as cloudy, knowledge of the underlying surface type, sun/sensor geometry, if the pixel is in the day or night regime, and the reflectances and BTs of bands used by the VCP are required as input.

Following the indication by the VCM of a cloud's presence in the pixel region the first three thresholding tests are the confident indicators of cloud particle phase. If a pixel's cloud phase is indicated by one of these first three tests then its phase will not be changed as a result of tests which are performed later in the VCP algorithm. Only those pixels whose phase is undetermined by the first three tests will be considered by tests done afterwards in the VCP algorithm. These first three tests are the R1.38, BT11, and visible/NIR reflectance thresholding tests. These tests are as follows:

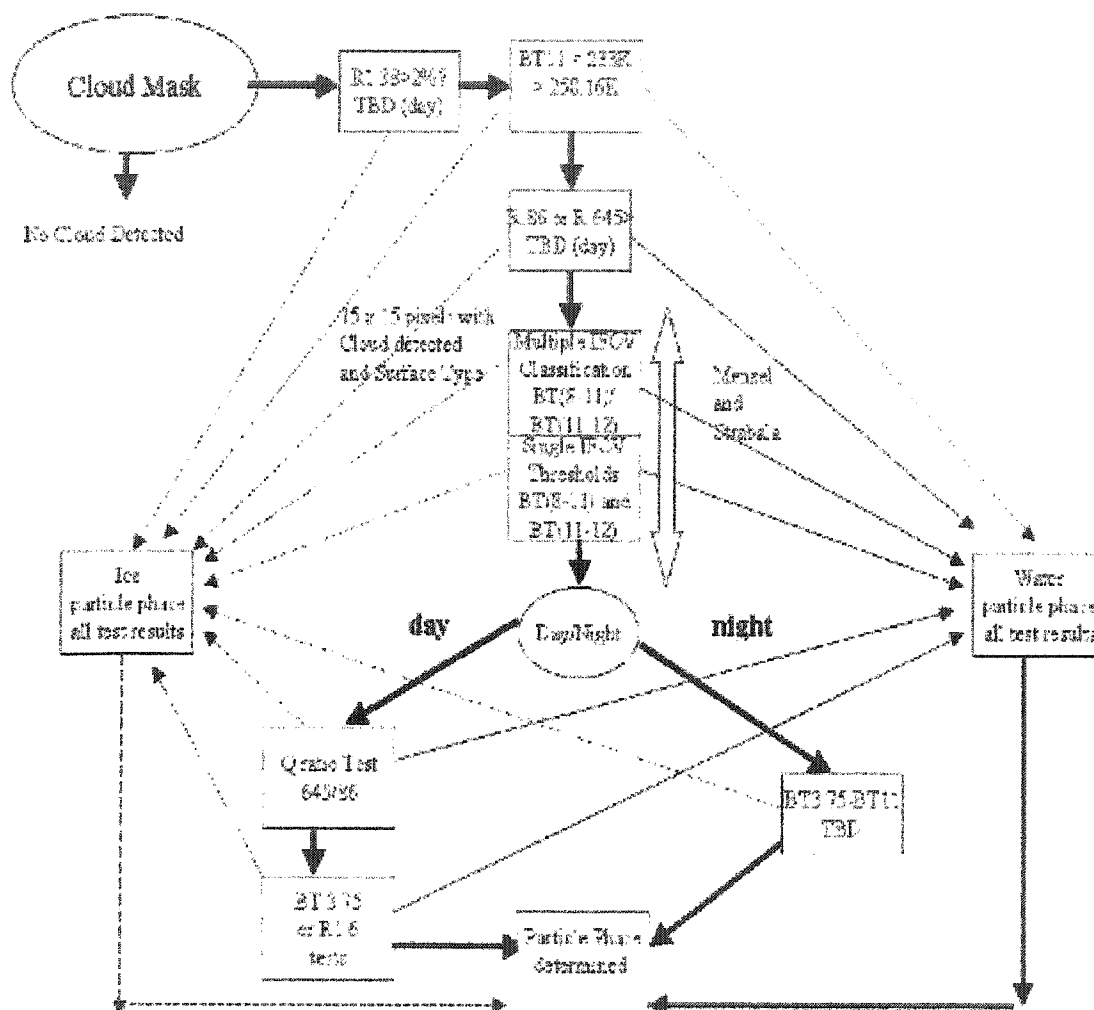


**Figure C-1: VIIRS Cloud Phase Algorithm.**

The reflectance at  $1.38 \mu\text{m}$  being greater than 2% is indicative of a high cirrus being present. The basis for this is that the large water vapor absorption in this band causes light reflected below the high cirrus cloud to be heavily absorbed, leaving the light measured by the sensor to consist predominantly of light reflected from high cirrus clouds. This phase test would only be done during the day, and would indicate ice phase only.



The BT11  $\mu\text{m}$  test is to be done day and night. For  $\text{BT}_{11} < 233 \text{ K}$  the ice particle phase is indicated, while for  $\text{BT} > 258.16 \text{ K}$  the water phase is indicated.

The R0.86 and R0.645 tests are reflectance tests based upon the reflectance of the clouds. For ice clouds the reflectance in both of these bands is less than that for liquid water clouds, which have large reflectance in these bands. The 0.645 band will be used over land, while the 0.86 band will be used over water, due to the large reflectance of vegetated surfaces at 0.86. Values for the thresholds indicative of phase are presently under development, however, there will be ranges of uncertainty and an angular dependence for these tests. This is a daytime only test.

In Figure C-1 the dashed lines indicate that this is a final decision that the cloud phase is designated and the phase classification is complete. However, the pixels thus classified are still used in the 15x15 pixel aggregation for Menzel and Strabala's tests (*Menzel and Strabala, 1997*). This is due to a need for enough pixels of defined distinct ice type to allow a well-defined slope for the multiple IFOV classification step. Ice clouds which have been classified by preprocessing tests are not reclassified a second time by the VCP algorithm, however the results of the multiple tests described below are flagged and may be used at a future point to indicate problems with tests performed.

Once the three initial cloud phase tests are performed, and a 15 x 15 matrix of determined and undetermined cloud phase pixels are collected then the Menzel and Strabala tests will be performed in a two step algorithm scheme.

The first step is a multiple Instantaneous Field of View (IFOV) classification of the 15x15 matrix of pixels. This step considers the slope of the BT(8-11) vs. BT(11-12) plot and determines the pixels which have dominant clustering about a common slope. This is developed from Menzel and Strabala's MODIS work (*Menzel and Strabala, 1997*). For the slope defined as  $\text{BT}(8-11)/\text{BT}(11-12)$  the pixel phase is defined as ice for slopes  $> 1.0$  and water for slopes  $< 1.0$ . The results in the pixel matrix are flagged based upon their clustered slopes, and those pixels which are not clustered are not flagged.

The second step is the Single IFOV Characterization of the 15x15 pixel matrix. This step uses a threshold approach to define the cloud phase. For  $BT(11-12) > 1.5$  K and  $BT(8-11) < 1.5$  K the cloud phase is determined to be ice, while for  $BT(11-12) < 1.5$  K and  $BT(8-11) > 1.5$  K the cloud phase is ice.

For those pixels which still do not have their phase determined additional tests will then be performed. Those tests are the Q ratio test (*Ou et al.*, 2000) and additional thresholding tests which employ the 1.6 and 3.75 bands, during the day. During the night one additional  $BT(3.75-11)$  test will be performed to detect ice clouds; this is a threshold test and the value is to be set.

Results of the various tests of the multiple IFOV classification, single IFOV characterization, and the threshold tests that follow are then all compared, and the decision of the final phase distinction is then performed. For cases in which there are tests that indicate both ice and liquid water the pixel will be flagged as a possible mixed phase, and for pixels with no cloud phase indicated the pixel will be flagged as unknown.

Once the cloud phase is determined it is included as part of the VCM output to the other EDRs. The knowledge of cloud phase will allow more accurate indexing of the Look Up Tables (LUT) used to retrieve the Cloud Optical Thickness and the Cloud Effective Particle Size EDRs (*Ou et al.*, 2000).

## Appendix D

### Error Budget and Flowdown Results

The process for establishing the error budget for the VIIRS EDRs is explained in The VIIRS System Verification Report (*Kealy and Ardanuy, 2000b*). The detailed discussion of errors contributing to the VIIRS EDR's and tables of error contributions are provided for insight into the origin and propagation of errors throughout the VIIRS System. Tracing of errors is intimately associated with the VIIRS Data Processing Architecture (DPA), which is comprised of a number of modules. Each module contains functional units for each of the scientific disciplines stated in the VIIRS SRD (*NPOESS IPO, 2000*). The VIIRS system comprises a sensor which generates scene radiances in a certain number of bands making up a Raw Data Record (RDR), and an algorithm subsystem which processes the RDR data through a series of interdependent algorithms to generate Environmental Data Records (EDRs). Intermediate products (such as Surface Reflectance) and Sensor Data Records (SDRs) are generated by algorithms that provide functionality more basic than the final EDR.

The accuracy and precision of both EDRs and SDRs depend to a large degree on conditions such as the presence of ocean, land, clouds, coastal areas, snow/ice; whether it is day or night; scan angle, and other conditions. The results of the tests are reported in the VIIRS Verification and Validation Plan (*Kealy and Ardanuy, 2000c*) in terms of system accuracy, precision, and/or uncertainty and/or stability. The VIIRS Error Budgets Document (*Kealy and Ardanuy, 2000b*) provides a breakout of the contributing errors for selected points or sub-areas in the stratified space along with justifications.

The VIIRS Algorithm Subsystem Specification (*Durham, 2000*) details the error specifications for ancillary and auxiliary data. The errors due to the ancillary and auxiliary data in the error budget are based on these specifications. Auxiliary data is defined to be all data from non-NPOESS sources, while data from NPOESS instruments, including VIIRS, are defined to be ancillary data. Hence, errors inherited from VIIRS

SDRs are referred to as resulting from ancillary data. The VIIRS System and Subsystem Specifications and their rationales document the EDR and SDR specifications at the system level, and the algorithm and sensor subsystem level. The error budget together with the VIIRS Validation and Verification Plan allows understanding of the error specifications. Based on error budget and stratification studies and analyses key error sources are identified. They provide a guide to instrument and algorithm developers to areas where improvements will have the greatest impact. Ultimately good error budgets lead to tighter specifications when margins can be tightened due to risk reduction based on reliable error estimation.

The design process used was a spiral process in which the specifications and performance of the sensor and algorithm design were improved iteratively. After the initial flowdown activity the algorithm data definitions provided requirements from each EDR to the sensor. The most stressing of these requirements became the first iteration for the sensor model. A better definition of the sensor model became available as a result of Cost As an Independent Variable (CAIV) studies, further definition of the sensor, and performance analyses of the end-to-end system.

The errors are assumed to be independent so that the total error is the square root of the sum of the squared errors, also called the Root Sums Squared (RSS). This assumption is made for both precision and accuracy. An exception are the error budgets based on probabilities. In those cases the total probability is either the product of its factors (for typing probability), or, for misclassification, the product of all misclassification probabilities. This is the case in the VCM error budget.

The error budget tables for the VCM (Table D-1 (a-d)) are identified by their name in the top left corner and by the case considered in the top right hand corner. For the case considered, all sensor errors are listed at the bottom with a product of the factors for the sensor performance on top of the sensor errors. The algorithm error sources are listed above the sensor error breakout. Above the algorithm error sources is the

algorithm performance, which is the product of the factors of the algorithm errors unless noted otherwise. The section under the header summarizes the specifications for the VCM scenario. The threshold and objective are taken from the VIIRS SRD document. The system specification is the VIIRS system specification. The system performance is the product of all the misclassification probabilities for algorithm and sensor errors. The system performance for the case under consideration shows how well the algorithm performs compared to the system specification.

**Table D-1 (a): Cloud mask daytime ocean error budget.**

VIIRS CLOUD COVER (Binary Map)			OCEAN, DAYTIME		Note that Probabilities do not RSS
Specification V3 (PDR) Preliminary Design Review March 21, 2000	Inputs		Probability of Correct Typing		
	Error	Unit	$\tau < 1$	$\tau > 1$	References and Notes
Threshold			>(TBD) at (TBS)% confidence level		(NPOESS IPO, 2000)
Objective			>(TBD) at (TBS)% confidence level		(NPOESS IPO, 2000)
System Specification			92%	99%	Cloudy/not cloudy, (Larsen, 2000a)
System Performance			92%	99%	
System Margin			0%	0%	
Algorithm Performance			98.0%	99.7%	total of algorithm errors
Surface Type misclassification	1	%	99.00%	99.99%	(Larsen, 2000a) only effects optically thin clouds.
Land/water mask	50	M			In surface misclassification
DEM elevation	50	M			In surface misclassification
Intrinsic Algorithm Error			99.00%	99.70%	
Sensor Performance			93.9%	99.6%	total of sensor errors
Geolocation ( $3\sigma$ )	200	M			In surface misclassification
NEdT	baseline		98.30%	99.90%	(Larsen et al., 2000a)
Calibration	baseline		99.00%	99.90%	(Hoyt, 1999)
MTF	baseline		97.50%	99.90%	(Kealy and Ardanuy, 1999)
Band-to-Band Mis-registration	0.2	Pixels			(Kealy and Ardanuy, 2000a) and (Larsen, 2000b)

**Table D-1 (b):** Cloud mask nighttime ocean error budget.

VIIRS CLOUD COVER (Binary Map)			OCEAN, NIGHTTIME		
Specification V3 (PDR) Preliminary Design Review March 21,2000	Inputs		Probability of Correct Typing		Note that Probabilities do not RSS
	Error	Unit	$\tau < 1$	$\tau > 1$	References and Notes
Threshold			>(TBD) at (TBS)% confidence level		(NPOESS IPO, 2000)
Objective			>(TBD) at (TBS)% confidence level		(NPOESS IPO, 2000)
System Specification			90%	96%	Cloudy/not cloudy, (Larsen, 2000a)
System Performance			91%	97%	
System Margin			1%	1%	
Algorithm Performance			98.0%	99.0%	total of algorithm errors
Surface Type misclassification	1	%	99.00%	99.99%	Only effects optically thin clouds. (Larsen, 2000a)
Land/water mask	50	M			in surface misclassification
DEM elevation	50	M			in surface misclassification
Intrinsic Algorithm Error			99.00%	99.00%	
Sensor Performance			93.1%	97.8%	total of sensor errors
Geolocation ( $3\sigma$ )	200	M			in surface misclassification
NEdT	baseline		97.00%	99.33%	(Larsen et al., 2000a)
Calibration	baseline		99.00%	99.91%	(Hoyt, 1999)
MTF	baseline		97.00%	98.53%	(Kealy and Ardanuy, 1999)
Band-to-Band Mis-registration	0.2	pixels			(Kealy and Ardanuy, 2000a) and (Larsen, 2000b)

**Table D-1 (c): Cloud mask daytime land error budget.**

VIIRS CLOUD COVER (Binary Map)			LAND, DAYTIME		
Specification V3 (PDR) Preliminary Design Review March 21, 2000	Inputs		Probability of Correct Typing		Note that Probabilities do not RSS
	Error	Unit	$\tau < 1$	$\tau > 1$	References and Notes
Threshold			>(TBD) at (TBS)% confidence level		(NPOESS IPO, 2000)
Objective			>(TBD) at (TBS)% confidence level		(NPOESS IPO, 2000)
System Specification			85%	93%	Cloudy/not cloudy, (Larsen, 2000a)
System Performance			90%	97%	
System Margin			5%	4%	
Algorithm Performance			98.0%	99.0%	total of algorithm errors
Surface Type misclassification	1	%	99.00%	99.99%	Cloudy/not cloudy, (Larsen, 2000a) in surface misclassification in surface misclassification
Land/water mask	50	M			
DEM elevation	50	M			
Intrinsic Algorithm Error			99.00%	99.00%	
Sensor Performance			92.2%	98.3%	total of sensor errors
Geolocation ( $3\sigma$ )	200	M			In surface misclassification
NEdT	baseline		97.00%	99.90%	(Larsen et al., 2000a)
Calibration	baseline		99.00%	99.00%	(Hoyt, 1999)
MTF	baseline		97.00%	99.40%	(Kealy and Ardanuy, 1999)
Band-to-Band Mis-registration	0.2	pixels			(Kealy and Ardanuy, 2000a) and (Larsen, 2000b)

**Table D-1 (d):** Cloud mask nighttime land error budget.

VIIRS CLOUD COVER (Binary Map)			LAND, NIGHTTIME		
Specification V3 (PDR) Preliminary Design Review March 21,2000	Inputs		Probability of Correct Typing		Note that Probabilities do not RSS
	Error	Unit	$\tau < 1$	$\tau > 1$	References and Notes
Threshold			>(TBD) at (TBS)% confidence level		(NPOESS IPO, 2000)
Objective			>(TBD) at (TBS)% confidence level		(NPOESS IPO, 2000)
System Specification			85%	90%	Cloudy/not cloudy, (Larsen et al., 2000a)
System Performance			90%	91%	
System Margin			5%	1%	
Algorithm Performance			98.0%	99.0%	total of algorithm errors
Surface Type misclassification	1	%	99.00%	99.99%	Only effects optically thin clouds. (Larsen et al., 2000a) in surface misclassification in surface misclassification
Land/water mask	50	M			
DEM elevation	50	M			
Intrinsic Algorithm Error			99.00%	99.00%	
Sensor Performance			92.2%	92.2%	total of sensor errors
Geolocation ( $3\sigma$ )	200	M			In surface misclassification
NEdT	baseline		97.00%	97.00%	(Larsen et al., 2000a)
Calibration	baseline		99.00%	99.00%	(Hoyt, 1999)
MTF	baseline		97.00%	97.00%	(Kealy and Ardanuy, 1999)
Band-to-Band Mis-registration	0.2	pixels			(Kealy and Ardanuy, 2000a) and (Larsen, 2000b)

The system margin is the difference between the system specification and the system performance for the case considered in the error budget. Since the error budget may be for a point, or a sub-range, or some average over the total stratification considered, the margin is only an indication of the spread between performance and specification. Other points in the stratification will generally have a smaller or larger margin.



The sensor baseline as specified in the VIIRS Sensor Specification (*Kealy and Ardanuy, 2000d*) is used for the derivation of the error budgets.

The sensor errors are:

- Sensor Noise - The error due to sensor noise in each VIIRS radiometric band is used by all error budgets.
- The Modulation Transfer Function (MTF) model provides information on how the sensor spatial sensitivity affects the data.
- Band to Band Registration
- Polarization (instrument)
- Calibration Errors
- Ancillary/Auxiliary Data

Note that the EDRs like the VIIRS cloud mask, and the SDR of surface reflectance are both dependent on auxiliary and ancillary data and are themselves ancillary data to other EDRs, and may as such be regarded as error sources within other EDRs.

The VIIRS cloud mask produces the binary cloudy/not cloudy map, a component of the Cloud Cover/Layers EDR. The cloud mask error budget has been stratified over day and night considering ocean and land surfaces. A basic assumption is that the setting of cloud detection thresholds in the development of the cloud mask employs the full range of realistic cloud reflectances and BT values. To minimize this specification error the cloud mask has been developed using MAS and VIIRS simulated data. The cloud mask errors are expressed as probability of correct typing.

There are three categories of error sources: sensor, ancillary and auxiliary data, and intrinsic algorithm. The sensor error component is the sensor noise, which is determined by the noise components of the baseline sensor model and Modulation Transfer Function (MTF) model. A band-to-band mis-registration study has been performed in Chapter 3, in which the radiance of all bands used by the VCM were mis-registered horizontally and vertically. This study shows that gross errors in the VCM occur when band-to-band mis-registration exceeds 20% (*Larsen, 2000b*).

Errors due to sensor noise are discussed in the Signal to Noise Requirements for VIIRS Cloud Mask and Cloud Cover (*Larsen et al.*, 2000a). Simulations of VIIRS radiances and imagery were generated with different sensor noise models and automated analyses of simulated imagery were then compared against true cloud fields used to generate the simulations. The intrinsic error is the error that the algorithm has when all other sources are free of error. The VCM algorithms properties are considered to have components that contribute to the intrinsic algorithm error.

Errors in surface type affect the VCM error budget. Presently the ecosystem and land/sea maps used by the VCM are the same as those used by MODIS. MODIS considered these maps to have a 1% error of surface type classification. For the assessment of the size of this error it is assumed that surface type misclassification is minimal in the large homogeneous surface types of the earth, i.e. minimal over the oceans and the vegetated land regions. The effect of surface misclassifications will be greatest in regions with snow/ice which is not known to be there. This is considered to be a small set of the total pixels which the VCM will map. It is important to note that the error in surface types will affect the detection of optically thin clouds, in particular those with optical thicknesses less than 0.5. The optically thick clouds are very easy to detect, due to their spectral features, so error in surface types are considered to be insignificant for thick clouds.

The error sources listed below are actually more clearly defined errors in surface type, i.e. snow/ice typing error and land/water map resolution error. These error sources have all been merged together to comprise the total error. Due to the low amount of surface misclassification this error source is assessed as being very small. Details on the accuracy of retrieving surface types which the cloud mask uses can be found in the works of *Hansen et al.* (2000) and the MODIS Surface Type ATBD (*Strahler et al.*, 1996).

The algorithm first determines the dominant surface type in the pixel. To do this both the latitude and longitude of the pixel are used in combination with a global map which references the surface type. This is presently done using the Olson map at 10 minute resolution. A one kilometer spatial resolution map is desired, and for the MODIS cloud mask there are plans to develop one. If the surface type determination is incorrect, the wrong cloud detection thresholds will be used for cloud detection. This error accounts for that probability. Since this error is actually very small it is not considered to be a dominant error term. Values have been placed into the VCM error specification tables based upon preliminary assessment of the effect of this error upon cloud detection.

One of the surface types that the algorithm needs to have knowledge of is snow/ice presence within the pixel being masked. This requirement applies for all pixels considered, either cloudy or clear. To identify the presence of snow and ice, the most recent snow/ice map, updated by VIIRS, will be used in combination with CMIS snow/ice detection knowledge if it is available, and a scaled down version of the MODIS snow/ice detection test. No dependence on CMIS data is implied. A fallback for this test is the use of climatological snow/ice extent. The cloud mask algorithm has included preliminary assessments of this typing error in the VCM error specification table.

This error source is a direct error in surface type. The resolution of the land/water map employed with the cloud mask affects the degree of misclassification. It is believed that the resolution will have the greatest impact in coastal regions and for small islands. A land/water map is a MODIS product, generated at 1 km resolution. Presently the land/water map used by VIIRS is from the Eros Data Center (EDC). It is expected that a Land/Water map will be developed by VIIRS for future use by the community.

Also with TOA reflectance values used for daytime cloud detection by the VCM, uncertainty in the sun/sensor geometry is a possible error source. For sun/sensor

geometries which minimize the path length of the sunlight through the atmosphere, this error source is the greatest, while for long path atmospheric path lengths this error is minimized. This because the greater path lengths increase the effect of the cloud on the photon propagation and hence increase the chances of detecting the cloud. Sun/sensor geometry is also used in determining regions of possible sunglint. In these regions daytime reflectance tests are questionable, however nighttime thermal only cloud detection will be done. The angular uncertainty will possibly broaden the sunglint regions, which would affect the probability of correct typing capabilities, due to varying capability of night and day time cloud detection.

Extraterrestrial properties lead to an additional error category, which combines all errors due to extraterrestrial sources. These error sources are shown in Table D-2 below, which summarizes the error allocated to the inputs to the algorithm and provides a reference where the basis for the error allocation to the cloud mask is documented. If an error source is not ancillary or auxiliary input the 'input source uncertainty' field lists "N/A".

The solar spectral irradiance has uncertainties that could amount to as much as several percent at different wavelengths based upon comparison of different published spectra. The current assumption is that the Thuillier solar spectrum will be used and it has uncertainties of as large as 0.5% (*Thuillier et al.*, 1997).

The solar spectrum is not constant but varies with solar activity. Since measurements of the total solar irradiance are not published for between several months to several years after they are made, it is assumed that they will not be available to the VIIRS team for inference of changes in the spectral irradiance on an operational basis. This will give rise to an unknown random error in the spectral irradiance of about 0.1% with greater variability for shorter wavelengths. Because the VCM depends primarily upon the longer wavelengths in the visible and near-IR spectrum variations are expected to have minimal effects. The Earth-Sun distance is well known and should not be a

significant error source. The only caveat is that if a simplified formula is used that actually gives the Earth-Moon barycenter to sun distance, false monthly and annual cycles can be introduced into the retrievals.

**Table D-2:** Error allocation to inputs to the cloud mask module.

<b>Error Source</b>	<b>Input Source Uncertainty</b>	<b>Reference Documentation of Basis for Error Allocation</b>
Recent Snow/Ice Map typing Error	10%	VIIRS Snow Cover requirement ( <i>NPOESS IPO, 2000</i> )
Land/Water Map Misclassification Error	50 m vertical	VIIRS Cloud Mask ATBD ( <i>Larsen, 2000a</i> )
	1 km horizontal	
Topographical Map Error	50 m vertical	VIIRS Cloud Mask ATBD ( <i>Larsen, 2000a</i> )
	1 km horizontal	
Error in Surface Type	1%	MODIS
Sun/Sensor Geometry Angular Uncertainty Error	32 arcsec	VIIRS RDR Module Level Build Structure ( <i>Kuin, 2000</i> )
Solar Irradiance Uncertainty	0.5%	( <i>Thuillier et al., 1997</i> )
Solar Activity Variations	0.2%	( <i>Hoyt et al., 1992</i> )
Sun Glint mask error	N/A	6S simulation of orbit

The concept of automated cloud detection in multispectral imagery, used to generate the automated cloud mask, is based upon a robust methodology which employs a series of tests that exploit the spectral signatures of ice and water clouds. This methodology is robust because clouds that may not be detected by one single test, described in Chapter 2, will generally be detected by another. Often, clouds are detected by multiple tests. This redundancy in cloud detection tests provides assurance that cloud detection is unlikely to fail, even as the VIIRS sensor or ancillary data become degraded with time or circumstances, e.g., ancillary data are not available. However, due to the

binary nature of a cloud mask, being cloud/no cloud, the terms like accuracy and precision cannot readily be used to construct an error budget for the cloud mask. The misclassification of the cloud mask is being used to assess the performance of the VCM.

One is unable to assess the performance of the cloud mask in terms of accuracy and precision requirements that are defined by the VCM product for the Cloud Cover/Layers EDR, misclassification of the cloud mask is thereby used as a merit of performance. Misclassification is the percentage of pixels within a given scene that are classified as cloudy when clear or clear when cloudy. The rationale behind this subdivision of the misclassification is that each case of misclassification will affect various EDRs in different ways. For demonstrations of the misclassifications, refer to the cloud mask flowdown performed in this chapter and chapter three. Subdivision into the two misclassifications, cloudy when clear and clear when cloudy, is important because the misclassification of clear when cloudy will affect VIIRS surface EDRs, while the misclassification of cloudy when clear will affect the cloud EDRs. The goal of the cloud mask algorithm development is to minimize the amount of misclassification. The probability of correct typing of the VCM is one minus the total misclassification.

Because the cloud mask is evaluated based upon misclassification, a plan has been devised to evaluate the impact of system-level errors on the automated cloud mask product in terms of misclassification in order to determine which, if any, are system drivers. The procedure uses numerous simulations of VIIRS imagery under different levels of degradation, described below.

Automated analyses of simulated imagery are then compared against ground truth cloud masks used to generate the simulations as described in the VIIRS Imagery ATBD (*Jensen et al.*, 2000). These pixel-level comparisons between the automated cloud mask and the ground truth cloud mask have proven useful for quantitative error budget analyses (*Jensen et al.*, 2000; *Hutchison et al.*, 1997; *Hutchison and Choe*, 1996; *Hutchison and Hardy*, 1995; *Hutchison et al.*, 1995). A theoretical description of the

errors which will be evaluated is provided. The total misclassification in the cloud mask product can be estimated as:

$$M_{tot} = 1 - \left( (1 - M_{geo}) * (1 - M_{BBR}) * (1 - M_{dyn}) * (1 - M_{NEdL}) * (1 - M_{alg}) * (1 - M_{rad\_acc}) * (1 - M_{anc}) * (1 - M_{alg}) * (1 - M_{bb}) \right) \quad (D-1)$$

while one can represent the total misclassification as the sum of two terms, cloudy when clear (M1) and clear when cloudy (M2), as follows:

$$M_{tot} = M_1 + M_2 \quad (D-2)$$

At present, the interacting effects of the ensemble of error sources are not yet clear and are hence hard to assess. Therefore, the error sources have initially been assumed to contribute independently to cloud misclassification. Further studies on this topic are necessary. The different error sources will be investigated separately.

The probability of correct typing, which is used in the assessment of the cloud mask performance is as follows:

$$P_{tot} = 1 - M_{tot} \quad (D-3)$$

This is a measure of the total probability of correct typing.

Errors due to geolocation/regional misclassification have been considered. Simulations of VIIRS radiances and imagery generated for erroneously classified regions and automated analyses of simulated imagery are then compared against ground truth cloud masks. This is considered to be an error source which contributes directly to the error in surface type.

Errors due to band-to band mis-registration have been considered. Simulations of VIIRS radiances and imagery generated with band-to-band registration errors of different amounts of pixel mis-registration, and automated analyses of imagery are then compared against ground truth cloud masks used to generate the simulations. The Band-to-Band Mis-registration (BBM) study is described in detail in chapter three. As a result of this study it was recommended that BBMs be kept less than 20% for the VIIRS sensor.

Simulations of VIIRS radiances and imagery were generated with different sensor noise models and automated analyses of simulated imagery were then compared against true cloud fields used to generate the simulations.

Errors due to surface type misclassification have been considered as well. Presently the ecosystem and land/sea maps used by the VCM are the same as those used by MODIS. The MODIS team has considered these maps to have an accuracy of 1%. For the assessment of the size of this error it must be considered that surface type misclassification is minimal in the large homogeneous surface types of the earth, i.e. minimal over the oceans and the vegetated land regions. The effect of surface misclassifications will be greatest in regions with snow/ice cover which is not known to be there. This is considered to be a small set of the total pixels which the VCM will map.

For errors of continuity the analysis will have to rely on a future assessment. Since many of the VIIRS bands resemble the MODIS bands, continuity with respect to the MODIS sensor is straightforward. With respect to bands which resemble AVHRR, the spectral and spatial aggregation requires further study.

Errors due to Modulation Transfer Function (MTF) were considered and found to be minimal. For the VIIRS system it was found that MTF does not play a large role in affecting cloud detection (*Kealy and Ardanuy, 1999*).

At this time, the sensor is assumed to be a polarization insensitive instrument. If true, the errors due to polarization are not significant. It is believed that ocean EDRs are



more affected by this potential problem. In addition the bands used by the VCM are all at wavelengths  $> 0.60 \mu\text{m}$ . This is believed to minimize the effects of polarization.

For addressing errors due to out-of-band response the experience with MODIS has indicated that some detectors are vulnerable to signals far outside their targeted spectral range (out-of-band leakage). Additionally, any detector will have a spectral response that will include contributions from the immediately surrounding wavelengths, as the bandwidth itself is generally defined by selecting the Full-Width Half-Maximum (FWHM) of the spectral response curve. While the VCM will be affected, it is believed that these effects will be minimal.

An attempt has been made to assess the cloud mask error budget as defined in Eq. (D-1) above. For the various cases, values have been inserted either from flowdown results or from experience with the cloud masks capabilities. The error budget is shown in Tables D-1 (a-d). In this table the performances are the lowest probabilities of correct typing for the water and land surface types considered.

## Appendix E

### Sensor Noise Flowdown and Cloud Cover Flowdown Analysis

This appendix summarizes the flowdown of the System Requirements Document (SRD) requirements for the VIIRS cloud cover to the Signal-to-Noise Ratio (SNR) of the VIIRS sensor for the baseline bands indicated in the table below. Background on the sensor models considered in this document is provided elsewhere (Kealy, 2000).

Thus far, cloud detection does not appear to be a major VIIRS sensor driver, for sensor noise. For sensor noise flowdown cirrus cases were analyzed. Cirrus cloud cases are considered to be the most challenging cases for cloud detection, stressing the cloud detection capabilities of algorithms under development. For daytime retrievals, noise models 1 –5 are suitable for retrieving cloud cover based on channels used by the VCM (Kealy, 2000). For nighttime retrievals noise models 1-5 are suitable for cloud cover inferred from the thermal VIIRS channels. Further tests are needed in the future for cases of liquid water, and ice clouds over snow/ice and water surfaces in typical arctic and typical tropical atmospheres and for off-nadir satellite sensor geometry. It is desirable to test scenarios involving off-nadir cases, additional climatological profiles, and liquid water and ice clouds at varying heights. In addition, the impact of aggregation must be studied for a wider range of cloud types and amounts.

The assumptions made for the cloud flowdown results are briefly described here. They relate to model scenarios used in the radiative transfer cloud scene generation, and modeling assumptions and approximations made within the testbed environment.

**Table E-1:** Scenario list of simulated data for sensor noise flowdown.

<b>Scenarios</b>	<b>Description</b>
Scene #1	Ice Cloud (9-10 km), Midlatitude, Nadir, Solar Z = 32
Scene #2	Ice Cloud (9-10 km), Midlatitude, Nadir, Night
Scene #3	Water Cloud (3-4 km), Midlatitude, Nadir, Solar Z = 32
Scene #4	Water Cloud (3-4 km), Midlatitude, Nadir, Night
Scene #22	Ice Cloud (9-10 km), Midlatitude, Edge-of-Scan, Solar Z = 32
Scene #23	Ice Cloud (9-10 km), Midlatitude, Edge-of-Scan, Night
Scene #25	Water Cloud (3-4 km), Midlatitude, Edge-of-Scan, Night

These tests were developed using radiative transfer model results from two separate scenarios, a nighttime case and a daytime case, for a listing of the scenarios used in the flowdown see Table E-1. A sample description is given below for the cases used to demonstrate flowdown:

- Atmosphere: US standard atmosphere profile data
- Haze: rural aerosol and 23 km visibility at surface
- Sensor Geometry: Nadir sensor view
- Sensor Altitude: 833 km
- Solar Geometry (*daytime* case): 32° local zenith angle (Z)
- Nominal day-of-year/location: 1 May, 40° North
- Cirrus Cloud Height: 9 – 10 km (All tests except Window IR)
- Water Droplet Cloud Height: 3 – 4 km (Window IR tests only)
- Wide range of optical depths and constant effective particle sizes for both the cirrus and water droplet clouds

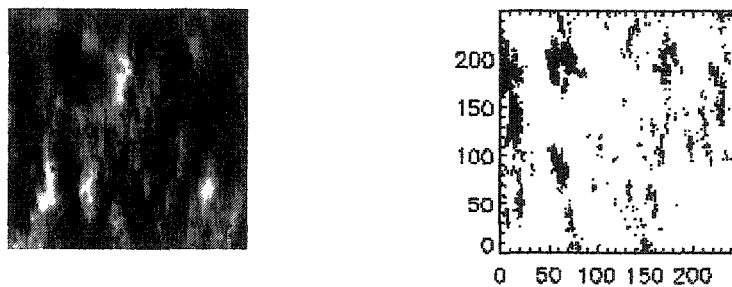
The subsequent allocation of cloud amount to specific vertical layers is a largely subjective process following the execution of the VCM and also relying upon other EDRS (e.g., cloud top temperature) to discriminate between vertical layers within the same horizontal cell. Comparison of cloud amount assigned to specific layers with ground truth layered cloud structure does not yield useful flowdown information because the cloud layer allocation algorithm is empirically forced to minimize both accuracy and precision type errors.

A flowdown analysis for cloud cover using the VCM was performed. This analysis has been employed to determine the cloud cover for several cloud scenarios, outlined in Table E-1. Representative results of that flowdown analysis for a cirrus cloud case is considered.

The SNR tests address the impact of SNR on both pixel-level retrievals and retrievals when the pixel-level retrievals are aggregated (averaged) to VIIRS SRD horizontal cell size (HCS). The required HCS is a function of the EDR parameter; threshold and objective values are stated. For the study aggregations are done at the cloud cover HCS threshold (25 km) and HCS objective (5 km). The VCM test results are presented separately for the daytime and nighttime cases.

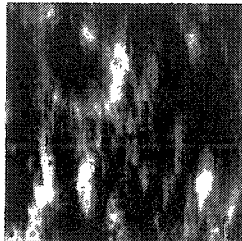
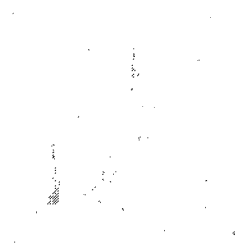
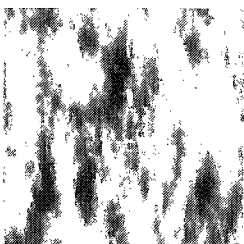
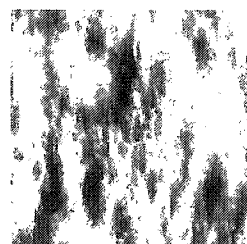
The simulation process used to generate the cloud covered radiance images is discussed in Chapter 2. Radiance scenes at all channels used in the VCM were generated using MODTRAN, with improved multiple scattering capabilities, (*Berk et al.*, 1989; *Larsen*, 1994) and the UCLA Double-Adding (*Ou et al.*, 2000) radiative transfer codes. For the simulations a cloud effective particle size of 20.7  $\mu\text{m}$  and optical thickness ( $\tau$ ) values 0-8 were adopted. The radiance image constitutes the 'no noise' case. Subsequently, noise was randomly added to the 'no noise' radiance bands using noise models (*Kealy and Ardanuy*, 2000e). Precision and accuracy metrics were computed using the SRD definitions (*NPOESS IPO*, 2000). The radiance scenes used were 0.4 x 0.4 km pixels; for these pixels a binary cloud mask result 0/1, clear/cloud,

was determined with the VCM. When aggregated to the 25 km cell size threshold, the HCS was composed of 62 x 62 pixels; for the 2 km objective cell size, the HCS was composed of 5 x 5 pixels. The threshold and objectives were summarized previously in Chapter 2. The VCM binary results were summed up and divided by the total number of pixels within the threshold/objective cell size to determine fractional cloud cover. These cloud cover results were then compared to the ‘truth’ which was generated for cloud optical thicknesses  $> 0.03$  within a pixel, providing a clear/cloud binary result, which was similarly aggregated to provide ‘truth’ cloud scenes at the threshold and objective HCS.



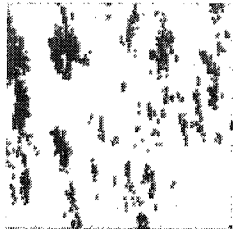
**Figure E-1 (a-b):** Optical thickness and truth case. (a) Optical thickness at  $0.65 \mu\text{m}$ . (b) The ‘truth case’ where the optical thickness is greater than 0.03.

Figure E-2 depicts the reflectance and BT scenes for the 88% coverage cirrus cloud covered case generated for the VCM retrievals. The radiance fields from which these scenes are derived had the noise models applied to them and the cloud mask generated from the noise-infected scenes (Figures E-3 and E-4). From these figures it is apparent that as the noise level increases the cloud mask begins to give false results. Figure E-1 shows the optical thickness and the ‘truth case’ pixels in which the optical thickness is greater than 0.03, which indicates a clouds presence.

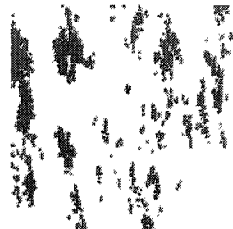
a) Band 0.65  $\mu\text{m}$  Reflectanceb) Band 0.86  $\mu\text{m}$  Reflectancec) Band 1.375  $\mu\text{m}$  Reflectanced) Band 3.75  $\mu\text{m}$  BTe) Band 10.8  $\mu\text{m}$  BTf) Band 12  $\mu\text{m}$  BT.

**Figure E-2 (a-f):** Simulated reflectances and BT of the VIIRS channels. These channels were used in the VIIRS cloud mask algorithm.

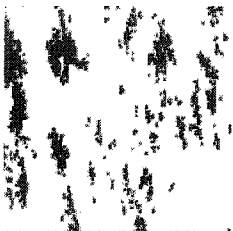
a) Optical Depth truth



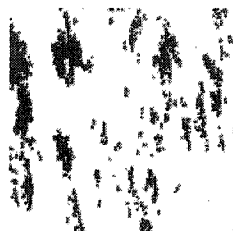
b) VCM no noise



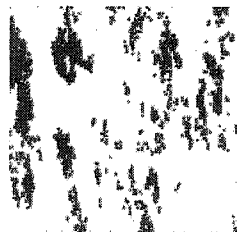
c) VCM Noise Model 1



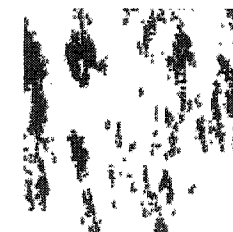
d) VCM Noise Model 2



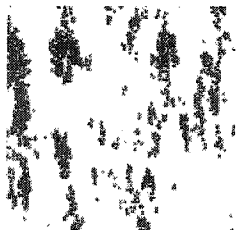
e) VCM Noise Model 3



f) VCM Noise Model 4



g) VCM Noise Model 5



h) VCM Noise Model 6

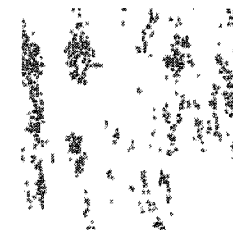


**Figure E-3 (a-h):** Noise models applied to daytime Cloud Mask. The VIIRS Cloud Mask results with no noise and six noise models applied to the radiance fields.

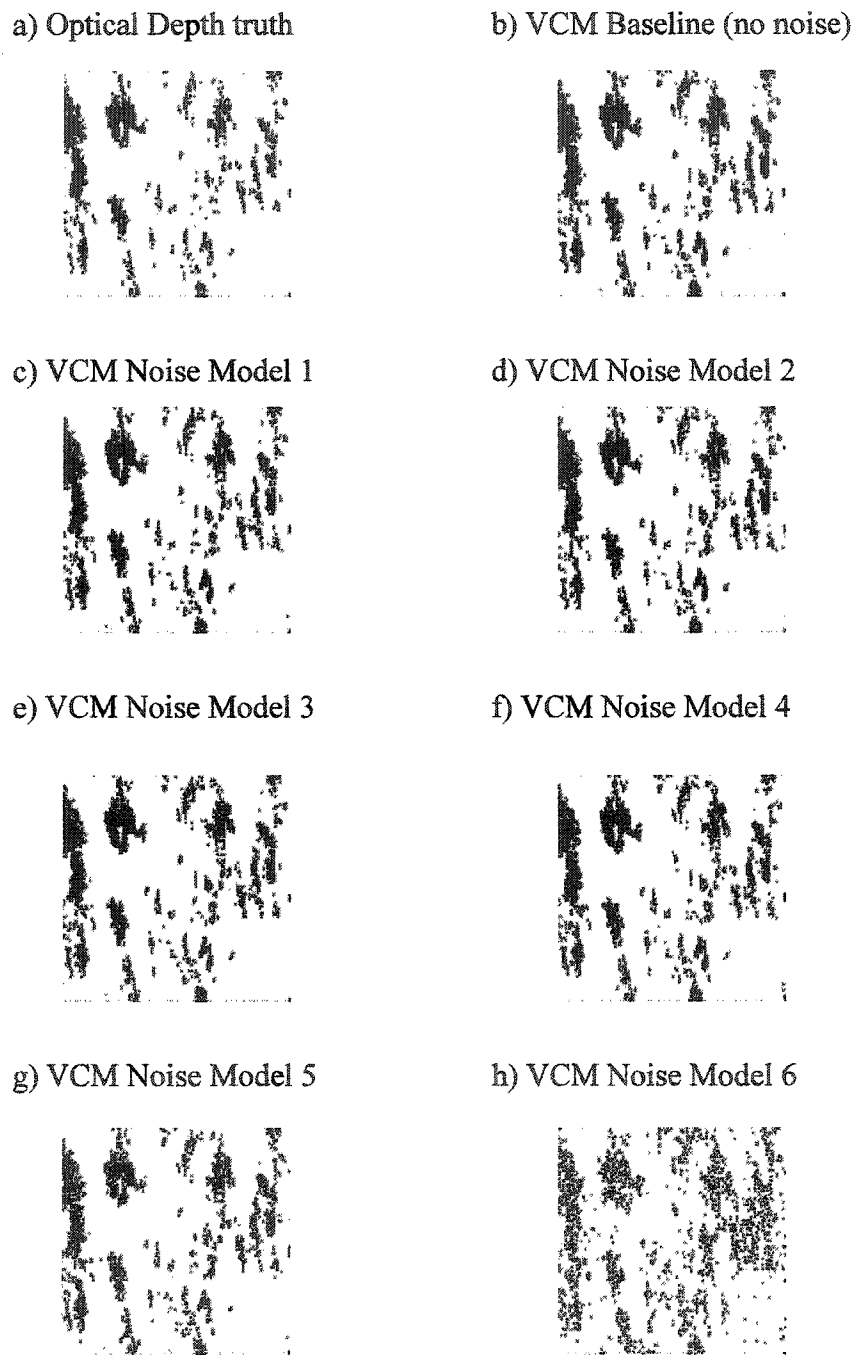


**Figure E-4 (a-h):** Noise models applied to nighttime Cloud Mask. The VIIRS Cloud Mask results with no noise and six noise models applied to the radiance fields.



Figures E-3 and E-4 display the day and night VCM cloud detection results at a pixel level for the baseline no noise case and the retrievals using the six noise models. The seventh was excluded because it was found in all cases to produce an unacceptable cloud mask, and hence cloud cover, results.

Figures E-5 and E-6 show the resulting accuracy and precision for the noise models at both threshold and objective HCS. The diamonds and triangles depict the computed results, while the squares and X's depict the SRD accuracy threshold (0.1 cloud fraction) and objective (0.05 cloud fraction) respectively (*NPOESS IPO*, 2000). Two accuracies and two precisions are depicted for each individual figure. The reason for this is the behavior of the SRD defined accuracy and precision. The modified accuracy and precision are shown as triangles on these figures, while the SRD defined accuracy and precision are depicted as squares. In these accuracy figures (a) displays accuracies for the noise models compared to the 'truth case', from the cloud optical thickness  $> 0.03$  in Figure E-1. In order to assess the effect of SNR upon the algorithm for flowdown, all of the results in these figures are relevant. However, the most relevant from experience gained is the modified precision and accuracy results. These figures demonstrate that for the 25 km threshold HCS during day and night the cloud cover's objective precision and accuracy is attainable for the thin cirrus case over land at nadir out to sensor noise model five. Figure E-5 indicates that for the 2 km HCS cloud cover the daytime cases are good out to noise model five, exceeding objective for the accuracy and attaining objective for the precision. However, for the nighttime case the cloud cover does not meet threshold. When the cloud detection thresholds are more precisely set in the developmental stage of the VCM, the accuracy of the cloud cover retrieval will be between threshold and objective.

## HCS: 25 km (threshold)

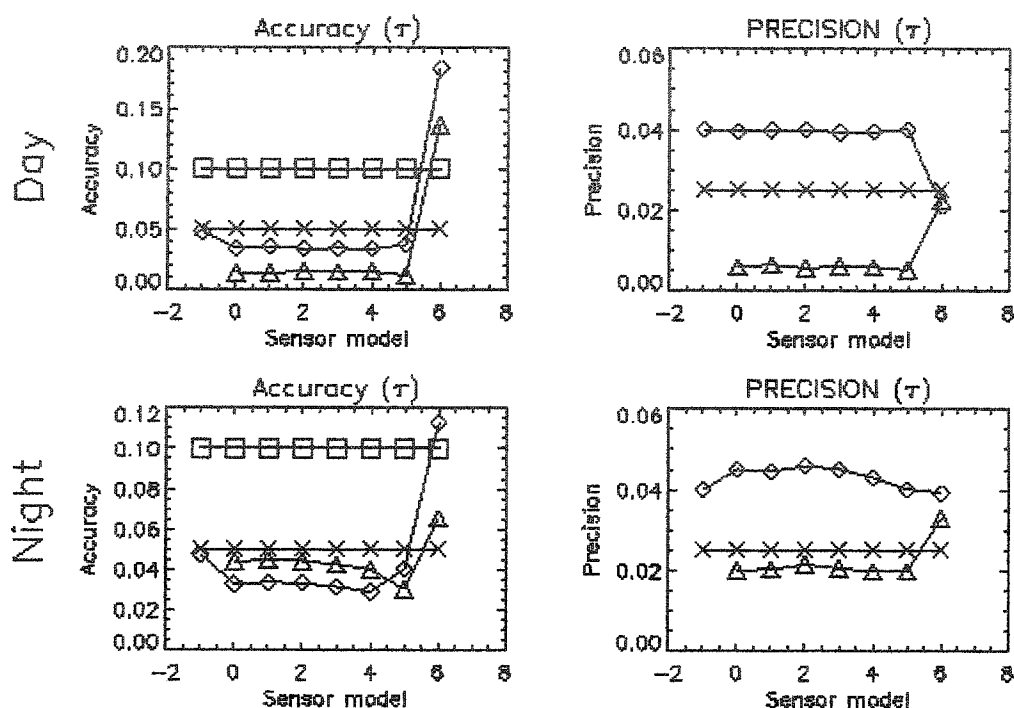


**Figure E-5:** VIIRS Cloud Cover accuracy and precision at 25 km. The VIIRS cloud cover day and night accuracy and precision results for the 25 km threshold HCS, with no noise and six noise models applied to the radiance fields. Results depict the accuracy and precision compared to the optical depth truth.

## HCS: 2 km (Objective)

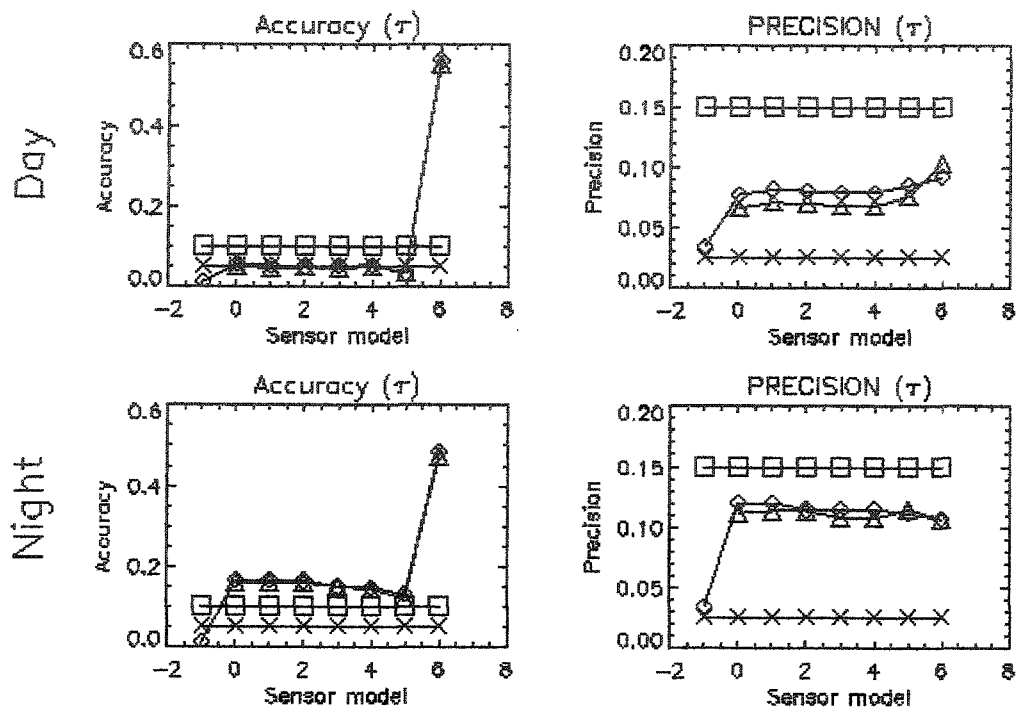


**Figure E-6:** VIIRS Cloud Cover accuracy and precision at 2 km. The VIIRS cloud cover day and night accuracy and precision results for the 2 km threshold HCS, with no noise and six noise models applied to the radiance fields. Results depict the accuracy and precision compared to the optical depth truth.

## **Appendix F**

### **Cloud Mask Validation and Simulation**

The VCM algorithm validation has been based on the inter-comparison of clouds simulated using radiative transfer codes with the true cloud scenes being simulated, and using real MODIS Airborne Simulator (MAS) radiance scenes.

The synthetic imagery data sets used for Cloud Mask validation and verification were generated using the MODTRAN and UCLA Radiative Transfer (RT) model (*Ou et al.*, 2000), and the Cloud Scene Simulation Model (CSSM) (*Apling et al.*, 2000). The process used to generate synthetic scenes is illustrated in Figure F-2, samples of simulated scenes generation are provided in Figure E-2.

The RT model is executed over a wide range of effective particle sizes and optical depths, for a specified atmospheric scenario, sensor geometry, solar geometry, VIIRS channels, and cloud type, altitude and thickness. The results are stored in the radiance Look-up Tables (LUTs). The radiance LUTs are used in conjunction with data from the CSSM, which is described in more detail below, to create synthetic radiance images for the VIIRS bands. The cloud EDR algorithms are applied to the synthetic imagery and retrievals are performed at the pixel-level. The pixel-level retrieval results are aggregated to the appropriate Horizontal Cell Size (HCS) for the EDR and compared with truth.

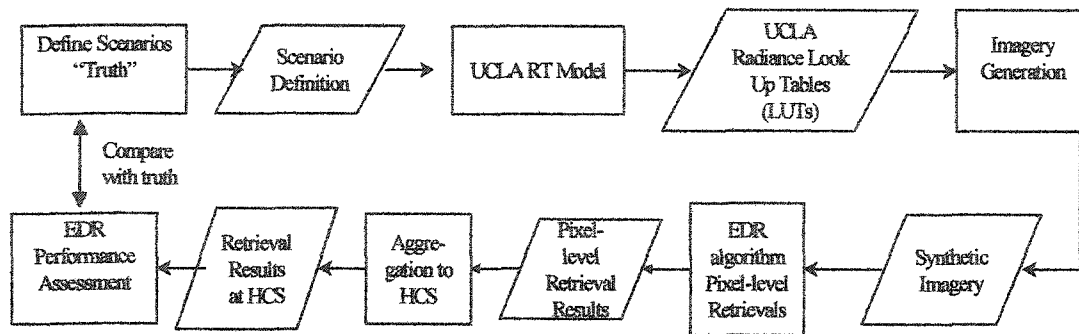


**Figure F-1:** Synthetic imagery generation diagram. High level diagram of the synthetic imagery generation and performance assessment process for the cloud EDRs.

Figure F-2 focuses on the imagery generation box of Figure F-1. CSSM is used to generate 3-D fields of cloud liquid water (CLW) or cloud ice water content (IWC) for specified cloud type, cloud coverage, etc. In the scene generation process for cloud EDR Testing, CSSM is used to generate 3-D synthetic cirrus and water droplet cloud distributions over a 100x100 km area at 0.1 km spatial resolution throughout the volume. These data are vertically integrated to form grids of Ice Water Path (IWP) or Cloud Liquid Water (CLW), depending upon the cloud type, at 0.1 km resolution over the 100x100 km region. The IWP and CLW data are converted to visible optical depth using standard relationships for each cloud type (water or ice). In addition, a scaling factor is used to tune the resultant optical depth grids, such that all values fall within a specified range, e.g to support stratification tests. The optical depth grids are used in conjunction with the radiance LUTs to create 100x100 km radiance images at 0.1 km resolution for each VIIRS cloud channel. Within each image, cloud top height, cloud thickness, and cloud effective particle size are set to nominal values over the entire image, consistent with the radiance data. Cloud optical thickness, however, varies considerably over the image. At this stage of the processing, sensor characteristics such as MTF, BBM, calibration, and geolocation errors are introduced, as necessary. The 0.1 km radiances are aggregated to the appropriate VIIRS pixel size, which varies according

to sensor viewing geometry. Pixel-level sensor noise is then introduced, resulting in synthetic imagery which include sensor effects.

Because VIIRS pixel level radiances are generated from higher resolution data, the resultant simulated VIIRS imagery contains cloud edge effects (mixture of clear and cloudy radiances) and variation of optical depth even within the pixel. This yields a very challenging retrieval environment to test the cloud mask algorithm.

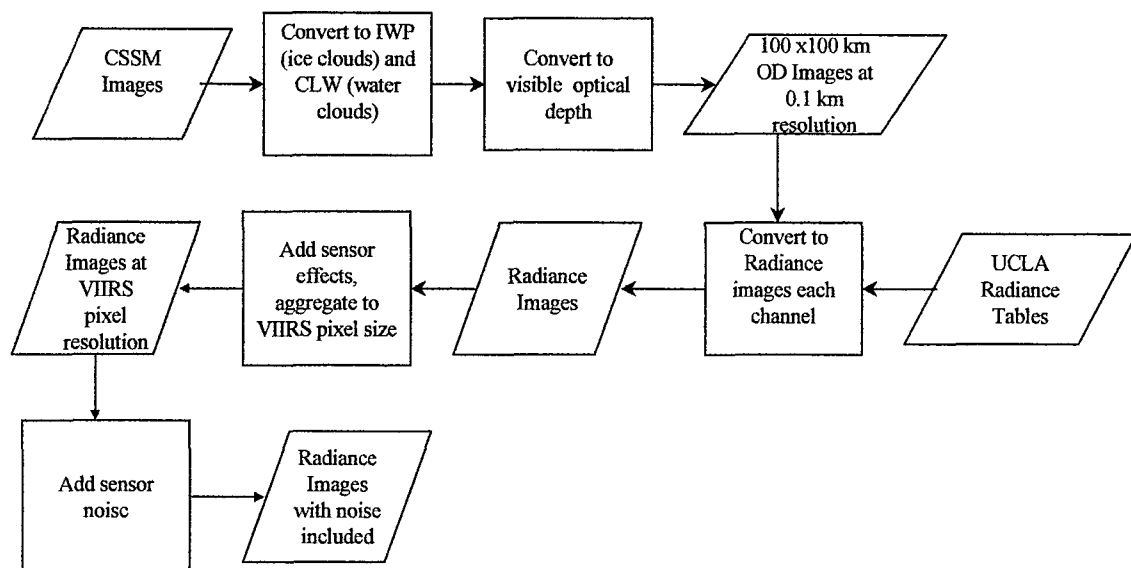


**Figure F-2:** The process for imagery generation. Imagery generation process using CSSM data, radiance LUTs, and sensor data.

For the simulated scenes discussed above, cloudy scenes were generated for varying cloud optical properties, height, phase, atmospheric type, and underlying surfaces. The number of possible scenes which might be used for cloud mask validation is overwhelming to consider. Therefore only a limited number of scenes will be presented in this appendix. The scenes considered are illustrated in Table F-1. Of these

scenes Scene #1 and Scene #3 will be presented as examples of multispectral cloud scene simulations.

**Table F-1:** Scenario list of simulated scene data used for the VCM.

<b>Scenarios</b>	<b>Description</b>	<b>Surface Type</b>
Scene #1	Ice cloud (9-10 km), Midlatitude, Nadir, Solar Z = 32	Vegetative
Scene #2	Ice cloud (9-10 km), Midlatitude, Nadir, Night	Vegetative
Scene #3	Water cloud (1-2 km), Midlatitude, Nadir, Solar Z = 32	Vegetative
Scene #4	Water cloud (1-2 km), Midlatitude, Nadir, Night	Vegetative
Scene #26	Ice cloud (9-10 km), Midlatitude, Nadir, Solar Z = 32	Ocean
Scene #27	Ice cloud (9-10 km), Midlatitude, Nadir, Night	Ocean
Scene #28	Water cloud (1-2 km), Midlatitude, Nadir, Solar Z = 32	Ocean
Scene #29	Water cloud (1-2 km), Midlatitude, Nadir, Night	Ocean

The first simulation will be a retrieval example will be the water cloud over vegetated land. The reflectances for the solar bands, and BTs for the thermal bands, are shown in Figure F-3. In this figure, the amount of multi-spectral information in the scene is displayed. Over different spectral bands, the underlying surface reflectance varies from that of the water clouds. In the BT images, the underlying surface is predominantly warmer than the water clouds in the scene.

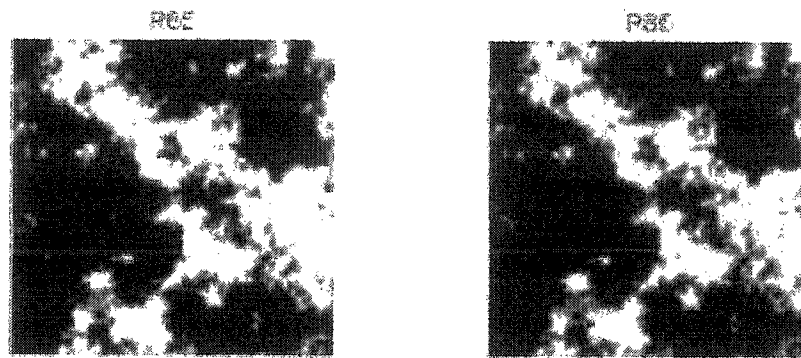


**Figure F-3 (a):** Reflectance for water cloud scene at 0.65 and 0.86  $\mu\text{m}$ .

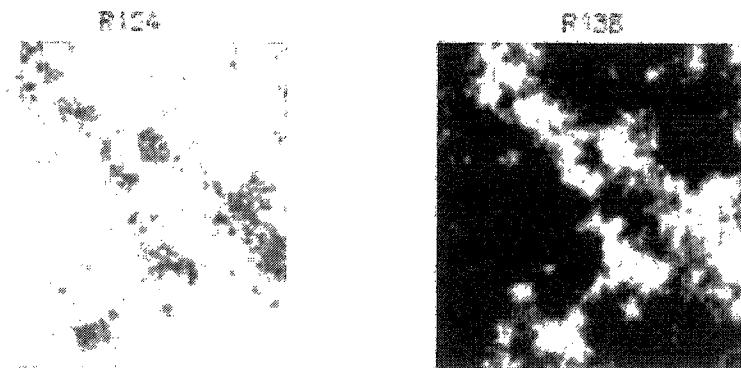


**Figure F-3 (b):** Reflectance for water cloud scene at 1.24 and 1.38  $\mu\text{m}$ .

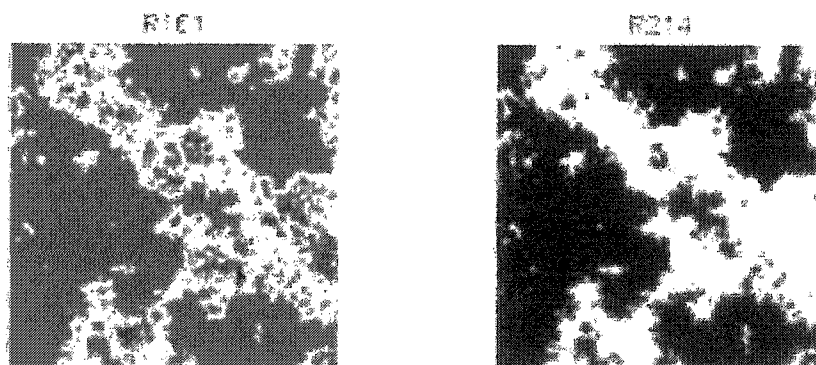


**Figure F-3 (c):** Reflectance for water cloud scene at 1.61 and 2.14  $\mu\text{m}$ .





**Figure F-3 (d):** BT for water cloud scene at 3.75 and 8.5  $\mu\text{m}$ .

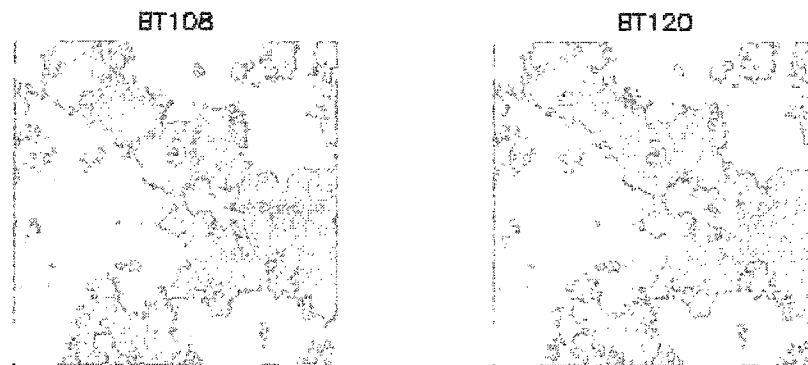


**Figure F-3 (e):** BT for water cloud scene at 10.8 and 12.0  $\mu\text{m}$ .

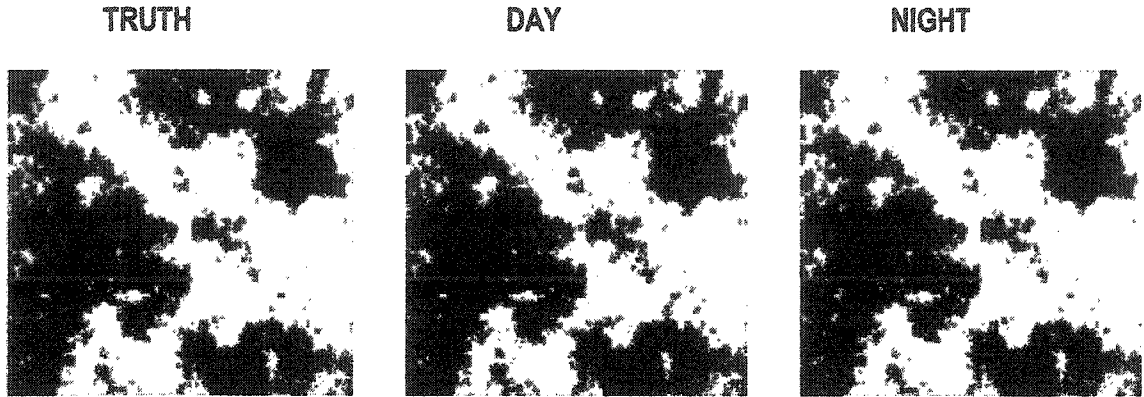


**Figure F-4:** VCM results for a simulated water cloud scene. VCM results for water cloud scene for ‘Tau-Truth’, day, and night cases.

Using tests discussed in Chapter 2, the VCM generates cloud mask results, which are displayed in Figure F-4. In this figure, the cloud mask is shown in gray, while black represents a negative cloud detection result. The three images in Figure F-4 display the cloud mask for three cases. The image on the left displays what is referred to as “Tau-Truth.” This represents cases where the optical thickness of the cloud displayed is greater than 0.03 at 0.65  $\mu\text{m}$ . This definition of a cloud comes directly from the definitions section of the VIIRS Sensor Requirements Document (SRD) (*NPOESS IPO*, 2000). The middle image is of the cloud mask results in the daytime. The far right image is the cloud mask results at night. The image shows that the cloud mask performance is very good for this scene. Note that this case (water clouds over land) is considered, due to the reflective and BT properties of land versus clouds. This case depicts a less difficult scene for the VCM, a more difficult scene is considered the below.

The next retrieval example is for a thin cirrus cloud over vegetated land. The reflectances for the solar bands and BTs for the thermal bands are shown in Figure F-5.

The cloud mask results are displayed in Figure F-6. This case is significantly more challenging than the water cloud case considered above.

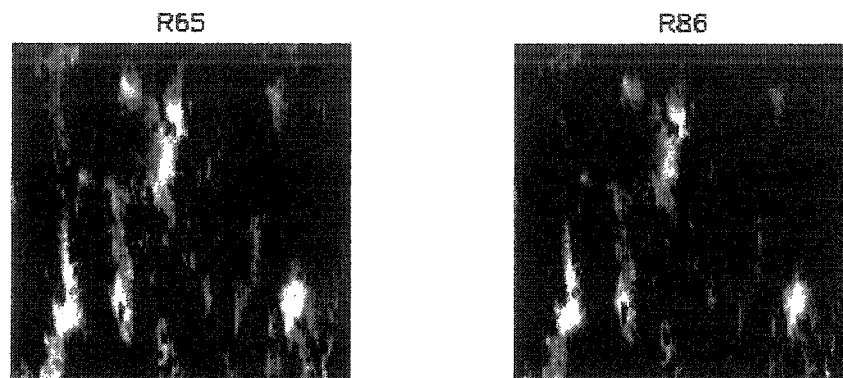


**Figure F-5 (a):** Reflectances for cirrus cloud scene at 0.65 and 0.86  $\mu\text{m}$ .

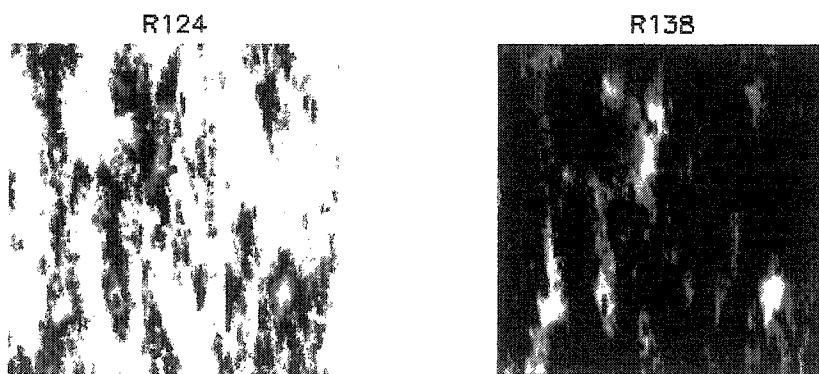


**Figure F-5 (b):** Reflectances for cirrus cloud scene at 1.24 and 1.38  $\mu\text{m}$ .

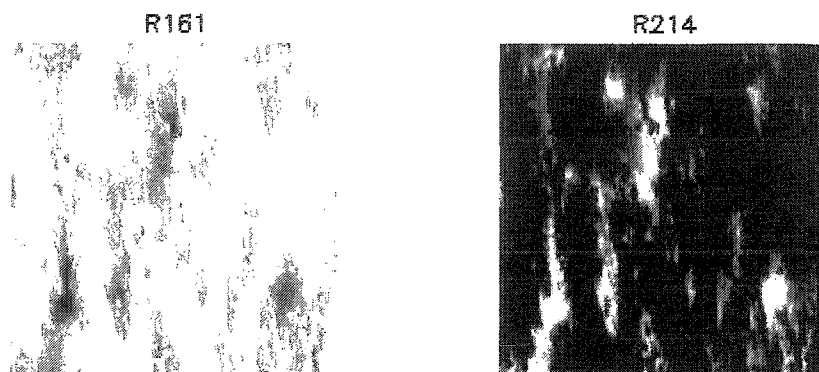


**Figure F-5 (c):** Reflectances for cirrus cloud scene at 1.61 and 2.14  $\mu\text{m}$ .



**Figure F-5 (d):** BT for cirrus cloud scene at 3.75 and 8.5  $\mu\text{m}$ .

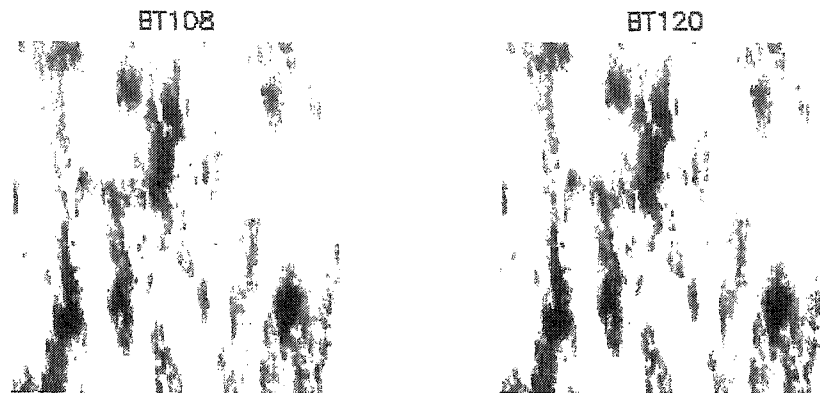


**Figure F-5 (e):** BT for cirrus cloud scene at 10.8 and 12.0  $\mu\text{m}$ .

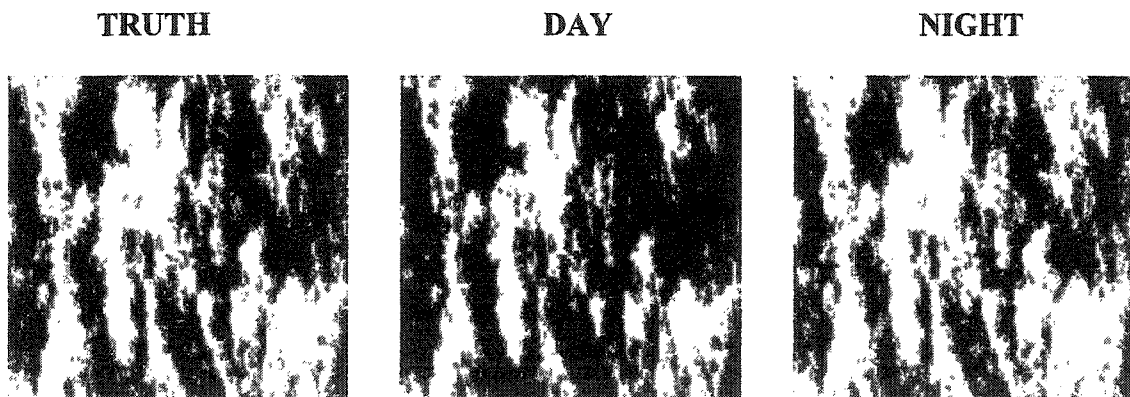


**Figure F-6:** VCM results for a simulated cirrus cloud. VCM cloud mask results for cirrus cloud 'Tau-Truth', day, and night cases.

**Appendix G**  
**GLOSSARY OF ACRONYMS**

**Table G-1: Table of acronyms.**

ADEOS2	Advanced Earth Observing Satellite-2
ARMCAS	Arctic Radiation Measurement in Column: Atmosphere-Surface
ATBD	Algorithm Theoretical Basis Document
AVHRR	Advanced Very High Resolution Radiometer
BBM	Band-to-Band Mis-registration
BRDF	Bidirectional Reflection Distribution Function
BT	Brightness Temperature
BW	Bandwidth
CAIV	Cost as an Independent Variable
CAR	Cloud Absorption Radiometer
CLAVR	Clouds from AVHRR
CLW	Cloud Liquid Water
CMIS	Conical Scanning Microwave Imager/Sounder
CRIS	Cross-track Infrared Sounder
CSSM	Cloud Scene Simulation Model
DEM	Digital Elevation Model
DMSP	Defense Meteorological Satellite Program
DNB	Daytime Nighttime Band
DOC	Department of Commerce
DoD	Department of Defense
DP	Data Product
DPA	Data Processing Architecture
EDC	EROS Data Center
EDR	Environmental Data Requirement

EDR	Environmental Data Record
EOS	Earth Observing System
EOS	Edge of Scan
ER-2	Experimental Research Plane
EROS	Earth Research Observation System
EUMETSAT	European Organization for the Exploitation of Meteorological Satellites
FOV	Field of View
FWHM	Full-width Half-maximum
GFM	Global Forecast Model
GIFOV	Ground Instantaneous Field of View
GLI	Global Imager
GOES	Geostationary Operational Environmental Satellite
GPSOS	Global Positioning System Occultation Sensor
GSD	Ground Sample Distance
HCS	Horizontal Cell Size
HSR	Horizontal Spatial Resolution
IA	Imagery Analyst
IABP	International Arctic Buoy Program
IFOV	Instantaneous Field of View
IP	Intermediate Product
IPO	Integrated Project Office
IR	Infra-Red
IWC	Ice Water Content
IWP	Ice Water Path
K	Kelvin
L	Spectral Radiance
LFA	Logical Flag Array
LIDAR	Light Detection and Ranging
LLS	Low-Level Light Sensor
LWIR	Long Wave Infra-Red

LUT	Look Up Table
MAS	MODIS Airborne Sensor
MCM	MODIS Cloud Mask
METOP	Meteorological Operational
MODIS	Moderate Resolution Imaging Spectroradiometer
MOPITT	Measurements of Pollution in the Troposphere
MTF	Modulation Transfer Function
MWIR	Mid-Wave-Infra-Red
NASA	National Aeronautics and Space Administration
NDII	Normalized Differential Ice Index
NDVI	Normalized Differential Vegetation Index
NIR	Near-InfraRed
NOAA	National Oceanic and Atmosphere Administration
NPOESS	National Polar-orbiting Operational Environmental Satellite System
OLS	Operational Linescan System
OMPS	Ozone Mapping Profiling Suite
PDR	Preliminary Design Review
POES	Polar Orbiting Environmental Satellite
PSC	Polar Stratospheric Clouds
R	Reflectance
RDQI	Radiometric Data Quality Indicator
RDR	Raw Data Record
RGB	Red-Green-Blue
RHS	Right Hand Side
RSS	Root Sum Squared
RT	Radiative Transfer
SBRS	Santa Barbara Remote Sensing
SDI	Snow Differential Index
SDR	Sensor Data Record
SDR	Supplemental Data Record



SEAWIFS	Sea-Viewing Wide Field-of-View Sensor
SESS	Space Environmental Sensor Suite
SNR	Signal-to-Noise Ratio
SRD	Sensor Requirements Document
SRR	Systems Requirements Review
SST	Sea Surface Temperature
SWIR	Short Wave Infra-Red
TBD	To Be Determined
TBR	To Be Resolved
TIROS-N	Television Infrared Observation Satellite
TOA	Top of Atmosphere
UCLA	University of California Los Angeles
US	United States
USGS	United States Geological Survey
UV	Ultraviolet
UW	University of Wisconsin
VCM	VIIRS Cloud Mask
VCP	VIIRS Cloud Phase
VIIRS	Visible/Infrared Imager/Radiometer Suite
VNIR	Visible-Near-Infrared
W	Watts
Z	Zenith

## References

- Ackerman, S. A., K. Strabala, P. Menzel, R. Frey, C. Moeller, L. Gumley, B. Baum, C. Schaaf, and G. Riggs, Discriminating Clear-Sky from Cloud with MODIS Algorithm Theoretical Basis Document (MOD35), *NASA Document*, Version 3.2, 1997.
- Ackerman, S. A., W. L. Smith and H. E. Revercomb, The 27-28 October 1986 FIRE IFO Cirrus Case Study: Spectral Properties of Cirrus Clouds in the 8-12 Micron Window, *Mon. Wea. Rev.*, 118, 2377-2388, 1990.
- Anderson, G. P., A. Berk, P. K. Acharya, M. W. Matthew, L. S. Bernstein, J. H. Chetwynd, H. Dothe, S. M. Adler-Golden, A. J. Ratkowski, G. W. Felde, J. A. Gardner, M. L. Hoke, S. C. Richtsmeier, B. Pukall, J. Mello and L. S. Jeong, MODTRAN4: Radiative Transfer Modeling for Remote Sensing, In Algorithms for Multispectral, Hyperspectral, and Ultraspectral Imagery VI, Sylvia S. Chen, Michael R. Descour, Editors, *Proceedings of SPIE*, Vol. 4049, pg. 176-183, 2000.
- Anderson, G. P., S. A. Clough, F. X. Kneizys, J. H. Chetwynd, and E. P. Shettle, AFGL Atmospheric Constituent Profiles (0-120 km), *Air Force Research Lab.*, AFRL-TR-86-0110 (OPI), Hanscom AFB, MA 01736, 1986.
- Apling, D., and M. Cianciolo, Cloud Cover Layers Visible/Infrared Imager Radiometer Suite Algorithm Theoretical Basis Document, *Raytheon Systems Company Document*, SBRS#Y2392, 3, 2000.

Barringer, A.R., *Unconventional Methods in Exploration for Petroleum and Natural Gas II*, Southern Methodist University Press, Dallas, pp. 219-239, 1981.

Berk, A., L. S. Bernstein, and D. C. Robertson, MODTRAN: A Moderate Resolution Model for LOWTRAN7, *Air Force Geophys. Lab.*, AFGL-TR-89-0122, 42 pp., Hanscom Air Force Base, Mass., 1989.

Borel, C. C., W. B. Clodius, and J. Johnson, Water Vapor Retrieval Over Many Surface Types, *SPIE Proc.*, 2758, 218-228, 1996.

Bouffies, S., F. M. Breon, D. Tanre, and P. Dubuisson, Atmospheric Water Vapor Estimate by a Differential Absorption Technique with the Polarization and Directionality of the Earth Reflectances (POLDER) Instrument, *J. Geophys. Res.*, 102, 3831-3841, 1997.

Brown De Colstoun, E. and W. Yang, Surface Type Visible/Infrared Imager/Radiometer Suite Algorithm Theoretical Basis Document, *Raytheon Systems Company Document*, SBRS #Y2402, 3, 2000.

Chesters, D. C., L. W. Uccellini, and W. D. Robinson, Low-level Water Vapor Fields from the VISSR Atmospheric Sounder (VAS) "Split-window Channels, *J. Clim. Appl. Meteorol.*, 22, 725-743, 1983.

Cicerone, R. and R. Oremland, Biogeochemical Aspects of Atmospheric Methane, *Global Biogeochem. Cycl.*, Vol. 2, pp. 299-327, 1988.

Clough, S. A., F. X. Kneizys, E. P. Shettle, and G. P. Anderson, Atmospheric Radiance and Transmittance: FASCODE2, *Proceedings of the Sixth Conference on Atmospheric Radiation*, pp. 141-144, Williamsburg, VA, 1986.

Conel, J. E., R. O. Green, C. Carrere, J. S. Margolis, R. E. Alley, G. Vane, C. J. Bruegge, and B. L. Gary, Atmospheric water vapor mapping with the airborne visible/infrared imaging spectrometer (AVIRIS) Mountain Pass, California, in *Proceedings of the Airborne Visible/Infrared Imaging Spectrometer (AVIRIS) Performance Evaluation Workshop*, edited by G. Vane, Publ. 88-38, pp. 21-29, Jet Propulsion Lab., Pasadena, Calif., 1988.

Cox, C., and W. Munk, Measurements of the Roughness of the Sea Surface from Photographs of the Sun's Glitter, *J. Opt. Soc. Am.*, 44, 838-850, 1954a.

Cox, C., and W. Munk, Statistics of the Sea Surface Derived from Sun Glitter, *J. Mar. Res.*, 13, 198-227, 1954b.

Cunningham, J., System Program Director, Requirements for the NPOESS Program, Climate and Global Change Panel, Winter Meeting, January 25, 2001.

Dickinson, R. E., and R. J. Cicerone, Future Global Warming from Atmospheric Trace Gases, *Nature*, 319:109-115, 1986.

Durham, R., Performance Specification Algorithm Specification for VIIRS, *Raytheon Systems Company Document*, PRFSS154650-001, 2000.

Everett, J. R., R. J. Staskowski, and C. Jengo, Remote Sensing and GIS Enable Future Exploration Success, *World Oil*, 223:11, pp. 59-60, 63-5, 2002.

Ferraro, R. R., F. Z. Weng, N. C. Grody, and A. Basist, An Eight Year (1987-1994) Time Series of Rainfall, Clouds, Water Vapor, Snow Cover, and Sea Ice Derived from SSM/I Measurements, *Bull. Am. Meteorol. Soc.*, 77, 891-905, 1996.

Fraser, R. S., and Y. J. Kaufman, The Relative Importance of Aerosol Scattering and Absorption in Remote Sensing, *IEEE J. Geosci. Remotes. Sens.*, 23, 525-633, 1985.

Frouin, R., P. Y. Deschamps, and P. Lecomte, Determination from Space of Atmospheric Total Water Vapor Amounts by Differential Absorption Near 940 nm: Theory and Airborne Verification, *J Appl. Meteorol.*, 29, 448-460, 1990.

Gao, B-C., and A. F. H. Goetz, Column Atmospheric Water Vapor and Vegetation Liquid Water Retrievals from Airborne Imaging Spectrometer Data, *J. Geophys. Res.*, 95, 3549-3564, 1990.

Gao, B. C., A. F. H. Goetz, and W. J. Wiscombe, Cirrus Cloud Detection From Airborne Spectrometer Data Using the 1.38 Micron Water Vapor Band, *Geophys. Res. Lett.*, 20, 301-304, 1993.

Gao, B-C., and Y. Kaufman, MODIS Near-IR Water Vapor Algorithm: Algorithm Theoretical Basis Document (MOD05), Product ID – MOD05 Total Precipitable Water, *NASA Document*, NASA Goddard Space Flight Center, 1998.

Gao, B.-C., and Y. Kaufman, Water Vapor Retrievals Using Moderate Resolution Imaging Spectroradiometer (MODIS) Near-infrared Channels, *J. Geophys. Res.*, 108, 4389, doi:10.1029/2002JD0003023, 2003.

Gao, B.-C., Han, W., Tsay, S.-C., and Larsen, N. F., Cloud Detection Over the Arctic Region Using Airborne Imaging Spectrometer Data During the Daytime, *J Appl. Meteorol.*, 37(11), 1421-1429, 1998.

Gatebe C. K., M. King, A. Lyapustin, G. T. Arnold, and J. Redemann, Airborne Spectral Measurements of Ocean Directional Reflectance, *Journal of Atmospheric Sciences*, in Press 2005.

Gatebe C. K., M. King, S. Platnick, G. T. Arnold, M. Gray, E. Moody, P. Hubanks, and J. Riedi, Cloud Absorption Radiometer Measurements for Chesapeake Lighthouse and Aircraft Measurements for Satellite CLAMS Experiment, GESTC/UMBC Presentation, February, 2002.

Goodman, A. H., and A. Henderson-Sellers, Cloud Detection Analysis: A Review of Recent Progress, *Atm. Res.*, 21, 203, 1988.

Gournay, L.S., J. W. Harrell, and C. L. Dennis, Remote Sensing of Hydrocarbon Gas Seeps Utilizing Microwave Energy, U.S. Patent No. 4, 132, 943, 1979.

Grant, W. B., and R. T. Menzies, A Survey of Laser and Selected Optical Systems for Remote Measurement of Pollutant Gas Concentrations, *J. Air Pollut. Control Assoc.*, 33, 187-194, 1983.

Gustafson, G. B., R. G. Isaacs, R. P. d'Entremont, J. M. Sparrow, T. M. Hamill, C. Grasotti, D. W. Johnson, C. P. Sarkisian, D. C. Peduzzi, B. T. Pearson, V. D. Jakabhazy, J. S. Belfiore, and A. S. Lisa, Support of Environmental Requirements for Cloud Analysis and Archive (SERCAA): Algorithm Descriptions, *Phillips Laboratory Document*, PL-TR-94-2114, AFMC, Hanscom AFB, MA, 1994.

Hagolle, H., J.-M., Nicolas, B. Fougnie, F. Cabot, and P. Henry, Absolute Calibration of VEGETATION Derived From an Interband Method Based on the Sun Glint Over Ocean, *IEEE Trans. On GeoScience and Remote Sensing*, Vol. 42, No. 7, July, 2004.

Halbouty, M. T., Application of LANDSAT Imagery to Petroleum and Mineral Exploration, *AAPG Bull.*, 60:5, pp. 745-793, 1976.

Hall, D. K., G. A. Riggs, and V. V. Solomonson, Development of Methods for Mapping Global Snow Cover Using Moderate Resolution Imaging Spectroradiometer Data, *Remote Sens. Env.*, 54, 127-140, 1995.

Hall, D. K., G. A. Riggs, and V. V. Solomonson, Algorithm Theoretical Basis Document (ATBD) for the MODIS Snow-, Lake Ice-, and Sea Ice-Mapping Algorithms, *NASA Document*, Version 3.0, 1996.

Hansen, M., DeFries, R., Townshend, J., and Sohlberg, R., Global Land Cover Classification at 1 km Spatial Resolution Using a Classification Tree Approach, *Int. J. Remote Sensing*, 21, 6 & 7, 1331-1364, 2000.

Hansen, J. E., and L. D. Travis, Light Scattering in Planetary Atmospheres, *Space Sci. Rev.*, 16, 527-610, 1974.

Hornafius, S. J., J. D. Quigley, B. Luyendyk, The Worlds Most Spectacular Marine Hydrocarbon Seeps (Coal Oil Point, Santa Barbara Channel, California): Quantification of Emissions, *J. Geophys. Res.*, 104(C9): 20,730-20,711, 1999.

Hoyt, D., VIIRS Radiometric Calibration Component Level Software Architecture, *Raytheon Systems Company Document*, 3.0, 1999.

Hoyt, D. V., H. L. Kyle, J. R. Hickey, and R. H. Maschhoff, The Nimbus-7 Solar Total Irradiance: A New Algorithm for its Determination, *J. Geophys. Res.*, 97A, 51-63, 1992.



Hunt, J. H., Surface Geochemical Prospecting Pro or Con, AAPG Annual Convention, San Francisco, May, 1981.

Hutchison, K. D., and K. Hardy, Threshold Functions for Automated Cloud Analyses of Global Meteorological Satellite Imagery, *Int. J. Remote Sens.*, 16, 3665-3680, 1995.

Hutchison, K. D., and N. Choe, Application of 1.38  $\mu\text{m}$  Imagery for Thin Cirrus Detection in Daytime Imagery Collected Over Land Surfaces, *Int. J. Remote Sens.*, 17, 3325-3342, 1996.

Hutchison, K. D., and J. K. Locke, Snow Identification through Cirrus Cloudy Atmospheres using AVHRR Daytime Imagery, *Geophys. Res. Lett.*, 24, 1791-1794, 1997.

Hutchison, K. D., K. Hardy, and B. C. Gao, Improved Detection of Optically-thin Cirrus Clouds in Nighttime Multispectral Meteorological Satellite Imagery Using Total Integrated Water Vapor Information, *Journal of Applied Meteorology*, 34, 1161-1168, 1995.

Hutchison, K. D., B. J. Etherton, and P. C. Topping, Validation of Automated Cloud Top Phase Algorithms: Distinguishing Between Cirrus Clouds and Snow in A-priori Analyses of AVHRR Imagery, *Optical Engineering*, 36, 1727-1737, 1997.

Kaufman, Y. J., and B-C. Gao, Remote Sensing of Water Vapor in the Near IR from EOS/MODIS, *IEEE Trans. Geosci. Remote Sens.*, 30, 871-884, 1992.

Kaufman, Y. J., J. V. Martins, L. A. Remer, M. R. Schoeberl, and M. A. Yamasoe, Retrieval of Black Carbon Absorption from Proposed Satellite Measurements Over the Ocean Glint, *Geophys. Res. Lett.*, 29, doi:10.1029/2002GL015403, 2002.

Kaufman, Y. J., A. Wald, L. A. Remer, B. C. Gao, R. R. Li, and L. Flynn, The MODIS 2.1  $\mu\text{m}$  Channel- Correlation with Visible Reflectance for use of Remote Sensing of Aerosol, *IEEE Trans. Geosci. Remote Sens.*, 35, 1286-1298, 1997.

Kealy, P., VIIRS Instrument Level Flowdown Results Signal to Noise Requirements, *Raytheon Systems Company Document*, 3, 2000.

Kealy, P. and P. Ardanuy, VIIRS Algorithm Data Definition Document – Instrument Parameter MTF, *Raytheon Systems Company Document*, Y2372, 3, 1999.

Kealy, P. and P. Ardanuy, VIIRS Instrument Level Flowdown Results 45 Degree Mirror Band-to-Band Registration Requirements, *Raytheon Systems Company Document*, SBRS#Y3250, 3, 2000a.

Kealy P. and P. Ardanuy, Systems Verification Report Error Budget Visible/Infrared Imager/Radiometer Suite, *Raytheon Systems Company Document*, SBR#Y3249, 3, 2000b.

Kealy P. and P. Ardanuy, VIIRS Systems Verification and Validation, *Raytheon Systems Company Document*, TP154640-001, 3, 2000c.

Kealy, P. and P. Ardanuy, VIIRS Sensor Specifications Document, *Raytheon Systems Company Document*, PS154640-101, 3, 2000d.

King, M. D. and D. Herring, The MODIS Airborne Simulator (MAS), *Earth Observer Magazine*, Nov./Dec. 1992.

King, M. D., W. P. Menzel, P. S. Grant, J. S. Myers, G. T. Arnold, S. E. Platnick, L. E. Gumley, S. C. Tsay, C. C. Moeller, M. Fitzgerald, K. S. Brown, and F. G. Osterwisch, Airborne Scanning Spectrometer for Remote Sensing of Cloud, Aerosol, Water Vapor, and Surface Properties, *J. Atmos. Oceanic Technol.*, 13, 777-794, 1996.

King, M. D., M. G. Strange, P. Leone, and L. R. Blaine, Multiwavelength Scanning Radiometer for Airborne Measurements of Scattered Radiation within Clouds, *J. Atmos. Oceanic Technol.*, 3, 513-522, 1986.

King, M. D., S. Tsay, S. Ackerman, N. Larsen, Discriminating Heavy Aerosol, Clouds, and Fires During SCAR-B: Application of Airborne Multispectral MAS Data, *J. Geophys. Res.*, 103, D24, 31,989 - 31,999, 1998.

Kleidman, R. G., Y. J. Kaufman, B. C. Gao, L. A. Remer, V. G. Brackett, R. A. Ferrare, E. V. Browell, and S. Ismail, Remote Sensing of Total Precipitable Water Vapor in the Near-IR Over Ocean Glint, *Geophys. Res. Lett.*, 27, 2657-2660, 2000.

Klusman, R. W., Soil and Gas Related Methods for Natural Resource Exploration, John Wiley & Sons, England, 473 pp., 1993.

Kneizys, F. X., E. P. Shettle, L. W. Abreu, J. H. Chetwynd, G. P. Anderson, W. O. Gallery, J. E. A. Selby, and S. A. Clough, Users Guide to LOWTRAN 7, *Air Force Geophys. Lab Report*, AFGL-TR-88-0177, Hanscom, AFB, MA 01731, 1988.

Koepke, P., Effective Reflectance of Oceanic White Caps, *Appl. Opt.*, Vol. 20, pp. 1816-1824, 1984.

Kriebel, K. T., and R. W. Saunders, An Improved Method for Detecting Clear Sky and Cloudy Radiances from AVHRR Data, *Int. J. Remote Sens.*, 9, 123-150, 1988.

Kuin, N., VIIRS Build SDR Module Level Software Architecture Visible/Infrared Imager/Radiometer Suite, *Raytheon Systems Company Document*, SBRS#Y2479, 3, 2000.

Jensen, K., D. Apling, I. Appel, K. Hutchison, R. Julian, N. Larsen, W. Yang, Imagery Visible/Infrared Imager/Radiometer Suite Algorithm Theoretical Basis Document, *Raytheon Systems Company Document*, SBRS #Y2466, 3, May, 2000.

Larsen, N., Improved Multiple Scattering Computations in a Moderate Resolution Radiative Transfer Model, University of Alaska Fairbanks, M.S. Thesis, 1994.

Larsen, N., Cloud Mask Visible/Infrared Imager/Radiometer Suite Algorithm Theoretical Basis Document, *Raytheon Systems Company Document*, SBRS #Y2412, 3, 2000a.

Larsen, N., Band-to-Band Registration Effect on the VIIRS Cloud Mask SDR and the Cloud Cover EDR, *Raytheon Systems Company Document*, 3, 2000b.

Larsen, N., VIIRS Cloud Mask Component Level Software Architecture Visible/Infrared Imager/Radiometer Suite Component Software Architecture, *Raytheon Systems Company Document*, SBRS#Y3244, 3, 2000c.

Larsen, N., D. Apling, and M. Cianciolo, Signal to Noise Requirements on the VIIRS Cloud Mask SDR and the Cloud Cover EDR, *Raytheon Systems Company Document*, 3, 2000a.

- Larsen, N. F. and K. Stamnes, Use of Shadows to Retrieve Water Vapor in Hazy Atmospheres, *Appl. Opt.*, Submitted, 2005a.
- Larsen, N. F. and K. Stamnes, Methane Detection from Space: Use of Sun Glint, *Opt. Eng.*, Submitted, 2005b.
- Link, W. K., Significance of Oil and Gas Seeps in World Oil Exploration, *Amer. Assoc. Pet. Geol. Bull.*, 36: 1505-1541, 1952.
- Loveland, T. R., J. M. Merchant, D. O. Ohlen, and J. F. Brown, Development of a Landcover Characteristic Database for the Conterminous U.S., *Photogrammetric Engineering and Remote Sensing*, 57 (11), 1453-1463, 1991.
- McClatchey, R. A., R. W. Fenn, J. E. A. Selby, F. E. Volz and J. S. Garing, Optical Properties of the Atmosphere, *AFCRL Report*, AFCRL-72-0497, Air Force Cambridge Res. Lab., Bedford, MA, 1972.
- McLaren, S., R. Richards, and J. Armstrong, Ground Survey of the Raton Basin for Methane Seeps, Apogee Scientific Inc., Contract C166016, June, 2001.
- Menzel P. and K. Strabala, Cloud Top Properties and Cloud Phase Algorithm Theoretical Basis Document, *NASA Document*, 5.0, 1997.

NPOESS IPO, Ozone Mapping Profiling Suite (OMPS) Sensor Requirements Document (SRD), National Polar-Orbiting Operational Environmental Satellite System (NPOESS) Spacecraft and Sensors, NPOESS Document, 2, February, 1999a.

NPOESS IPO, Cross Track Infrared Sounder (CRIS) Sensor Requirements Document (SRD), National Polar-Orbiting Operational Environmental Satellite System (NPOESS) Spacecraft and Sensors, NPOESS Document, 2, March, 1999b.

NPOESS IPO, Visible/Infrared Imager/Radiometer Suite (VIIRS) Sensor Requirements Document (SRD), National Polar-Orbiting Operational Environmental Satellite System (NPOESS) Spacecraft and Sensors, NPOESS Document, 3, June, 2000.

NPOESS IPO, Conical Scanning Microwave Image/Sounder (CMIS) Sensor Requirements Document (SRD), National Polar-Orbiting Operational Environmental Satellite System (NPOESS) Spacecraft and Sensors, NPOESS Document, 3, March, 2001.

Olson, J. S., J. A. Watts, and L. J. Allison, Global Ecosystems Database, Ecosystem and Global Change Program, National Geophysical Data Center, Boulder, Colorado 80303, USA, 1994.

Ophir Corp., Crude Oil Pipeline Leak Detection System Demonstrated: New System for Remote Liquid Pipeline Leaks Validated, Press Release, 2003.

Ou, S., K. Liou, Y. Takano, G. Higgins, N. Larsen, Cloud Effective Particle Size and Cloud Optical Thickness Visible/Infrared Imager Radiometer Suite Algorithm Theoretical Basis Document, *Raytheon Systems Company Document*, SBR#Y2407, 3, 2000.

Peixoto, J. P., and A. H. Oort, *Physics of Climate*, American Institute of Physics, New York, pp. 278-285, 1992.

Prabhakara, C., H. D. Chang, and A. T. C. Chang, Remote Sensing of Precipitable Water Over the Oceans from Nimbus 7 Microwave Measurements, *J. Appl. Meteorol.*, 21, 59-68, 1982.

Ramanathan, V., R. J. Cicerone, H. B. Singh and J. T. Kiehl. Trace Gas Trends and their Potential Role in Climate Change, *J. Geophys. Res.*, 90: 5547-5566, 1985.

Rasmussen, R. A., and M. A. K. Kahlil, Atmospheric Methane in Recent and Ancient Atmospheres: Concentrations, Trends, and Interhemispherical Gradient, *J. Geophys. Res.*, 89:11599-11605, 1984.

Rossow, W. B., Measuring Cloud Properties from Space: A Review, *J. Clim.*, 2, 201, 1989.

Rothman, L. S., C. P. Rinsland, A. Goldman, S. T. Massie, D. P. Edwards, J. -M. Flaud, A. Perrin, C. Camy-Payret, V. Dana, J. -Y. Mandin, J. Schroeder, A. McCaan, R. R. Gamache, R. B. Wattson, K. Yoshino, K. V. Chance, K. W. Jucks, L. R.



Brown, V. Nemtchinov, P. Varanasi, The HITRAN Molecular Spectroscopic Database and HAWKS (HITRAN Atmospheric Work Station): 1996, *J. Quant. Spectrosc. Radiat. Transfer*, Vol. 60, No. 5, pp 665-710, 1998.

Safley, L. M., M. E. Casada, J. W. Woodbury, and K. F. Roos. Global Emissions from Livestock and Poultry Manure, Report No. EPA 1400/1-91/048, U.S. Environmental Protection Agency, Washington D.C., 145 p., 1992.

Salomonson, V. V., W. L. Barnes, P. W. Maymon, H. E. Montgomery and X. Ostrow, MODIS: Advanced Facility Instrument for Studies of the Earth as a System, *IEEE Transactions in Geosciences and Remote Sensing*, 27, 5954--5964, 1989.

Saunders, R. W. and K. T. Kriebel, An Improved Method for Detecting Clear Sky and Cloudy Radiances from AVHRR data, *Int. J. Remote Sens.*, 9, 123-150, 1988.

Schumacher, D., and M. A. Abrams, Hydrocarbon Migration and its Near Surface Expression, *AAPG Memoir*, 66, 446 pp., 1996.

Shettle, E. P. and R. W. Fenn, Models of Atmospheric Aerosols and their Optical Properties, Optical Propagation in the Atmosphere, Agard Conference Proceedings 183, AGARD-CP-183, [NTIS ADA 028615], 1976.

SRI Int., Remote Gas Leak Detector for Underground Pipelines, SRI Int. Report, 2004.

Stamnes, K., S-C. Tsay, W. Wiscombe, and K. Jayaweera, Numerically Stable Algorithm for Discrete-Ordinate-Method Radiative Transfer in Multiple Scattering and Emitting Layered Media, *Appl. Opt.*, 27, 2502-2509, 1988.

Stamnes, K., Cloud Detection Over Snow/Ice (CTSK1) Algorithm Description, *NASDA internal document*, 3.4.1- -3.4.1-28, 1999.

Stamnes, K., Snow Grain Size Retrieval in Polar and Mid-latitude Regions, ATBD (CTSK2b1), *NASDA internal document*, 3.4.2-1-3.4.1-27, March, 2003.

Stowe, L. L., P. Davis, and E. P. McClain, Evaluating CLAVR (Clouds from AVHRR) Phase I Cloud Cover Experimental Product, *Adv. in Space Res.*, 16, 21-24, 1995.

Stowe, L. L., P. Davis, and E. P. McClain, Scientific Basis and Initial Evaluation of the CLAVR-I Global Clear/Cloud Classification Algorithm for the Advanced Very High Resolution Radiometer, *J. Atmos. and Oceanic Technology*, May, 1998.

Strabala, K. I., S. A. Ackerman, and W. P. Menzel, Cloud Properties Inferred from 12 Micron Data, *J. Appl. Meteor.*, 33, 212-229, 1994.

Strahler, A., J. Townshend, J. Borak, A. Hyman, E. Lambin, A. Moody, and D. Muchoney, MODIS Land Cover Algorithm Theoretical Basis Document, *NASA Document*, December, 1996.

Su, W., T. P. Charlock, and K. Rutledge, Observations of Reflectance Distribution Around Sun Glint from a Coastal Ocean Platform, *Appl. Opt.*, 41, 35, Dec., 2002.

Susskind, J., J. Rosenfield, and D. Reuter, Remote Sensing of Weather and Climate Parameters from HIRS2/MSU on TIROS-N, *J. Geophys. Res.*, 89, 4677-4697, 1984.

Tedesco, S. A., Surface Geochemistry in Petroleum Exploration, Chapman and Hall, pp. 1-29, 1995.

Thai, S. and M. V. Schonermark, Determination of the Column Water Vapor of the Atmosphere Using Backscattered Solar Radiation Measured by the Modular Optoelectronic Scanner (MOS), *Int. J. Remote Sens.*, 19, 3223-3236, 1998.

Thomas, G. E. and K. Stamnes, Radiative Transfer in the Atmosphere and Ocean, Cambridge University Press, 1999.

Thompson, C. K., Unconventional Methods in Exploration for Petroleum and Natural Gas II, Southern Methodist University Press, Dallas, pp. 240-248, 1981.

- Thuillier, G., M. Herse, P. Simon, D. Labs, H. Mandel, and Gillotay, Observation of the Solar Spectral Irradiance from 200 to 850 nm During the ATLAS Missions by the SOLSPEC Spectrometer, NEWRAD 97 Presentation, 1997.
- Tsay, S.-C., and G. L. Stephens, A Physical/Optical Model for Atmospheric Aerosols with Application to Visibility Problems, CIRA Report, (ISSN 0737-5352-16), January, 1990.
- Valvocin, F. R., Spectral Radiance of Snow and Clouds in the Near Infrared Spectral Region, *Tech Report No. 78-0289, Air Force Research Lab, Hanscom Air Force Base, MA, 1978.*
- Vesperini, M., F-M., Breon, and D. Tanre, Atmospheric Water Vapor Content from Spaceborne POLDER Measurements, *IEEE Trans. Geosci. Remote Sens.*, 37, 1613-1619, 1999.
- Yan, B., K. Stamnes, W. Li, B. Chen, J. J. Stamnes, and S. C. Tsay, Pitfalls in Atmospheric Correction of Ocean Color Imagery: How Should Aerosol Optical Properties be Computed?, *Appl. Opt.*, 41, 412-423, 2002.
- Yang, H., J. Zhang, F. van der Meer, and S. B. Kroonenberg, Geochemistry and Field Spectrometry for Detecting Hydrocarbon Microseepage, *Terra Nova*, 10, pp. 231-235, 1998.